Electronic Transport Properties of Stabilized Amorphous Selenium X-ray Photoconductors

A Thesis

Submitted to the College of Graduate Studies and Research

in Partial Fulfillment of the Requirements for the Degree of

Master of Science

in the Department of Electrical Engineering

University of Saskatchewan

By

Bud J Fogal

Saskatoon, Saskatchewan

PERMISSION TO USE

In presenting this thesis in partial fulfillment of the requirements for a Postgraduate degree from the University of Saskatchewan, I agree that the Libraries of this University may make it freely available for inspection. I further agree that permission for copying of this thesis in any manner, in whole or in part, for scholarly purposes may be granted by the professor or professors who supervised my thesis work or, in their absence, by the Head of the Department or the Dean of the College in which my thesis work was done. It is understood that any copying or publication or use of this thesis or parts thereof for financial gain shall not be allowed without my written permission. It is also understood that due recognition shall be given to me and to the University of Saskatchewan in any scholarly use which may be made of any material in my thesis.

Requests for permission to copy or to make other use of material in this thesis in whole or part should be addressed to:

Head of the Department of Electrical Engineering
University of Saskatchewan
Saskatoon, Canada, S7N 5A9

ACKNOWLEDGEMENTS

I extend my sincerest gratitude towards my supervisor, Dr. S.O. Kasap, and my co-supervisor, Dr. S.K. O'Leary, for their patience, encouragement and leadership throughout the course of this project. I also thank Dr. Robert Johanson for his assistance with the initial design and setup of the experimental system, Zahangir Kabir for his derivation of Ramo's Theorem and George Belev for his excellent answers to my many questions. This thesis would not have been possible without the financial support from the University of Saskatchewan, NSERC, Anrad and Micronet. Finally, I would like to thank my family and girlfriend, Michelle Cruz, for their support, encouragement and patience.

ABSTRACT

Amorphous selenium (a-Se) and its alloys are important photoconductor materials used in direct conversion flat panel digital x-ray detectors. The performance of these detectors is determined, in part, by the electronic transport properties of the a-Se photoconductor layer – namely, the charge carrier mobility μ and the deep trapping lifetime τ. The product of the mobility and the lifetime $\mu\tau$, referred to as the charge carrier range, determines the average distance that photo-generated charge will travel before being removed from the transport band by deep localized states in the mobility gap of the semiconductor. The loss of carriers to these deep states reduces the amount of charge collected per unit of x-ray exposure, and, hence, limits the x-ray sensitivity of the detector. Two experimental techniques that may be used to measure the transport properties of holes and electrons in high resistivity semiconductors are described in this thesis. The Time-of-Flight (TOF) transient photoconductivity technique is used to evaluate the charge carrier mobility by measuring the time required for the charge carriers to transit a fixed distance under the influence of an applied electric field. The Interrupted-Field Time-of-Flight (IFTOF) technique is used to determine the charge carrier deep trapping time; the drift of the injected carriers is temporarily interrupted at a position in the sample by removing the applied field. When the field is reapplied the number of charge carriers has decreased due to trapping events. The carrier lifetime is determined from the dependence of the fraction of recovered charge carriers before and after the interruption with the interruption time.

TOF and IFTOF measurements were carried out on a number of samples of vacuum deposited selenium alloy x-ray photoconductors. Device quality photoconductor films are fabricated by evaporating a-Se source material that has been alloyed with a small quantitiy of As (~0.3 at. %) and doped with a halogen (typically Cl) in the p.p.m. range. The dependence of the carrier range on the composition of the photoreceptor film was accurately measured using both TOF and IFTOF measurements. It was found that the transport properties of the film could be controlled by suitably adjusting the composition of the alloy. Combined IFTOF and TOF measurements were also performed on several samples to examine the effects of trapped electrons on the hole transport properties in a-Se films. It was found that drifting holes recombine with the trapped electrons, and that this process could be described by a Langevin recombination process. This finding is important for the correct modeling of amorphous selenium digital x-ray detector designs. Finally, the effects of x-ray exposure on a-Se films were examined. A temporary reduction in the effective hole lifetime was observed due to an increase in the number of hole capture centers following an x-ray exposure. The capture coefficient between free holes and the x-ray induced hole capture centers was measured using combined TOF and IFTOF measurements. It was shown that this capture process was governed by the Langevin recombination mechanism. From these observations it was concluded that trapped electrons from a previous x-ray exposure act as recombination centers for subsequently generated holes, thereby reducing the effective hole lifetime in the sample.

TABLE OF CONTENTS

LIST OF FIGURES

LIST OF TABLES

LIST OF ABBREVIATIONS

a-Se	amorphous selenium
a-Si:H	hydrogenated amorphous silicon
AB	anti-bonding
AMA	active matrix array
BJT	bipolar junction transistor
CCD	charge coupled device
CFO	density of states model proposed by Cohen, Fritsche and Ovshinski
CMOS	complementary metal oxide semiconductor
CMRR	common mode rejection ratio
EHP	electron hole pair
ESR	electron spin resonance
FET	field effect transistor
GPIB	general purpose instrumentation bus
HV	high voltage
IFTOF	interrupted field time-of-flight
ITO	indium tin oxide
IVAP	intimate valence alternation pair
LCD	liquid crystal display
LP	lone pair
NB	non-bonding
NSB	normal structure bonding
PC	personal computer
PCB	printed circuit board
PCI	peripheral component interconnect

PPM	parts per million
RFI	radio frequency interference
SNR	signal to noise ratio
SPDT	single pole double throw
SPST	single pole single throw
TFT	thin film transistor
TOF	time-of-flight
TP	transient photoconductivity

1. DIGITAL RADIOGRAPHY AND STABILIZED AMORPHOUS SELENIUM

1.1 Introduction

Radiography, the creation of images by measuring the differential attenuation of ionizing radiation, such as x-rays, which pass through a body, is well established as an important diagnostic tool in hospitals and medical clinics. Currently, radiography relies on a film emulsion to store the optical response that is generated when incident x-ray photons interact with a phosphorescent screen. The film and screen are coupled together and packaged as an x-ray detector cassette, which is manually inserted into the radiographic system prior to exposing the patient to x-ray radiation. Following the exposure, the cassette must be removed from the system and transported to a separate room for processing before the image can be examined. If the quality of the image is unacceptable, the exposure settings on the system are adjusted, and the entire process is repeated until a suitable image is generated. The resulting image prints are large, difficult to handle and store, and must be manually examined on a lighted view box to diagnose the patient's condition.

Digital imaging technology has the potential to make the process of capturing x-ray images considerably more efficient [1]. Ideally, a digital radiographic system would monitor the quality of the image, automatically adjust the exposure settings as necessary, and display a digital image immediately following the x-ray exposure on a video monitor. Such "real-time" detectors are ideally suited for fluoroscopic procedures where a motion picture is generated to aid internal guiding therapies such as angioplasty. Furthermore, analytical software can be used to enhance the quality of the digital image or to facilitate the computer-aided-diagnoses of complex medical conditions [2]. The digital image files can easily be stored on centralized file servers and shared over computer networks for the provision of clinical care to individuals in remote locations [3].

One of the most important developments in digital radiographic imaging is the concept of a direct conversion flat panel x-ray image detector [4]. In this system, a layer of an x-ray photoconductive material is coated onto a large area integrated circuit called an Active-Matrix-Array (AMA). The x-ray photoconductor converts incident x-ray photons into electronic charge, which is then stored in charge collection capacitors located in each element of the AMA circuit. Thin-Film-Transistors located in each array element coordinate the readout of the image charge, and the resulting signal is digitized and sent to a computer for processing and display. The photoconductor, AMA, and readout electronics can be packaged as a compact detector unit capable of fitting into existing film/screen based radiographic imaging systems. Most importantly, flat panel direct conversion x-ray image detectors have the potential to produce higher quality images at lower x-ray doses than is currently possible with film/screen based systems [5].

Alloys of a-Se are an attractive direct conversion photoconductor mainly because large-area, uniform layers may be economically fabricated using conventional vacuum deposition techniques without damaging the AMA electronics [6]. The photoconductor properties of the a-Se layer determine, in large measure, the x-ray sensitivity of the detector. These include the x-ray absorption efficiency, the electron hole pair creation energy, and the charge carrier drift mobility and deep trapping time (lifetime). Furthermore, a-Se layers exhibit a low dark current compared to other potential x-ray photoconductors [6]. Continued research into properties of a-Se and its alloys is important in order to understand the processes that will lead to increased x-ray detector performance.

One of the objectives of this work was to develop and utilize a system capable of performing Time-of-Flight (TOF) and Interrupted-Field Time-of-Flight (IFTOF) transient photoconductivity experiments on stabilized a-Se photoconductive layers. Transient photoconductivity experiments capture the transient response that results when a short pulse of highly absorbed light injects carriers into an electroded and biased photoconductor. In the TOF experiment, the pulse width of the transient response that is generated when the injected carriers drift across the entire length of the sample is measured in order to determine the charge carrier mobility μ. In the IFTOF experiment, the fractional change in the magnitude of the transient response that occurs when the external field is temporarily removed is measured in order to determine the charge carrier deep trapping time (lifetime) τ. Both of these techniques are important for characterizing the performance of a-Se x-ray photodetectors inasmuch as the product of the mobility and the lifetime $\mu\tau$ determines their x-ray sensitivity [6].

The TOF technique is well established as a technique for measuring the drift mobility in a-Se, and it is extensively discussed in the literature. The IFTOF, however, has not been widely implemented for measuring the lifetime in a-Se layers because of the large fields that are required to bias these layers for transient photoconductivity measurements. The temporary removal of the bias from the capacitive sample produces voltage transients that are considerably larger than the desired photocurrent signal. These voltage transients may, however, be eliminated by performing a differential measurement across a bridge network containing an equivalent capacitive load. High-speed rectifiers limit the magnitude of the switching transients to within the safe operating range of the electronics used to detect and amplify the desired photocurrent signal.

The TOF and IFTOF techniques were applied to various samples of stabilized a-Se in order to:

1. measure the inherent charge transport properties μ and τ,
2. determine the effects of alloy composition on the carrier $\mu\tau$ product,
3. determine if trapped electrons can act as recombination centers for drifting holes, and
4. investigate the effects of x-ray exposure on the transport properties.

1.2 Principles of Digital Radiography

Radiography is the process of creating an image by measuring the amount of x-ray radiation that passes through an object. The total attenuation of an x-ray in a given thickness of material depends on the photon energy, the material density, and the thickness through which it must pass [7]. In general, an x-ray that propagates through two materials of the same thickness is attenuated to a greater extent by the denser of the two. If an object consists of different materials, then measuring the differential attenuation of the x-ray beam over the area of the object provides sufficient information to generate an image, or radiograph, of the internal structure of the object.

A typical x-ray imaging system that can be used for diagnostic radiography is shown in Figure 1.1; it consists of an x-ray source, collimator, and x-ray detector. Figure 1.2 shows a typical x-ray source; electrons are emitted by the cathode, are accelerated by a large potential (~100 kV) and strike a rotating tungsten target. The collisions between the high-energy electrons and the atoms of the target result in the emission of broad-spectrum x-ray radiation. A collimator, which consists of 2 to 3 perforated lead sheets, is placed between the x-ray source and the patient to produces a beam of nearly parallel x-rays with uniform intensity that is incident on the area to be imaged. The intensity of the

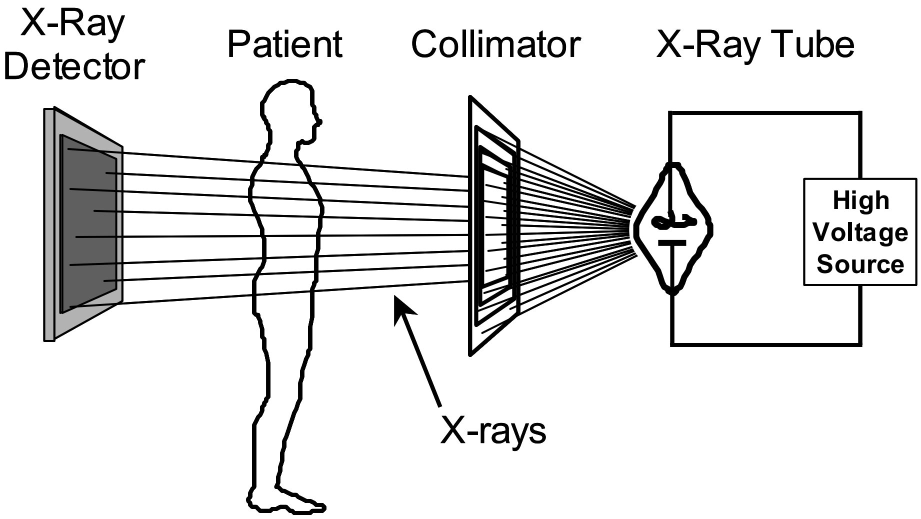

Figure 1.1 A typical projection radiography system consists of an x-ray source, collimator, and x-ray detector. The detector records the intensity pattern of the x-rays after they pass through the patient.

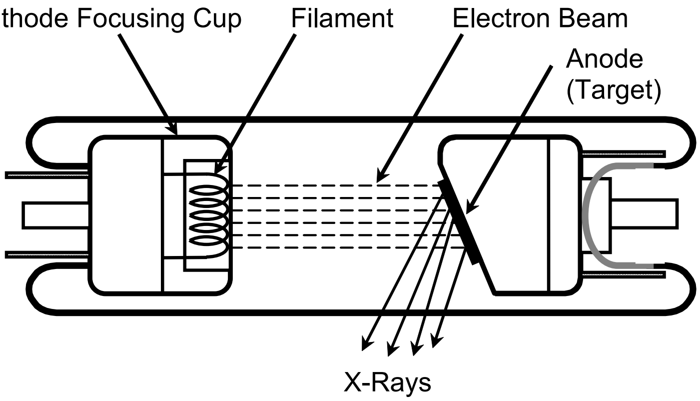

Figure 1.2 Schematic diagram of an x-ray source.

x-ray beam is modulated as it passes through the patient, and the resulting intensity pattern is projected onto the x-ray detector as shown in the figure. Since there is no practical method of focusing the x-ray beam, the detector area should be slightly larger than the size of the object being imaged.

The x-ray detector converts the intensity pattern of the incident x-ray beam into a measurable response that can be stored until the final image can be developed. The resulting image typically consists of variations in the amount of x-ray exposure registered by the detector over the area of the image. For example, the areas falling in the shadow of bone tissue appear darker or underexposed in the image because relatively few x-rays exit the patient and generate a small response in the detector. Conversely, areas falling under the shadow of soft tissue (i.e. fat and muscle) appear white in the image because a large number of x-rays exit the patient, and the detector registers a large response.

The requirements of the x-ray detector vary depending on the type of image being generated. Chest radiography, for example, requires an x-ray detector with a very large field of view and a very large dynamic range to accommodate the different penetration of x-rays into the lungs and mediastinum [4]. Mammography, on the other hand, attempts to visualize differences in soft-tissue contrast in order to enable the early detection of breast cancer, and the requirements for this form of imaging are much more stringent than for chest radiography. For example, high-resolution images are generally required to locate deposits as small as 0.1 mm in diameter [8].

In order to generate a digital x-ray image, the intensity of the incident x-ray beam must be sampled in both the intensity and spatial domains. In the intensity domain, the magnitude of the x-ray intensity is converted into a proportional electronic signal; this signal is then digitized so that it can be sent to a computer where the final image will be processed. In the spatial domain, the variation in the intensity signal over the area of the object represents the image information. Therefore, it is necessary to coordinate the digitized intensity signal with its position within the active imaging area of the detector. Any digital radiography solution therefore consists of two parts: the conversion of incident x-ray photons into an electrical signal, and the measurement of the spatial variation in this signal.

One method of generating an electrical signal from incident x-ray photons is to couple a phosphor screen to a photodetector, such as a silicon photodiode or CCD camera [7]. This type of detection is often referred to as *indirect conversion* because the electronic signal is indirectly generated from the pattern of visible light given off when x-rays strike the phosphor screen. It should be noted that a conventional film/screen detector can also be classified as an indirect detector for digital imaging; x-ray images that are captured on film may be converted to an electronic form by scanning the image hardcopy into a computer after it has been developed.

A *direct conversion* detector, on the other hand, directly records the electrical charge that results from the ionization of the atoms in the detector due to the incident x-ray photons. Examples of direct conversion x-ray detectors include gas chambers used for exposure meters, and photographic film (without the phosphor screen), which records x-ray image information through a photochemical process. Practical direct conversion detectors for digital x-ray imaging applications consist of a solid x-ray sensitive photoconductor material, such as a-Se, sandwiched between two metal electrodes to facilitate the application of a biasing potential. The absorption of x-ray photons in the solid layer generates electron hole pairs, which drift to the electrodes under the influence of the applied field. The magnitude of the charge that accumulates at the electrodes is proportional to the intensity of the x-ray beam, and this value may be measured electronically.

Direct detection has several advantages over indirect detection. The first is that the inherent resolution of a direct conversion detector is greater than the resolution of an indirect detector. This is because the x-ray generated charge carriers drift along lines of the electric field that are perpendicular to the image plane. The lateral spread of the x-ray generated response is minimal, so the generated response can be measured at the position in the image plane where the x-ray photon was absorbed. Indirect detectors on the other hand suffer from blurring due to the scatter of optical photons by the phosphor grains [7]. Secondly, the absorption efficiency of a solid state detector can be maximized with the suitable choice of the photoconductor material, operating bias, and the thickness of the photoconductive layer [9]. The sensitivity of an indirect detector is limited by the relatively low x-ray sensitivity of the phosphor screen.

A direct conversion digital flat-panel x-ray detector is one of the most promising developments in digital radiography [4]. This technology has recently been made possible with the development of amorphous silicon (a-Si:H) Active-Matrix-Array (AMA) devices for large area display applications [10]. An AMA circuit divides the imaging plane into an $M \times N$ array of discrete picture elements, or pixels. Each pixel contains a charge collection capacitor and a thin-film-transistor (TFT) switch. A direct conversion x-ray detector is created by coating a thick (~1mm) layer of a-Se onto the surface of the array.

In Figure 1.3, a cross sectional view of the pixel elements illustrates the principles of operation in a direct conversion flat panel detector. A top electrode is sputtered onto the surface of the a-Se layer to facilitate the application of a biasing potential. During the x-ray exposure, x-ray photons that pass through a patient generate electron-hole pairs (EHPs) in the a-Se layer due to the photoelectric effect. The EHP is then separated by the electric field F; electrons drift to the top electrode where they are collected by the battery, and holes drift to the bottom electrode where they are collected and stored by the pixel

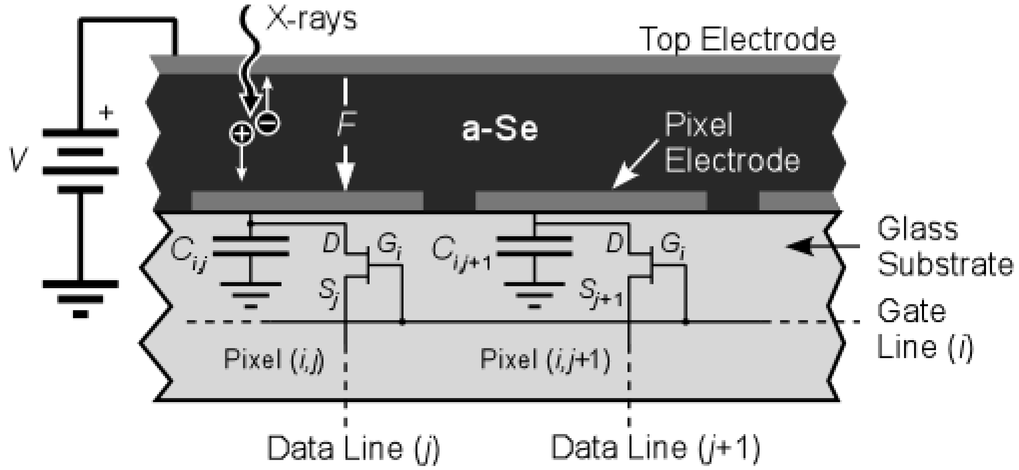

Figure 1.3 This cross-sectional view of the detector structure for a-Se based flat panel direct conversion digital x-ray detectors shows the details of two of the detector pixels.

capacitor C_{ij}. The positive charge signal Δq_{ij} that is stored on the pixel capacitor is proportional to the amount of incident radiation absorbed within the pixel area.

After the x-ray exposure, the pixel capacitors in the AMA contain a distributed charge signal that represents the x-ray image. The read out of this signal involves the coordinated operation of the TFT switches and is facilitated by the structure of the AMA circuit. A small section of an $M \times N$ flat panel AMA, where M is the number of rows and N is the number of columns in the array is shown in Figure 1.4. The gate terminals of each TFT in row i are connected to a control line, and the source terminals in column j are connected to a common data line. When control line i is activated, all TFTs in that row are turned on, and the charge signal on each row capacitor is read out on the N data lines. The parallel data streams are digitized, multiplexed, and transmitted serially to a computer. The charge read out then proceeds to the next row, and the process is repeated until all of the array rows have been processed in this manner.

The combination of an a-Se layer and an AMA produces a compact, self-scanning detector suitable for general radiographic imaging applications. Figure 1.5 shows a typical x-ray image obtained by a flat-panel x-ray image detector using an a-Se x-ray photoconductor. Since the image signal is read out using electronics that are embedded in the detector, there is no need to rely on complicated external scanning schemes and no

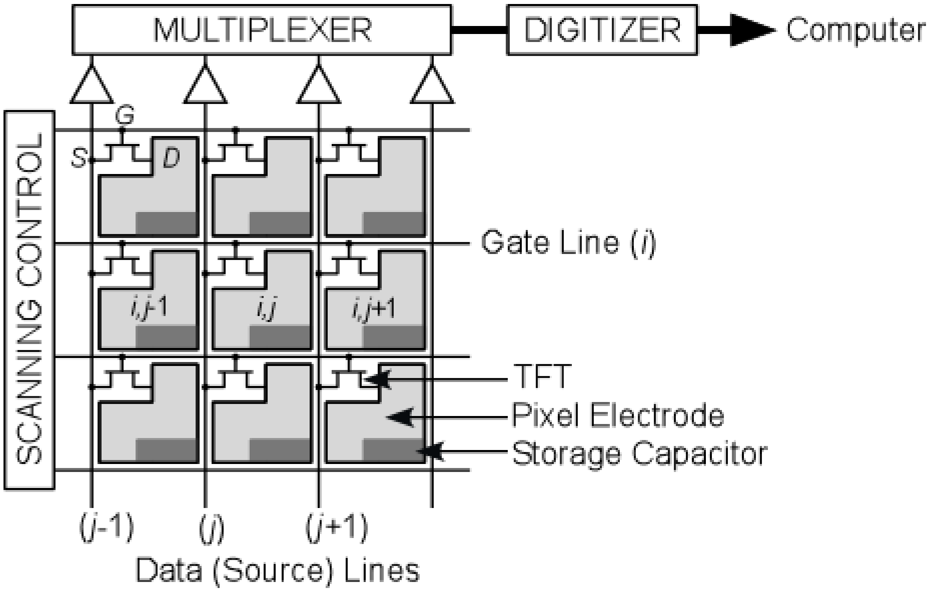

Figure 1.4 A small section of a thin-film transistor active-matrix-array used in flat panel x-ray image detectors with self-scanned electronic readout.

handling of the detector is required. Therefore, a flat panel x-ay detector can be used for real time imaging applications such as fluoroscopy. The image resolution of the detectors is determined by the pixel dimensions the AMA panel. The present size of AMA pixels is ~150μm, which is suitable for chest radiography. In the future, it is expected that AMA panels with a pixel size of 50μm will be possible in order to achieve the resolution necessary for mammography [6].

1.3 a-Se X-ray Photoconductors and Detector Performance

The x-ray sensitivity of a direct conversion flat panel detector is determined by the amount of charge that can be collected per unit of radiation that is incident on the detector. It depends critically on the following three properties of the photoconductor; the absorption coefficient, the electron-hole pair creation energy, and the charge mobility and lifetime in the material (transport properties). In this section, the mechanisms of x-ray sensitivity in x-ray photoconductors are described, and the properties of an ideal photoconductor material are presented.

Figure 1.5 An x-ray image of a phantom hand obtained from a direct conversion flat-panel X-ray image detector that uses a stabilized a-Se photoconductor. The AMA has 1,280 × 1,536 pixels. The image is provided courtesy of Sterling Diagnostic Imaging.

1.3.1 X-ray Absorption

The absorption coefficient α is a material parameter that determines the number of x-ray photons that are absorbed by a photoconductor due to the photoelectric effect. The fraction of incident x-ray photons that are absorbed by the photoconductor is

$$A_Q(E) = [1 - \exp(-\alpha L)] \qquad 1.1,$$

where L is the detector thickness and $\alpha = \alpha(E, Z, d)$ is the photoelectric absorption coefficient of the photoconductor material which depends on the energy E of the incident x-ray photons and the atomic number Z and density d of the photoconductor. The absorption coefficient typically decreases with increasing x-ray energy as E^{-n}, where, for example $n \approx 3$, and increases with Z; typically, $\alpha \propto Z^{m}$ where $m \approx$ 3-5. The initial interaction of an x-ray photon with an atom leads to the emission of an energetic electron from an inner core shell into the conduction band, so each shell marks the onset of absorption and is reflected by sharp edges in the $\alpha(E)$ curve. The identification of the atomic shell edges, i.e. K and L, facilitates the comparison of different photoconductor materials and their potential for use in mammography or chest radiology.

In order to minimize the x-ray exposure to the patient, the majority of the incident radiation should be absorbed within the photoconductive layer. This means that the absorption depth $\delta = 1/\alpha$, the amount of material that results in a 63% attenuation of the incident x-ray beam, should be much less than the thickness of the layer, i.e. $\delta < L$. The required thickness of the photoconductive layer depends on the specific radiographic application and the material used to detect the x-rays. For example, the x-ray radiation used in mammographic procedures typically has a mean energy of 20keV. If the required photoconductor thickness is taken as 2δ, then 100μm of a-Se would be required to sufficiently absorb the incident x-ray radiation. The x-ray beam energy used in chest radiography examinations is 60keV, which would require 2000μm of a-Se.

Ideally, the thickness of the photoconductive layer would be several times that of the absorption depth of the material; however, there are three factors that limit the maximum thickness of the layer. The first is that it is technically difficult and very expensive to fabricate very thick photoconductor layers that are uniform in their properties and free of defects [11]. Second, as the thickness of the photoconductive layer increases, so does the probability that an x-ray generated charge will be lost due to trapping before it reaches the collection electrode. This is referred to as s*hubweg*, or transport, limited sensitivity and will be discussed in more detail below. Lastly, the operating bias voltage increases in proportion to the thickness of the photoconductor. Large bias voltages (>10kV/μm) introduce additional technological problems such as supplying these voltages, dielectric breakdown in the panel, and protecting the TFT switches in the underlying AMA circuit.

1.3.2 Electron-Hole Pair Creation Energy

The absorption of an x-ray photon results in the creation of an energetic photoelectron that travels with a high velocity through the material. This electron collides with other atoms and causes further ionizations along its path, so that many electron-hole pairs are generated from the absorption of a single x-ray photon. The amount of charge ΔQ that is generated by the absorption of an amount of x-ray radiation energy ΔE is

$$\Delta Q = \frac{e\Delta E}{W_{\pm}} \qquad 1.2,$$

where $W_{\pm}$ is the electron-hole pair creation energy, the amount of radiation energy that is absorbed by the material to create a single electron-hole pair. This value must be kept as low as possible in order to maximize the sensitivity of the detector.

For amorphous semiconductors such as a-Se, Que and Rowlands [12] have shown that $W_{\pm}$ is related to the energy gap E_g of the material by $2.2E_g + E_{phonon}$, where the phonon energy term E_{phonon} is expected to be small. Additionally, $W_{\pm}$ has been shown to depend on the applied electric field, which likely arises from the recombination mechanism operating for the EHPs generated by the photoelectron; however, the exact nature of this recombination mechanism has yet to be determined, and is a topic of current study [11].

1.3.3 Charge Transport and Schubweg Limited Sensitivity

In order for x-ray generated charge to contribute to the image signal, it must move from the position where it was created to a collection electrode. An electron drifts from the point where it was created to the positive electrode with a finite velocity that is determined by the electron's mobility μ in the material and the magnitude of the electric field F. The transit time of the charge is the time it takes to travel from the point of creation to the collection electrode. Maximum collection efficiency occurs when all of the x-ray generated charge reaches an electrode. However, a-Se photoconductive layers contain a significant concentration of localized electron and hole traps. Carriers that become trapped are removed from the conduction band, become immobile, and do not contribute to the collected charge signal; this results in a decrease in the x-ray sensitivity of the x-ray detector. The probability that a charge carrier is trapped is determined by the reciprocal of the carrier trapping time (lifetime) τ.

The product of the mobility, lifetime, and operating field is defined as the carrier *shubweg* $\mu\tau F$, the average distance a charge carrier will drift before it is trapped. Ideally, the photoconductor thickness would be chosen so that $L << \mu\tau F$. However, this would sacrifice the x-ray absorption efficiency of the layer, as discussed earlier. The process of choosing a suitable photoconductor thickness for a particular imaging application is to balance the trade off between the high x-ray absorption requirement and the transport limited sensitivity, i.e. choose L such that $1/\alpha < L < \mu\tau F$. Thicker layers to maximize absorption can be used with large operating fields (~10V/μm) to increase the carrier schubwegs. However, increasing the operating field increases the magnitude of the dark current, which decreases the signal-to-noise (SNR) of the detector; it also leads to other technological difficulties as discussed in Section 1.3.1.

1.3.4 Ideal X-ray Photoconductor

The performance of direct-conversion x-ray sensors depends critically on the selection and design of the photoconductive layer. It is, therefore, instructive to identify the properties of an ideal x-ray photoconductor in order to develop better performing materials.

i. High x-ray absorption efficiency is required so that the majority of incident x-ray photons are absorbed within the detector thickness L to avoid unnecessary exposure to the patient. Any radiation that passes through the detector is essentially wasted.

ii. In order to generate as much charge as possible from the absorption of incident x-ray photons, the photoconductive layer should have a small value of $W_{\pm}$ (EHP creation energy).

iii. The dark current of the photoconductive layer should be negligible in order to maximize the signal-to-noise ratio (SNR) of the detector. The dark current can be minimized by using non-injecting contacts and using a material with a large band gap E_g. However, increasing E_g increases $W_{\pm}$, which is in conflict with (ii).

iv. There should be no bulk recombination of x-ray generated pairs as they drift to the collection electrodes. The rate of recombination, which is proportional to the concentration of generated charge carriers, is typically negligible provided that the x-ray exposure is not too high.

v. There should be negligible deep trapping of generated pairs, i.e. the carrier schubweg should be much longer than the photoconductor thickness, $\mu\tau F >> L$.

vi. The longest carrier transit time must be shorter than the access time of the pixel.

vii. These properties should not change or deteriorate with time as a consequence of repeated exposure to x-rays.

viii. The photoconductor layer should be economically coated onto a large area AMA circuit without damaging the electronics. For example, annealing the photoconductor material at temperatures above 300°C can damage the a-Si:H TFTs in the AMA panel. A large area detector is essential in diagnostic radiography applications because there is no practical way of focusing x-ray radiation.

X-ray sensitive amorphous semiconductors are appealing candidates for diagnostic flat panel systems because they can readily be prepared over areas as large as 40 cm × 40 cm. In particular, amorphous selenium (a-Se) alloys can be easily coated onto an AMA panel using conventional vacuum deposition techniques. The substrate temperature during the evaporation process is typically 60 – 70 °C, and will not damage the a-Si:H TFTs in the AMA. The resulting photoconductive layer exhibits acceptable x-ray absorption, good electron and hole transport properties, and small dark current compared to some of the competing polycrystalline materials such as PbI_2 [6]. It is, therefore, almost ideally suited for large area radiographic applications such as chest radiology and mammography. Furthermore, a-Se alloys have been extensively developed as large area photoreceptors for commercial use in electrophotographic and xeroradiographic applications, so there is a wealth of documented information on their electronic and physical properties [13, 14].

1.4 Research Objectives

The present investigation focuses on experimentally measuring the charge transport properties in alloys of a-Se suitable for use in direct conversion flat panel x-ray detectors. The carrier mobility μ and lifetime τ are important from a device standpoint as they determine the carrier shubweg and, hence, the performance of the x-ray detector. Charge transport investigations are also of scientific benefit as they can be used to provide insight into the fundamental physics of amorphous semiconductor materials. Therefore, convenient and accurate measurements of these parameters are important, not only for device characterization, but also to resolve the outstanding controversies surrounding the exact nature of the electronic structure in amorphous semiconductors [6].

1.4.1 Transient Photoconductivity Experiments

The charge transport properties of stabilized a-Se photoconductor films will be investigated using Time-of-Flight (TOF) and Interrupted-Field Time-of-Flight (IFTOF) transient photoconductivity experiments. The TOF technique is well established as a method for measuring the drift mobility in low mobility materials. Charge carriers are injected into an electroded sample using a short pulse of strongly absorbed radiation (i.e. light from a nitrogen laser). The drift of these carriers across the thickness of the film due to an applied field induces a transient photocurrent pulse in the external circuit. This signal may be captured to determine the mobility of the photoinjected carriers. The deep trapping time is determined by interrupting the drift of the carriers during transit by temporarily removing the applied bias. Examination of the dependence of the recovered photocurrent versus the interruption time can be used to determine the deep trapping time, and is the basis of the IFTOF experiment.

The initial goal of this project is to build an experimental system capable of performing both TOF and IFTOF measurements on stabilized a-Se photoconductor films. An IFTOF system for studying low mobility solids such as a-Se is technically difficult due to the large bias that must be applied during the carrier drift. The switching of this bias results in extremely large transient signals that can obliterate the desired photocurrent signal if they are not properly eliminated. A system based on the combination of transient suppressing rectifiers and a bridge circuit is used to eliminate the IFTOF switching transients. The theoretical principles of the TOF and IFTOF transient photoconductivity techniques are presented in Chapter 3, and a detailed description of the experimental setup is presented in Chapter 4.

1.4.2 Effects of Alloy Composition

The effects of alloy composition on the charge transport properties $\mu\tau$ are examined. Pure a-Se films are unstable and tend to crystallize over time. Therefore, the a-Se source material is typically alloyed with As (~0.5%) and doped with Cl (~20ppm) to produce device quality photoconductor films, and the resulting alloy is called *stabilized a-Se*. The effects of alloy composition on $\mu\tau$ have previously been studied using either TOF measurements or xerographic measurements. However, accurate measurement of the carrier lifetimes is difficult using these techniques. In the present study, both TOF and IFTOF measurements are used to measure $\mu\tau$ as a function of As and Cl content in the films for both holes and electrons. The results of this investigation will benefit device designers wishing to fabricate photoconductor layers with specific charge transport properties.

1.4.3 Bulk Space Charge

Flat panel x-ray digital detectors fabricated with a-Se are poised to make a significant impact on the field of diagnostic radiography. Therefore, there is current interest in studying the effects of x-ray exposure on the performance of these detectors. Two important temporal imaging characteristics of flat panel direct conversion detectors are ghosting and lag. Ghosting refers to the decrease in the sensitivity of the detector with exposure to x-ray radiation. Lag refers to the carry over of image information from previous x-ray exposures into subsequent image frames. Both of these effects may be attributed to the presence of trapped bulk space charge in the a-Se layer; that is, trapped charge carriers from a previous x-ray exposure. Lag results from the thermal release of the trapped charge, and ghosting may be attributed to the recombination of subsequently generated free carriers with the trapped charge.

In order to study the process that contributes to detector ghosting, a technique is developed to study the recombination of drifting holes with trapped negative bulk space charge (electrons). This technique uses a combination of the TOF and IFTOF transient photoconductivity techniques; the TOF measurement probes the space charge density profile in the sample, and the IFTOF measurement determines the recombination lifetime. The results are combined in order to calculate the recombination coefficient between drifting holes and trapped electrons. Previous studies have demonstrated that a Langevin process governs the recombination mechanism between drifting (free) holes and free electrons. It is expected that the same mechanism can be used to describe recombination between free holes and trapped electrons. Once the recombination coefficient is determined, the concentration of trapped charge can also be readily determined.

1.4.4 X-ray effects

The effects of x-ray exposure on the charge transport properties of biased a-Se x-ray photoconductive layers will be quantitatively investigated using TOF and IFTOF transient photoconductivity measurements. The charge mobility and lifetime are important x-ray photodetector parameters as they determine the photodector schubweg, and hence, the x-ray sensitivity of the device. Changes in the transport properties with x-ray exposure will therefore be reflected in the performance of the detector being modified. The results from this investigation will aid in efforts to model the performance of a-Se direct conversion flat panel detectors.

1.5 Thesis Outline

This chapter provides an introduction to the principles of digital radiography and describes the current developments in flat panel direct conversion x-ray detector technology. Such detectors, fabricated by depositing a layer of x-ray photoconductor material (i.e. a-Se) onto an active-matrix-array (AMA), are compact, self-scanning, and produce high quality images immediately following an x-ray exposure on a video monitor. The realization of the benefits of digital radiography is driving continued research into the fundamental physics of x-ray photoconductor materials as their properties determine the performance of the detector. Currently, a-Se is the most suitable photoconductor material for large area imaging applications such as chest radiography and mammography. This is primarily because a-Se alloys may be economically fabricated as thick, large area films with uniform properties at low substrate temperatures; they are, therefore, ideally suited to coat AMA panels. Further, a-Se films exhibit good intrinsic x-ray sensitivity, good charge transport properties, and small dark current.

The remainder of this thesis is separated into five chapters. In Chapter 2, the nature of the electronic bonds in the a-Se solid are described, and a band model that can be used to understand the electronic and optical properties of a-Se and its alloys is derived. In Chapter 3, the theoretical principles of the TOF and IFTOF transient photoconductivity techniques are presented, and expressions for the TOF transient photocurrent under a variety of trapping conditions (i.e. set of discrete traps, a continuous trap distribution) are developed. The experimental system used to capture the TOF photocurrent signals and to perform the IFTOF measurement is described in detail in Chapter 4. This chapter also includes a description of the deposition of device quality stabilized a-Se films used in the subsequent investigations. The charge carrier transport properties in a variety of samples are investigated to determine the effects of alloy composition and x-ray irradiation on the properties of stabilized a-Se photoconductor films; these results are presented in Chapter 5. The conclusions from the experimental results are presented in Chapter 6 along with suggestions for future work.

2. AMORPHOUS SELENIUM

> *Historically [photoconductivity] was first reported by Willoughby Smith, an electrician for a telegraph company. By one of those curious coincidences, his observation was made in the element selenium which would prove so important in the development of xerography. Smith, using rods of selenium as resistors in the testing of submarine cables, found that their resistance changed depending on whether they were enclosed in a light-tight box or exposed to a light source.* [13]

Amorphous selenium (a-Se) and its alloys have been well studied because of their importance in commercial xerography during the 1960s and 1970s. Presently, research in these materials is enjoying a renaissance of sorts due to the interest in developing digital flat panel x-ray detectors for medical imaging applications. A photoconductive layer of a-Se, which converts incident x-ray photons directly into electronic charge, can easily be fabricated in the large areas that are required for imaging applications such as chest radiology. The x-ray sensitivity of such a detector is related to the optical and electronic properties of the photoconductive a-Se layer. Therefore, a thorough understanding of the properties of a-Se is necessary in order to optimize the performance of these detectors.

A theoretical framework for understanding the properties of materials can be derived by applying a quantum mechanical analysis to the bonding arrangement of the atoms in the material. This results in the band theory for solids, which is so important for understanding the principle of operation of modern solid-state electronic devices. In crystalline solids, the periodicity of the atomic network leads to mathematical simplifications that may be exploited to derive a band model that describes the electronic and optical properties in these materials. Amorphous materials, however, lack long-range periodicity in their atomic network, so it is difficult to derive a framework that describes their properties. Nevertheless, a band model for amorphous semiconductors can be derived by noting their similarities to crystalline semiconductors and through experimental observation of their electronic and optical properties.

2.1 The Atomic Structure of Amorphous Semiconductors

A solid consists of a three dimensional network of atoms interconnected by atomic bonds. These bonds consist of interactions between the wavefunctions of the outer shell, or valence, electrons of the atoms when they are brought close together to form a solid. In semiconductors, atomic bonds are formed when two or more atoms share their valence electrons to complete the sub-shells of each atom. The wavefunctions of these electrons are no longer isolated to a single atom, but are now extended over the volume of the solid. This type of bond is known as a covalent bond, and the number of nearest neighbors for a given atom in the solid is known as the coordination number of that atom.

The crystalline and amorphous bonding arrangements for semiconductors are illustrated two-dimensionally in Figure 2.1. The dots in the figures represent the equilibrium positions about which the atoms oscillate, and the lines represent the bonds

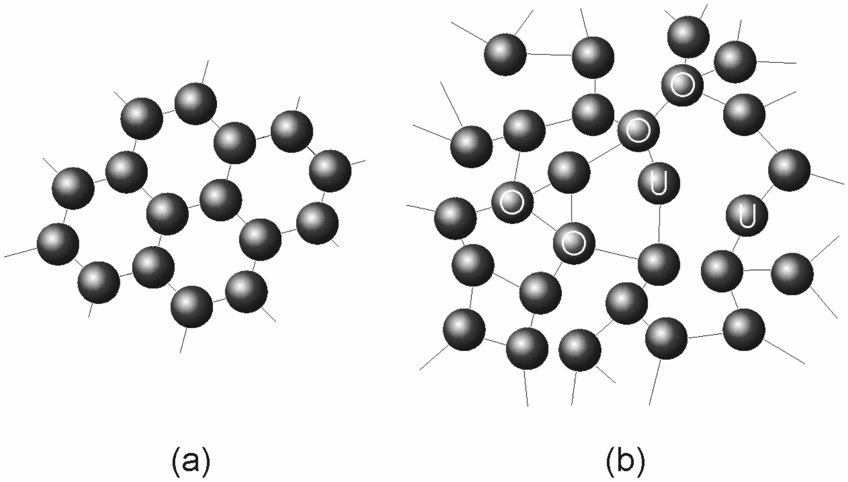

Figure 2.1 A 2-dimensional representation of a three-fold coordinated atomic structure is shown for (a) a crystalline semiconductor and (b) an amorphous semiconductor. Over-coordinated (O) and under-coordinated (U) defects are shown for the amorphous case.

between an atom and its nearest neighbors. The crystalline structure is characterized by a highly ordered arrangement of atoms as depicted in Figure 2.1 (a). Each atom in the network has the same coordination number, and the bond lengths and bond angles between the atoms are identical. The order exists to a high degree throughout the crystal so that, ignoring the surface states, the equilibrium position of each atom in the network is precisely known from any other position in the network. This type of order is described as long-range order because the periodicity of the network extends throughout the bulk of the solid.

In an amorphous semiconductor, slight variations exist in the bond length and bond angle between the atoms in the network. These slight variations are sufficient to destroy the spatial periodicity of the network over distances greater than a few atomic radii as depicted in Figure 2.1 (b). The similarity of the short-range order results in a similar electronic structure for the amorphous and crystalline phases of a semiconductor. However, the disorder in the network introduces localized electronic states; states where the electron wavefunction is localized to a particular position in the semiconductor. The energy location and density of these localized states have a profound impact on the electronic and optical properties of amorphous semiconductors.

The atomic structures of crystalline and amorphous semiconductors also contain defects that affect their properties. In a crystalline network, any atom that is not in its equilibrium position is a defect. In the amorphous structure, the only specific structural feature of the atoms is the coordination number of an atom, which is often referred to as the normal structure bonding (NSB) of the atom. Since there is no correct position of an atom, one cannot say whether a specific structure is a defect or not [15]. The elementary defect of an amorphous semiconductor, therefore, is a coordination defect when an atom has too many or too few bonds. An under-coordinated (U) and an over-coordinated (O) defect are shown in Figure 2.1 (b). These defects introduce additional localized electronic states in the electronic structure of the amorphous material.

2.2 The Band Theory of Amorphous Semiconductors

The band model is an important concept in solid-state physics that can be used to explain the electronic and optical properties of semiconductors. It is derived from a quantum mechanical treatment of the behavior of electrons as a large number of atoms are brought together to form a solid. In a single atom system, quantum theory suggests that the energy of the electron is quantized into discrete energy levels or states. When atoms form a solid, the electron energy states associated with the individual atoms combine in such a way to form almost continuous bands of allowable energy states. These band states are described by a function called the density of states $g(E)$, which defines the number of electron states per unit energy per electron at energy E.

The density of states for crystalline semiconductors, shown in Figure 2.2 (a), can be derived quantitatively by applying the principles of quantum mechanics and using mathematical simplifications resulting from the periodicity of the crystal structure. The predominant features of the band diagram in Figure 2.2 (a) are the two bands of allowed energy states separated by a forbidden region or *band gap*. The lower band is fully occupied by the electrons involved in the covalent bonding of the semiconductor and is called the valence band. The upper band of states, however, is almost completely devoid of electrons. When an electron acquires sufficient energy to surpass the band gap, it becomes free to contribute to an electrical current. This band is, therefore, called the conduction band. In Figure 2.2 (a), E_C and E_V are the energies that denote the conduction and valence band edges respectively, and E_F is the Fermi Level.

A quantitative development of the electronic structure of amorphous materials is much more difficult because of the absence of any long-range topological order. In fact, the disordered structure of amorphous semiconductors led many to believe that the amorphous band diagram was vastly different from the crystalline band diagram. However, when it was discovered that amorphous solids possessed the same basic electronic and optical properties as their crystalline counterparts [16], it was concluded

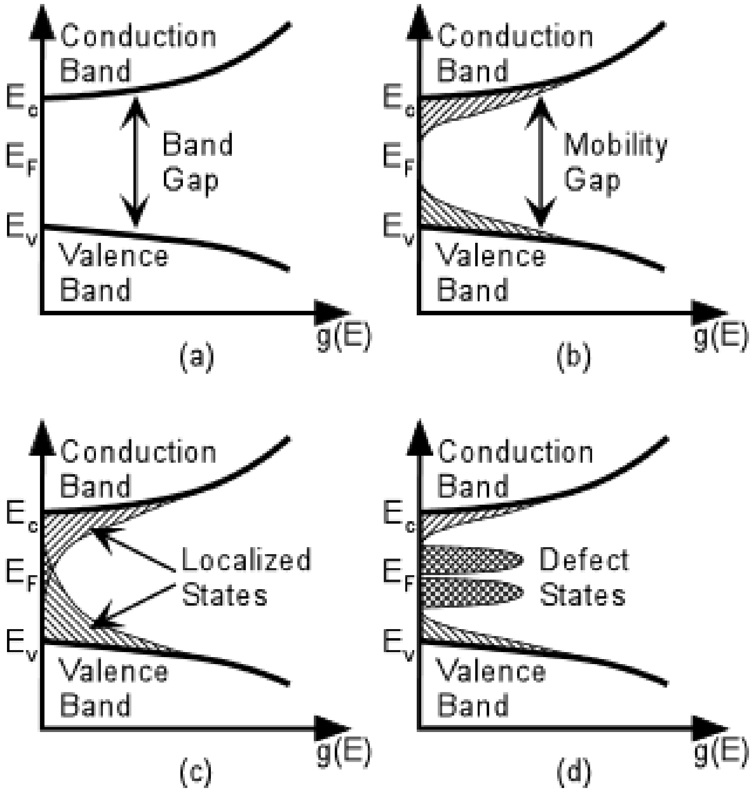

Figure 2.2 Density of States (DOS) models for crystalline and amorphous semiconductors. (a) In the crystalline case, two extended state bands are separated by a forbidden energy region called the *band gap*. (b) The initial DOS model for amorphous semiconductors as proposed by Mott; the disorder of the amorphous network introduces localized states that encroach into the gap region. (c) The CFO model for amorphous semiconductors showing localized states that extend continuously through the gap region. (d) Marshall and Owen argued that defects in the structure would contribute a significant number of localized states deep in the gap region.

that only short-range order in the atomic structure is necessary for the band theory to be applicable.

The first semi-quantitative step in generalizing a band model for amorphous materials was taken by N.F. Mott in the 1960s [17]. He noted that the electronic structure of crystalline semiconductors has the following universal features:

1. the individual electrons within the crystal can be described by extended Bloch wave-functions that possess long range order in both amplitude and phase, and
2. the allowable electron energies fall into bands of allowed states which are separated by a well defined gap of "forbidden" energies.

Mott assumed that amorphous semiconductors had similar universal characteristics. He postulated that the Bloch wavefunctions for electrons in an amorphous solid had long-range order in their amplitudes, but only short-range order in their phases. This difference would result in an encroachment of localized electron states into the forbidden gap region.

Mott's hypothesis was based on the work of P. W. Anderson, who in 1958, quantitatively showed that sufficient structural disorder could produce characteristic solutions to the Schrödinger equation that are localized in space [18]. These Anderson states are not associated with definite imperfections, but are the result of the randomness of the network; the number and energy spread of these localized states increases as the randomness of the network increases.

The band model that Mott proposed for the density of states in an amorphous semiconductor is illustrated in Figure 2.2 (b). The amorphous semiconductor's conduction and valence band states extend throughout the volume of the solid. However, the disorder of the network introduces "tails" of localized states that begin at the band edges E_v and E_c and trail off into the forbidden gap region. Mott postulated that the transition from the localized tail states to the extended band states is well defined [19], corresponding to an abrupt change in the electron mobility. Electrons in the extended states move with a finite band transport mobility determined by the electron's effective mass in the solid. Electrons in the localized tail states, on the other hand, move with a mobility that is controlled by thermally activated tunneling between states. The mobility in the localized states, therefore, disappears as the temperature approaches absolute zero. This transition in the mobility leads to the concept of a *mobility gap* for amorphous semiconductors that is analogous to the *band gap* in crystalline semiconductors.

The model put forth by Mott was extended by Cohen, Fritzsche and Ovshinski [20] who argued that topological and composition disorder would introduce considerably more disorder in amorphous semiconductor alloys than was originally expected. Their band model, referred to as the CFO model, is shown in Figure 2.2 (c). This model is characterized by the formation of localized tail states that extend much deeper into the mobility gap of the semiconductor and overlap in the region of the Fermi level. Despite the continuum of electronic states throughout the gap, metallic conduction properties are not expected since these gap states are highly localized in space.

The structure of amorphous semiconductors also contains atoms that are coordinated differently from the normal structure bonding (NSB) of the network. Since the connectivity of the amorphous network is well defined on a local basis, there can be well-defined localized defects such as dangling bonds, chain ends, vacancies, substitutional impurities, and interstitials. Such defects lead to additional localized states within the mobility gap of the material.

It was originally assumed that the intrinsic disorder of the amorphous structure introduced a sufficiently large density of states in the gap to obscure any effects from the defect states. However, Marshal and Owen [21] proposed that defects in the NSB of the network would cause a significant density of mid-gap states, as shown in Figure 2.2 (d). In this band model, the position of the Fermi level is determined by bands of donor- and acceptor-like states that appear in the upper and lower half of the mobility gap respectively. As the solid forms, these states adjust themselves by a self-compensation mechanism so that their concentrations are nearly equal, and the Fermi level remains near the center of the gap. Even small concentrations of these states can affect the band model of a semiconductor, so their origin is of particular interest for predicting the electronic properties of a material.

2.3 The Atomic Structure of Amorphous Selenium

Selenium is a member of a family of elements called chalcogens, which are located in the group VI column of the periodic table. The outermost shell of the atoms in this group can accommodate up to 8 electrons, two in the s-states and up to six in the p-states. Selenium, with an atomic number of thirty four (Z = 34), has twenty eight inner core electrons and six valence electrons that occupy the eight possible states in the outermost shell. The two electrons in the s-states form a lone pair (LP) and do not participate in bonding. Chalcogen elements normally have a p-state lone pair in addition to the s-state lone pair, and these are both commonly referred to as non-bonding states. This leaves two valence electrons in the p-states that are available for covalent bonding with other atoms to form a solid. Therefore, Se atoms in a solid have a two-fold coordinated bonding configuration with an optimum bond angle of 105° [22]; this is the lowest energy configuration of the Se atom.

The two-fold coordinated bonding configuration of selenium results in two forms of the crystalline phase of the solid, which are known as α-monolclinic Se (α-Se) and trigonal Se (γ-Se). The α-monoclinic structure is composed of Se_8 rings while the trigonal structure consists of parallel, spiral Se_n molecule chains. In the amorphous phase of selenium, it was originally assumed that the structure would contain a mixture of these ring-like and chain-like formations randomly distributed throughout the solid. However, structural studies of a-Se and its alloys favor a "random chain model" in which the individual atoms of the solid are arranged in a two-fold coordinated chain structure where the magnitude of the dihedral angle ϕ remains constant, but its sign changes randomly [22,23]. The dihedral angle, as illustrated in Figure 2.3, is defined as the angle between two adjacent bonding planes. Its definition therefore involves four atoms, and it is

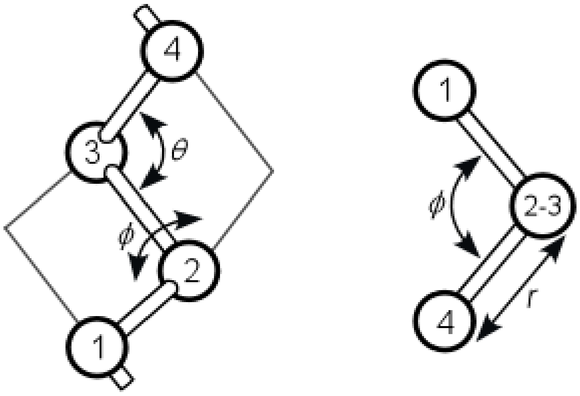

Figure 2.3 The selenium chain molecule and the definition of the dihedral angle ϕ. The definition involves an angle between bonding planes and thus requires four atoms as illustrated. It is observed looking down the bond joining atoms 2 and 3. The bond angle θ and the bond length r are also defined in the figure.

observed by looking down the bond connecting the second and third atom in the chain.

In the crystalline phase of selenium, the positions of the atoms are fixed by symmetry, the bond length *r*, and the bond angle θ. Consequently, the magnitude of ϕ is constrained as a function of *r* and θ. In γ-Se , the dihedral angle rotates in the same sense in moving along a chain to form a spiral pitch of three atoms. In α-Se, the sign of ϕ alternates as you move around the ring. In a-Se, random variations in the sign of the dihedral angle lead to regions that are ring-like in structure and regions that are chainlike in structure. If + and – are used to indicate the relative phase of the dihedral angles, then a sequence of the type +-+- is ring-like, and a sequence of +++ or --- is chain-like [22].

Figure 2.4 shows a selenium chain that can be characterized as +++-+-+---. This model assumes only local molecular order within the selenium chain, and it has been successfully used to explain the vibrational spectra of a-Se to account for the presence of various Se_8-like spectral features in the infrared absorption and Raman scattering spectra without invoking a mixture of Se_n and Se_8 members for the structure. Other structural studies of a-Se also support this random chain model [24, 25].

A feature common to all amorphous chalcogenide solids is the presence of defects

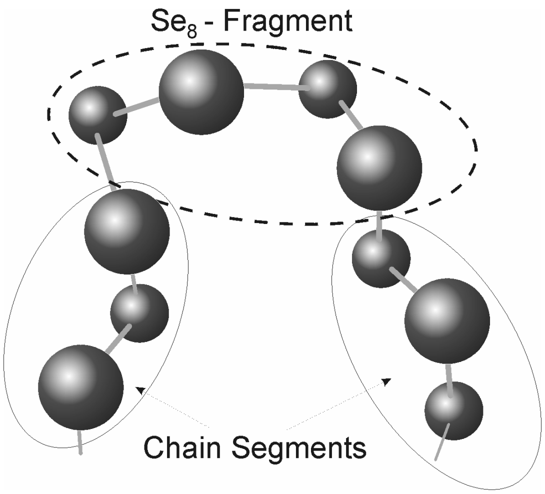

Figure 2.4 The random chain model of the structure of a-Se showing localized regions that are ring-like and chain-like.

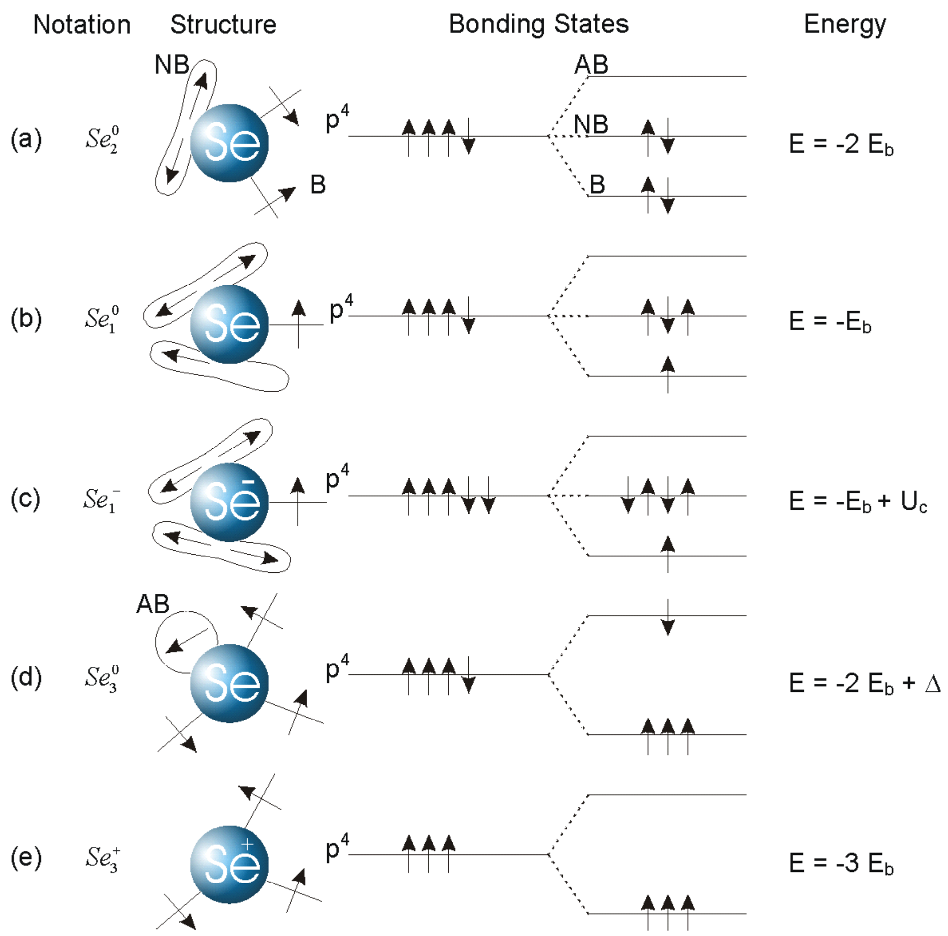

Figure 2.5 The structure and energy of simple bonding configurations for selenium atoms. Straight lines represent bonding orbitals, lobes represent lone-pair (nonbonding) orbitals, and circles represent antibonding orbitals. The energy of a lone-pair is taken as the zero energy. This figure is adapted from [26].

corresponding to some of the atoms being under- and over- coordinated. Several different bonding configurations for Se have been identified and are shown in Figure 2.5, which has been adapted from [26]. The two-fold coordinated Se_2^0 is the lowest energy bonding state, and is involved in the normal structure bonding of the solid. The lowest energy electrically neutral defect, the trigonally coordinated Se_3^0 atom, has three valence electrons in bonding states and one electron in an anti-bonding state. Another neutral defect, the singly coordinated Se_1^0 chain end, possesses three valence electrons in nonbonding states and one electron available for bonding.

The absence of a detectable electron spin resonance (ESR) signal, however, indicates that there are no unpaired (dangling) bonds in the a-Se structure [27, 28]. This suggests that there are very few of these neutral defects. However, it is believed that there is a large concentration ($10^{18} - 10^{20}$ cm^{-3}) of thermodynamically derived charged structural defects known as valence alternation pairs (VAPs). These defects are indicated in Figure 2.5 as Se_1^- and Se_3^+. These types of defects are prevalent because the formation of a diamagnetic pair of charged over- and under-coordinated VAP centers is energetically more favorable than the formation of singly or triply coordinated defects, Se_1^0 and Se_3^0. For example, a dangling bond Se_1^0 can lower its energy by approaching the lone pair on the normally coordinated Se_2^0 atom to generate an intimate valence alternation pair (IVAP). The diffusion of the resulting species can further reduce the Gibbs free energy of the solid. Thus the reaction

$$\mathrm{Se}_1^0 + \mathrm{Se}_2^0 \rightarrow \mathrm{Se}_1^- + \mathrm{Se}_3^+ \qquad 2.1,$$

is exothermic because the lone pair electrons have been absorbed into the dative bonding scheme of the Se chain. Figure 2.6 is a schematic representation of a typical a-Se structure with an IVAP center and illustrates the lowest energy defect in chalcogen glasses.

Many photoelectric properties of a-Se and its alloys can be qualitatively explained

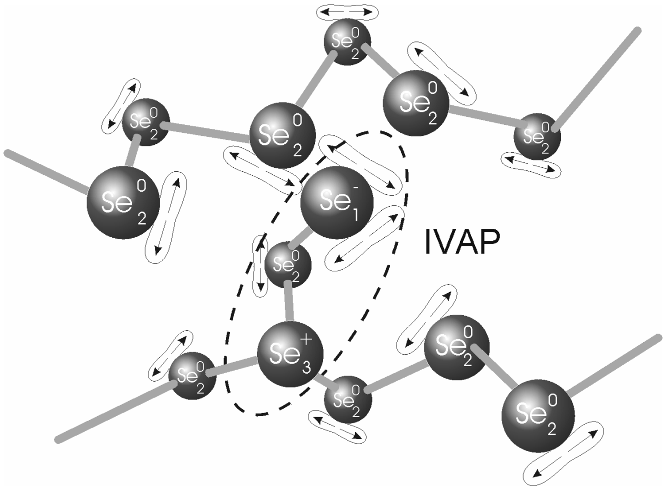

Figure 2.6 Illustration of the a-Se structure detailing an IVAP defect.

by using concepts based on VAP- and IVAP-type defects, and on the interconversions between the normally bonded (two-fold coordinated) Se atoms and these defects. The physics of such processes has been extensively discussed in the literature [29,30]. Their existence and the possible defect reactions that can occur in the structure have led to many important predictions and much insight in to the behavior of chalcogenide semiconductors. For example, the linear dependence of the steady state photoconductivity on the light intensity in a-Se has been interpreted via photoinduced IVAP-type centers [31].

2.4 Properties of Stabilized a-Se

The properties of the amorphous form of selenium and its alloys have been widely studied because of their technological importance in xerography during the 1960s and 1970s. The experimental observations of the electronic and optical properties of a-Se are mainly interpreted through its density-of-states (DOS) band diagram. Unfortunately, even though the properties of a-Se photoconductors are well studied, there are still a number of controversies surrounding the exact shape of the DOS function, and, therefore, the exact nature of the electron and hole transport. This section will describe some of the properties of a-Se in relation to the currently accepted DOS function.

2.4.1 Density of States and Carrier Transport in a-Se

Figure 2.7 illustrates the current accepted model for the DOS in a-Se, and it has been derived from various experiments such as time-of-flight (TOF) transient photoconductivity, xerographic cycled-up residual voltage decay and xerographic dark discharge. Originally proposed by Abkowitz [32] in 1988 as an extension of the Owen-Marshall DOS model described above, its notable features are a decaying density of localized states from the band edges, with peaks close to the valence and conduction band edges. These peaks are known as shallow hole and electron traps respectively. Near the Fermi level, there are two additional peaks in the DOS, which are known as deep traps.

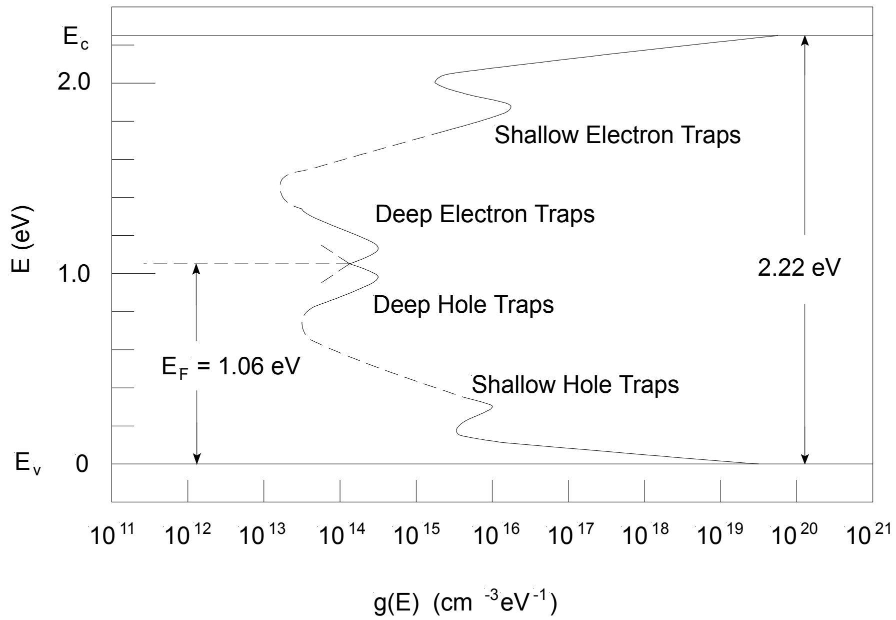

Figure 2.7 The density of states function for amorphous selenium as determined from experimental measurements [32].

The mobility gap for amorphous selenium is effectively 2.22 eV as indicated in the diagram.

Experimental observations of the carrier drift mobility in a-Se indicate that both holes and electrons are mobile and thermally activated at low temperatures. Furthermore it is believed that the carrier drift mobility is shallow trap controlled [33]. This means that the effective carrier drift mobility μ is the microscopic mobility μ_o in the extended states reduced by trapping and release events involving the shallow traps, i.e.,

$$\mu = \theta\mu_o = \frac{p_{free}}{p_{free} + p_{trapped}}\mu_o \qquad 2.2.$$

In Equation 2.2, θ is the mobility reduction factor [34], p_{free} is the concentration of carriers in the transport band, and $p_{trapped}$ is the concentration of carriers occupying shallow traps. It is assumed that $p_{trapped}$ is in equilibrium with p_{free}.

For a discrete set of monoenergetic shallow traps, it can be shown that the equation for the hole mobility becomes

$$\mu = \mu_o \left[1 + \frac{N_t}{N_v} \exp\left(\frac{E_t}{kT} \right) \right]^{-1} \approx \mu_o \frac{N_v}{N_t} \exp\left(-\frac{E_t}{kT} \right) \qquad 2.3,$$

where N_t is the shallow trap concentration, N_v is the density of states at the valence band mobility edge E_v, and E_t is the energy depth of the shallow traps from E_v. At sufficiently low temperatures, the mobility can be expressed by the Arhenius form assuming that $p_{trapped} >> p_{free}$. As the temperature is increased, μ approaches μ_o.

The location of the shallow traps in Figure 2.7 can be determined by curve fitting Equation 2.3 to the experimental observations of the carrier drift mobility versus temperature [6]. It has been shown that the peak in the concentration of shallow hole traps occurs at E_t-$E_v \approx 0.29$ eV, and that the microscopic mobility for holes is related to temperature with an almost diffusive index (i.e. $\mu_o \sim T^{-n}$, where $n \approx 1$). This gives a microscopic mobility for holes in the transport band that is ~ 0.3 – 0.4 cm^2/Vs at room temperature [35, 36] which agrees with μ_o reported from Hall effect measurements [37]. The peak in the shallow electron trap density is similarly derived and occurs at E_c-$E_t \approx$ 0.35 eV. Both the hole and electron shallow trap densities have been shown to decay almost exponentially from the transport band edges from picosecond-resolution transient photoconductivity measurements using microwave strip-line techniques [38].

The peaks in the energy distributions of the deep traps in Figure 2.7 have been measured by photoinduced discharge measurements and cycled-up xerographic residual voltage measurements. The peak in the deep hole trap density occurs at 0.87 eV from E_v and the peak in the electron traps occurs at 1.22 eV from E_c. The integrated concentrations of these deep states are small compared to similar amorphous semiconductors, which makes a-Se a good candidate for x-ray photodetector applications. Deep localized hole states have also been measured by cycled time-of-flight experiments with a peak at ~0.85 eV [39].

It has been shown that both the shallow and deep localized states in the mobility gap are due to various structural defects that are thermodynamically stable at room temperature [40, 41, 42]. The deep states are of particular interest as they control the carrier lifetimes, or trapping times, and thus determine the carrier shubweg $\mu\tau F$ and hence, the x-ray sensitivity of the photoconductor as discussed in Chapter 1. Experiments at Xerox in the 1980s showed that these states are derived from equilibrium defects [40] and, therefore, cannot be eliminated by careful preparation methods or by purification of the source material. The exact nature of traps in the mobility gap of a-Se has not been conclusively resolved, but it is currently accepted that they are due to VAP defects in the atomic structure of a-Se (i.e. positively charged over-coordinated Se_3^+ and negatively charged under-coordinated Se_1^- centers).

The effects of impurities and alloying elements on the transport properties of a-Se have been well documented. Pure a-Se is unstable and tends to crystallize over a period of time, which varies from months to years depending on the ambient conditions [6]. It was found that the rate of crystallization could be reduced by alloying pure a-Se with small amounts of As (0.2%-0.5%). Since As atoms have a valency of III, they are triply bonded and link Se chains which increases the viscosity of the amorphous structure and prevents crystallization. However, the addition of As increases the number of VAP defects that act as hole traps, so the hole lifetime decreases. This can be compensated for by adding a halogen (e.g. Cl) in the parts per million range.

A thermally stable film with good hole and electron transport can be achieved by adjusting the amount of As and Cl in order to balance the number of VAP defects that lead to carrier traps. The resulting material is called *stabilized a-Se*, and the nominal composition is indicated, for example, as a-Se:0.3%As +20ppm Cl. The compensation effect of As and Cl on the charge transport properties of a-Se photoconductors is currently being studied as there are fundamental issues that have yet to be fully resolved [35, 43]. Table 2.1 summarizes the transport properties of a typical stabilized a-Se photoconductor film.

It should be noted that new experiments based on post-transit transient photoconductivity techniques have cast substantial doubt as to the veracity of the DOS in

Table 2.1 The transport properties of stabilized a-Se (a-Se 0.2-0.5% As +10-40ppm Cl) photoconductor films.

Property	**Typical Range**	**$\mu\tau F$ @ 5 V/μm**	**Comment**
Hole mobility **μ_h (cm^2/Vs)**	0.12 – 0.14		well reproducible, probably shallow trap controlled
Electron mobility **μ_e (cm^2/Vs)**	0.003 – 0.006		decreases rapidly with As addition, probably shallow trap controlled.
Hole lifetime **τ_h (μs)**	20 – 200	1.2 - 12 mm	depends on the substrate temperature
Electron lifetime **τ_e (μs)**	200 – 1000	0.3 – 1.5 mm	sensitive to small quantities of impurities
Hole range **$\mu_h\tau_h$ (cm^2/V)**	2×10^{-6} to 2×10^{-5}		substantially higher than PbI_2
Electron range **$\mu_e\tau_e$ (cm^2/V)**	1×10^{-6} to 6×10^{-6}		somewhat higher than PbI_2

Figure 2.7 [44]. The results from these experiments suggest that the peaks in the densities of the shallow traps occur at 0.55 eV from the conduction band edge and 0.40 eV from the valence band edge, and that the carrier mobility is determined by a distribution of shallow localized states that extends over an energy range ΔE from the band edges, i.e.,

$$\mu = \mu_o\left(\frac{\Delta E}{kT}\right)^n \exp\left(-\frac{\Delta E}{kT}\right) \qquad 2.4.$$

In Equation 2.4, it is assumed that the density of localized states decays with energy from N_v at E_v to zero at $E_v + \Delta E$, i.e. $N(E)\propto(\Delta E - E)^n$ and that $p_{trapped} >> p_{free}$. Note that the distributions of the deep states are not accessible within the limits of the post transient photocurrent experiment, and are, therefore, not defined by this model. Clearly, further research is needed to clarify the shape of the DOS and, therefore, the nature of carrier drift in a-Se and its alloys.

2.4.2 Optical properties

The conductivity of a-Se, like many other semiconductor materials, increases considerably with exposure to light due to an increase in the charge carrier density in the material. This phenomenon is known as photoconductivity; an incident optical photon with sufficient energy can excite an electron from the valence band into the conduction band. The probability that absorption occurs is determined by the optical absorption coefficient α of the material. This value depends on the incident photon energy and the magnitude of the DOS at the band edges. If the energy of the incident photon is less than the band gap, negligible absorption will occur. As the energy of the incident photons surpasses the value of the band gap, the magnitude of the absorption coefficient increases rapidly.

Experimental studies have shown that the optical absorption coefficient of a-Se exhibits an Urbach edge of the form $\alpha(h\nu) = 7.35 \times 10^{-12} \exp(h\nu/0.058\text{eV})\text{cm}^{-1}$, which corresponds to the excitation of charge carriers from the mid-gap localized states into the extended states [45]. At higher photon energies, the absorption coefficient obeys $\alpha(h\nu) \sim (h\nu - E_o)$ [46], where $E_o \approx 2.05$eV is the optical band gap at room temperature. This behavior has been attributed to the sharp rise in the density of states at the band edges. A dependence following Tauc's law $\alpha(h\nu) \sim (h\nu - E_o)^2$ has also been observed with an optical bandgap $E_o \approx 1.9$eV [47].

The absorption of an optical photon results in the generation of an electron-hole pair (EHP); an electron excited to the conduction band leaves a void, or hole, in the valence band. These optically generated charge carriers may contribute to the conduction current in the presence of an electric field. The quantum efficiency η determines the probability that a generated EHP is separated by the field, and it is another important optical parameter of semiconductor materials. EHPs that are not separated by the field quickly recombine and do not contribute to the conduction current. The quantum efficiency in a-Se has been found to exhibit a strong field dependence, even for photon energies well above the optical gap. The dependence of α and η on the photon energy $h\nu$ and electric field E is shown in Figure 2.8.

The mechanism behind the field dependent quantum efficiency observed in a-Se can be explained by the Onsager theory for the dissociation of photogenerated EHPs [48]. The Onsager theory essentially calculates the probability that an EHP will diffuse apart for a given electric field F and temperature T. The quantum efficiency can be expressed as $\eta = \eta_o f(F, T, r_o)$, where $\eta_o(h\nu)$ is the quantum efficiency of the intrinsic photogeneration process, $f(F,T,r_o)$ is the probability that an EHP will separate, and r_o is the initial separation of the photogenerated pair.

2.5 Summary

A framework for understanding the electronic and optical properties of amorphous selenium and its alloys was reviewed in this chapter. The modern band

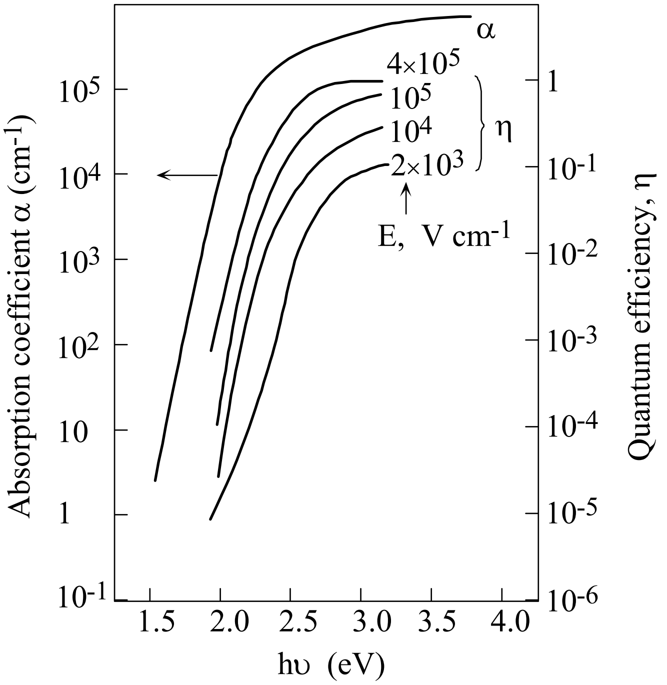

Figure 2.8 Absorption Coefficient α and quantum efficiency η in a-Se as a function of incident photon energy $h\nu$ at various applied fields [48].

theory of solids can be derived from a quantum mechanical treatment of the relationship between the electrons that are involved in bonding when a large number of atoms are brought together to form a solid. An analytical derivation of the band model for amorphous semiconductors is difficult because there is no long-range periodicity in the amorphous network. However, experimental observations of the electronic and optical properties in these materials have shown that a band model, similar to that for crystalline semiconductors, can also be applied to amorphous semiconductors.

In order to derive the band model for a-Se, the common bonding arrangements that occur when selenium atoms form a solid are also presented in this chapter. It was shown that random variations in the dihedral angle of the divalent bonded atoms in a-Se produce localized electronic states in the mobility gap of the density of states function. Furthermore, thermodynamically stable VAP type defects contribute additional localized states. The density and location of these localized states is of considerable interest as they have a profound impact on the optical and transport properties of these materials.

The electronic and optical properties of a-Se are determined by the nature of the amorphous structure of the film, and they may be described in relation to the DOS function. Therefore, a considerable amount of experimental research has been performed in an attempt to generalize the shape of this function. It is currently accepted that the disorder of the film results in an encroachment of localized tail states into the “forbidden” gap of the material, and that thermodynamically stable VAP type defects introduce additional mid-gap states. The localized tail states near the band edge control the carrier mobility through multiple trapping and release events, while the mid-gap states determine the carrier lifetime and, hence, the carrier shubweg. Despite the amount of published data on the properties of this important elemental amorphous semiconductor, several outstanding controversies surrounding the exact shape of the DOS remain to be resolved.

3. TIME-OF-FLIGHT AND INTERRUPTED-FIELD TIME-OF-FLIGHT TRANSIENT PHOTOCONDUCTIVITY: PRINCIPLES AND TECHNIQUES

3.1 Introduction

Amorphous semiconductors are used in many large-area, solid-state devices because they may be economically fabricated as large films with uniform properties. The charge transport properties of these films are of particular interest as they determine, in large part, the performance of such devices. Characterization of these properties relies on direct experimental measurement since theoretical determinations are difficult due to the complexities arising from the disordered state of the material. In fact, the results of such experiments can be used to probe the nature of the electronic transport in these materials. The time-of-flight (TOF) and interrupted-field time-of-flight (IFTOF) transient photoconductivity experiments are powerful techniques for directly measuring the charge mobility and deep trapping time in low mobility solids. These experiments measure the voltage transient that results from the injection and subsequent drift of free charge carriers. This chapter presents the principles of the TOF and IFTOF transient photoconductivity techniques, and the principles and theories involved in the interpretation of the photocurrent signals for various transport and trapping conditions.

3.2 The Time-of-Flight Transient Photoconductivity Technique

The TOF transient photoconductivity technique measures the transient response due to the drift of injected charge carriers across a highly resistive medium. Figure 3.1 (a) illustrates the principles of this technique. A trap free solid of thickness L is

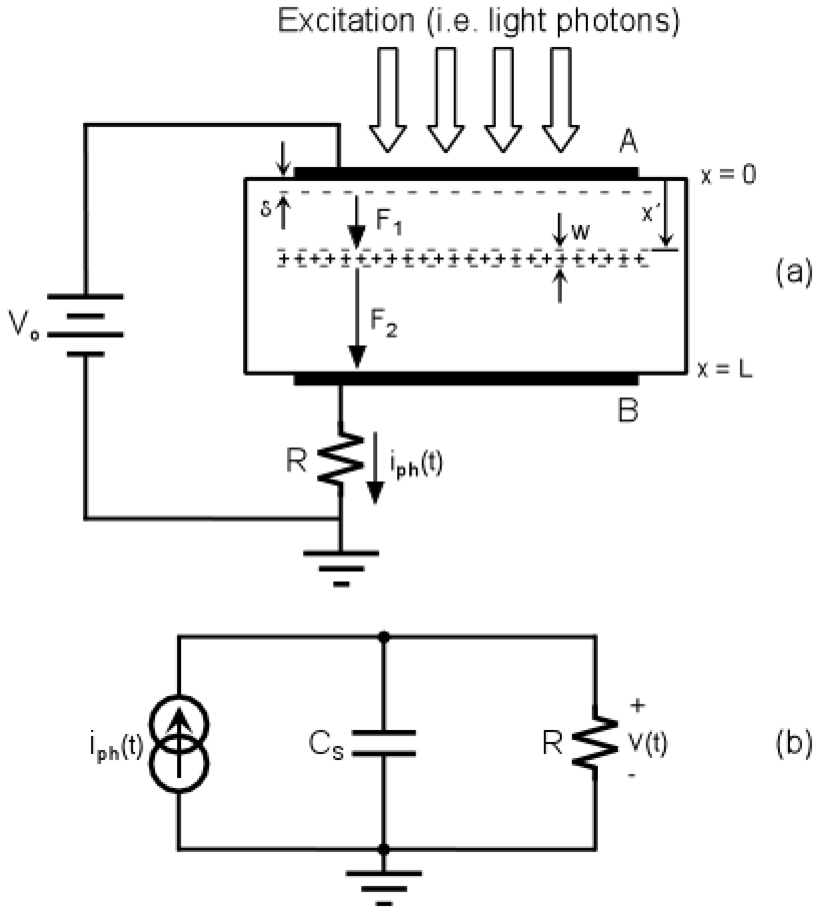

Figure 3.1 The principles of the TOF transient photoconductivity experiment are illustrated in (a) the schematic diagram and (b) the small signal ac equivalent circuit. C_S is the combination of the sample capacitance and any stray capacitance added by the cables and subsequent signal conditioning electronics.

sandwiched between two non-injecting metallic electrodes, A and B. Electrode A is connected to a voltage source, and electrode B is grounded through a resistor. The resistance R is small compared to the resistance of the sample, so the applied field appears almost entirely across the sample thickness.

Electron-hole pairs are generated underneath the top electrode by a short pulse of excitation radiation. An optical excitation pulse may be used provided that the top electrode is transparent or semi-transparent. If the wavelength of the excitation source is selected such that the absorption depth δ of the radiation is small compared to L, then the electrons will be immediately collected at electrode A. The injected holes will drift towards electrode B under the influence of the applied field and will induce a transient photocurrent $i_{ph}(t)$ through the external resistor R. The transient photocurrent due to the drift of electrons can be measured by simply reversing the polarity of the applied bias.

The excitation source used to inject charge into the sample must be carefully selected in order to simplify the analysis of the transient photocurrent response. First, the wavelength of the incident radiation should be selected so that the absorption depth δ is small compared to the thickness of the sample. This ensures that only one carrier species drifts across the entire length of the sample. Care must be taken, however, to ensure that the absorption depth is not too small; carriers that are generated too close to the surface of the material will be trapped by surface defects and will not contribute to the current transient. Second, the duration of the excitation pulse should be much less than the time it takes for the carriers to drift across the thickness of the material. This ensures that the injected carriers drift as a narrow sheet of charge with a width w that is much less than the thickness of the material under investigation. Finally, the intensity of the incident radiation should be small so that the injected carriers do not perturb the internal field; this requirement ensures that experiment is performed under small signal conditions, and it is explained in greater detail below.

The mechanism leading to the photocurrent in the external circuit can be understood by considering the effect of the injected holes on the electric field within the sample. The duration of the excitation pulse is short compared to the time it takes for the injected holes to drift across the length of the sample. Therefore, the injected holes form a "packet" or "sheet" of positive charge of width $w << L$ that drifts towards the bottom electrode with a drift velocity v_d. Consider this charge sheet at a position x' in the solid, as shown in Figure 3.1 (a). In the absence of space charge, the electric fields F_1 and F_2 are constant and depend on the position of the charge sheet in the solid [49], i.e.,

$$F_1 = F_o + \frac{ep_o w}{\varepsilon}\left(\frac{x'}{L} - 1\right) \qquad 3.1,$$

and

$$F_2 = F_o + \frac{ep_o w}{\varepsilon}\frac{x'}{L} \qquad 3.2.$$

In Equations 3.1 and 3.2, p_o is the concentration of holes within the charge sheet, and ε is the dielectric permittivity of the solid. These expressions indicate that the presence of the charge sheet slightly perturbs the applied electric field $F_o = V_o/L$; the electric field F_1 behind the charge sheet is reduced, and the electric field F_2 in front of the charge sheet is enhanced. This deviation in the electric field produces the force responsible for inducing current to flow in the external circuit.

If the TOF photocurrent is to be used to determine the drift mobility of the charge packet, then it is important that the perturbation term in Equations 3.1 and 3.2 is negligible compared to the applied field, i.e. $ep_o w/\varepsilon << V_o/L$. This condition is realized when the total injected charge Q_o is much less than the charge on the electrodes as determined by $C_S V_o$, where C_S is the capacitance of the sample. This is referred to as the *small-signal condition* and means that, as a first approximation, the field in the solid can be considered uniform, and that the charge packet moves at a constant drift velocity [50]. If the hole packet perturbation is comparable to the applied field, then the analysis becomes considerably more complex and must include the effects of the space charge perturbation [51].

The photocurrent signal produced in the external circuit due to the drift of the charge sheet can be determined using Ramo's theorem [52]. Consider a positive charge q generated at a position l in a highly resistive medium with an applied field $F_o = V_o/L$, as shown in Figure 3.2. The charge drifts towards the left with a constant drift velocity $v_d = \mu F_o$, where μ is the mobility of the charge in the medium. The transit time t_T is defined as the time it takes for the charge to drift from its generation point to the collecting electrode, i.e., $t_T = l/v_d$. The motion of the charge in the solid induces a current in the external circuit of Figure 3.2 that persists for the duration of the transit time. When it reaches the electrode, the charge is collected by battery, and the photocurrent goes to zero.

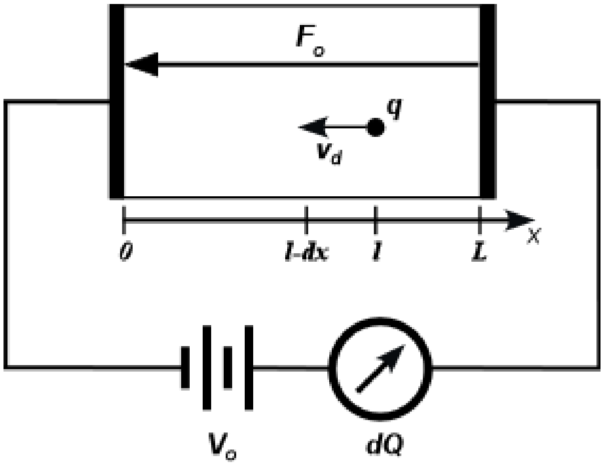

Figure 3.2 The motion of a charge *q* through a distance *dx* in the sample induces a charge *dQ* to flow in the external circuit.

The magnitude of the current induced in the external circuit may be determined by the following arguments. First, consider that the force acting on the charge is qF_o; it follows that the amount of work required to move the charge a distance *dx* is $qF_o dx$. The battery in the external circuit must provide this work; therefore, the work done *dW* in moving the charge a distance *dx* in time *dt* is $dW = F_o q dx = V_o i_{ph}(t) dt$. Using $F_o = V_o / L$ and $v_d = dx/dt$, it can be shown that the magnitude of the current in the external circuit due to the drifting charge is

$$i_{ph}(t) = \begin{cases} \dfrac{q v_d(t)}{L} & 0 < t < t_T \\ 0 & t > t_T \end{cases} \qquad 3.3.$$

Equation 3.3 can be applied to the situation depicted in Figure 3.1 provided that the small signal condition is met in the TOF experiment. The total number of injected holes in the TOF experiment is

$$Q_o = e p_o w A \qquad 3.4,$$

where p_o is the injected hole concentration, *w* is the width of the charge sheet (i.e., the absorption depth of the excitation radiation), and *A* is the area of the charge sheet (i.e. the exposure area). The injected charge sheet is narrow compared to the length of the sample, so the packet essentially drifts across the entire thickness of the solid, L. The drift velocity $v_d = \mu V_o / L$ is constant under small signal conditions, so the transit time of the charge sheet is

$$t_T = \frac{L}{v_d} = \frac{L^2}{\mu V_o} \qquad 3.5,$$

where μ is the conduction mobility of the injected holes in the solid. The photocurrent in the external circuit due to the motion of the injected charge sheet is therefore

$$i_{ph}(t) = \begin{cases} \dfrac{e p_o w A v_d}{L} = \dfrac{e p_o w A}{t_T} & 0 < t < t_T \\ 0 & t > t_T \end{cases} \qquad 3.6.$$

The transient voltage response generated by this photocurrent depends on the characteristics of the external circuit in Figure 3.1 (a). The small signal ac equivalent of the TOF setup is shown in Figure 3.1 (b). Here, C_S is the combination of the capacitance of the sample and the parasitic capacitance added by the cables and subsequent signal conditioning electronics. The photocurrent produces a voltage signal that appears across the impedance determined by the parallel combination of R and C_S. If $V(s)$ and $I_{ph}(s)$ are the Laplace transforms of the voltage signal and photocurrent signal respectively, then it can be shown that

$$V(s) = \frac{R}{sRC_S + 1} I_{ph}(s) \qquad 3.7.$$

An expression for the transient voltage response $v(t)$ is found by taking the inverse Laplace transform of the above equation. If the bandwidth of the photocurrent signal is arbitrarily defined as the reciprocal of the transit time, then it can be shown that there are two solutions depending on the relative magnitude of R and C_S. If $RC_S << t_T$, then taking the inverse Laplace transform of Equation 3.7 yields

$$v(t) \approx \begin{cases} Ri_{ph}(t) & 0 < t < t_T \\ 0 & t > t_T \end{cases} \qquad \text{for } RC_S << t_T \qquad 3.8.$$

Equation 3.8 is called the I-mode signal because the magnitude of the observed signal is directly proportional to the photocurrent signal. An ideal I-mode signal rises abruptly upon charge carrier generation, and remains constant until the charge carriers reach the collecting electrode, at which point the signal falls back to zero. It lends itself readily to the evaluation of the charge carrier drift mobility since an abrupt change in the signal magnitude occurs when the carriers leave the specimen.

If $RC_S >> t_T$, then the inverse Laplace transform of Equation 3.7 becomes

$$v(t) \approx \begin{cases} \dfrac{1}{C_S} \dfrac{ep_o wA}{t_T} t & 0 < t < t_T \\ \dfrac{1}{C_S} ep_o wA & t > t_T \end{cases} \qquad 3.9,$$

which can be further simplified and expressed as

$$v(t) \approx \frac{1}{C_S} \int_0^t i_{ph}(t')dt' \qquad \text{for } RC_S >> t_T \qquad 3.10.$$

Equation 3.10 is the integral of the expression for the I-mode signal, and it is known as the V-mode signal. This signal increases linearly with time as the charge sheet traverses the thickness of the solid. After the carriers reach the collecting electrode the voltage signal remains constant at a value that is proportional to the total injected charge. The V-mode signal is often referred to as the *charge transient signal*, and it is typically used to measure the total quantity of charge that is injected into the solid.

In the preceding discussion, the time dependence of the number of mobile charge carriers in the charge sheet has been tacitly ignored by assuming that the solid in question is free of charge carrier traps. This assumption is generally invalid for amorphous semiconductors; the disordered nature of these materials introduces a large number of localized states within the mobility gap of the semiconductor. The number of mobile charge carriers in the charge sheet decreases as the sheet drifts across the solid because charge carriers are trapped in these localized states and removed from the transport band. The magnitude of the photocurrent, which is proportional to the number of charges in the packet, will therefore decay with time due to the trapping of free carriers.

Consider a set of hole traps located at a discrete energy level deep in the mobility gap of the semiconductor and characterized by a mean trapping time τ_c. It is assumed that the release time from these traps is much longer than the transit time of the charge sheet, i.e. trapped carriers are not released back into the transport band in the time scale of the experiment. It can be shown that the number of free carriers contributing to the photocurrent will decay exponentially as the charge sheet traverses the sample. Equation 3.6 can be modified to take this decay into account, i.e.,

$$i_{ph}(t) = \frac{ep_o wA \exp(-t/\tau_c)}{t_T} \qquad 3.11.$$

The I-mode signal can be found by substituting Equation 3.11 into Equation 3.8 to get

$$v(t) = \begin{cases} R\dfrac{ep_o wA}{t_T}\exp\left(-\dfrac{t}{\tau_c}\right) & 0 < t < t_T \\ 0 & t > t_T \end{cases} \qquad 3.12.$$

The expression for the V-mode transient signal is determined by integrating Equation 3.12;

$$v(t) = \begin{cases} \dfrac{ep_o wA\,\tau_c}{C_S t_T}\left(1 - \exp\left(-\dfrac{t}{\tau_c}\right)\right) & 0 < t < t_T \\ \dfrac{ep_o wA\,\tau_c}{C_S t_T}\left(1 - \exp\left(-\dfrac{t_T}{\tau_c}\right)\right) & t > t_T \end{cases} \qquad 3.13.$$

This final expression, known as the Hecht relationship, was used extensively to estimate the trapping time of charge carriers from TOF photocurrent signals [53]. Figure 3.3 illustrates the expected I- and V-mode transient signals for the case of a trap free solid ($\tau_c = 100t_T$) and for the case of heavy deep trapping ($\tau_c = t_T$).

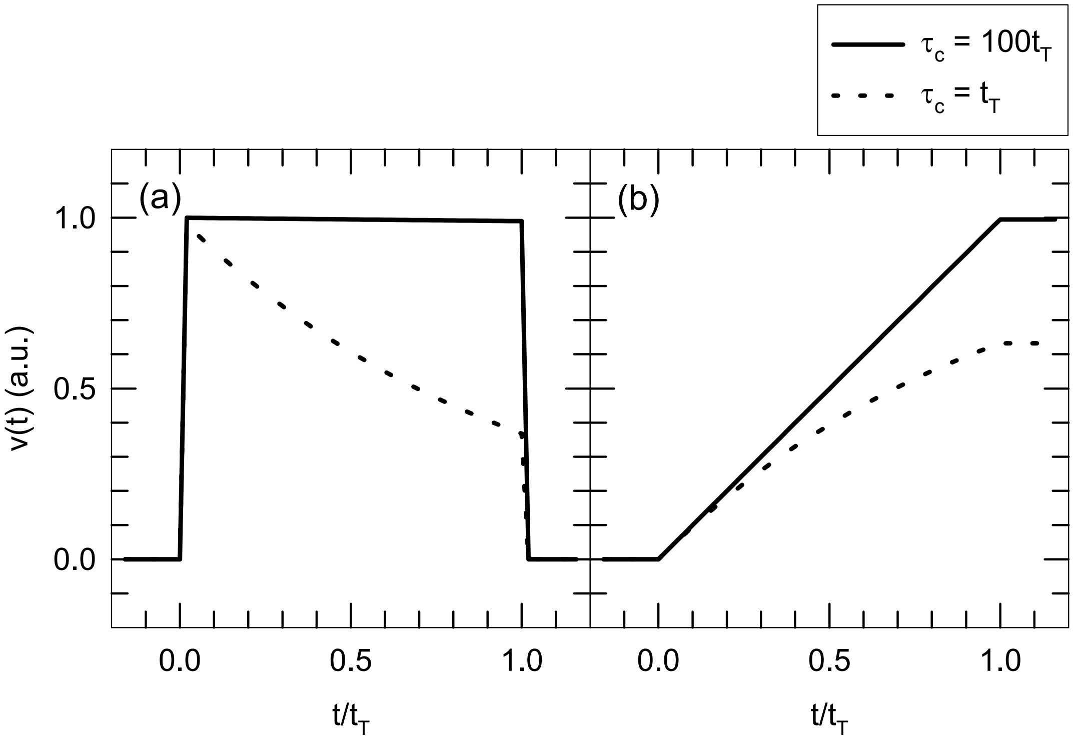

Figure 3.3 Simulation of the expected (a) I-mode and (b) V-mode TOF photocurrent transient signals for the case of no traps (solid line) and deep traps (dashed line).

3.3 The Interrupted-Field Time-of-Flight Technique

The interrupted-field time-of-flight (IFTOF) transient photoconductivity technique is a powerful technique for accurately measuring the deep trapping lifetime of carriers in high resistivity materials such as amorphous selenium. The principle of this technique is similar to the conventional TOF technique described in Section 3.2. A short laser pulse injects a narrow sheet of free carries into a sample with a thickness *L* and an applied bias *V*. The charge sheet drifts across the solid and induces a transient photocurrent signal to flow through the external resistor *R*. If small signal conditions are maintained during the experiment, then the charge packet velocity $v_d = \mu V/L$ is constant because the field is uniform and the mobility μ is a material property. If the solid in question has a discrete distribution of traps located deep in the mobility gap, then the magnitude of the induced photocurrent may be determined from Equation 3.11. If the bias is selected such that the transit time t_T is much larger then the capture time τ_c of these traps, the magnitude of the photocurrent may be expressed as

$$i = e\mu PV/L \qquad 3.14,$$

where P is the number of carriers in the charge sheet. Equation 3.14 shows that, under the proper experimental conditions, the photocurrent is directly proportional to the number of carriers in the charge sheet.

The IFTOF technique measures the trapping time of the drifting carriers by temporarily removing the applied field at some time t_1 before the carriers reach the collecting electrode, i.e. $0 < t_1 < t_T$. As soon as the field is removed, the drift of the charge sheet is halted, and the photocurrent in the external circuit falls to zero. The carriers remain at a position $\ell \approx t_1 L/t_T$ under zero field conditions until the field is reapplied at time t_2. The charge carriers resume their transit across the sample thickness, and a post interruption photocurrent is induced in the external circuit that persists until the carriers are collected at the electrode. During the interruption time $t_i = t_2 - t_1$, some of the carriers in the charge sheet will be removed from the transport band by the localized gap states at position ℓ. If these states are characterized with a well defined τ_c, then the charge carrier concentration following the field interruption $p(t_2)$ is related to the charge carrier concentration before the field interruption $p(t_1)$ by $p(t_2)/p(t_1) = \exp(-t_i/\tau_c)$. Since the induced photocurrent signal is proportional to the concentration of carriers in the packet, it follows that the magnitude of the photocurrent following the interruption $i(t_2)$ is related to the photocurrent before the interruption $i(t_1)$ by

$$\frac{i(t_2)}{i(t_1)} = \exp\left(-\frac{t_i}{\tau_c}\right) \qquad 3.15.$$

Equation 3.15 shows that the amount of trapping that occurs during t_i will be reflected in the relative magnitudes of the IFTOF photocurrent signals before and after the interruption. This is illustrated in Figure 3.4 for an ideal solid with a well defined capture time that is much larger than the transit time. The conventional TOF transient

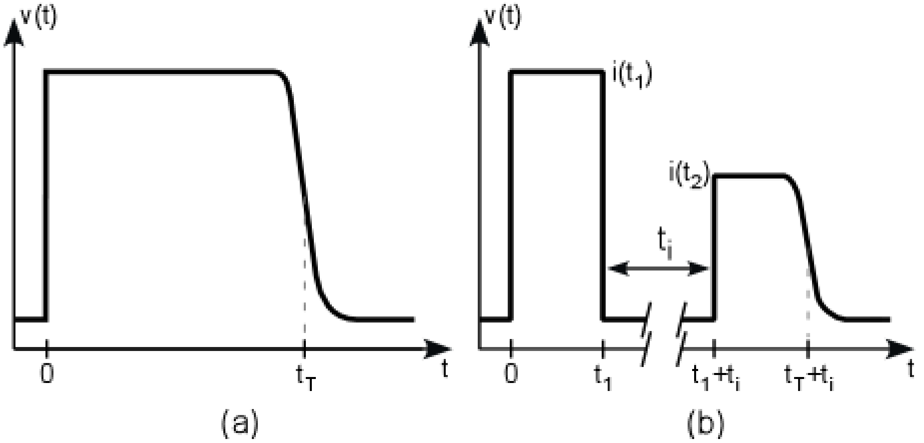

Figure 3.4 (a) A typical TOF waveform and (b) a typical IFTOF waveform. During the interruption time t_i, carriers are lost to deep traps so that the magnitude of the photocurrent immediately after interruption i_2 is less than the photocurrent immediately before the interruption i_1.

response is also shown for comparison. A typical IFTOF experiment involves measuring the fractional recovered photocurrent as a function of the interruption time at a single position in the sample. The carrier lifetime is then determined from the slope of a semi-logarithmic plot of $i(t_2)/i(t_1)$ versus t_i.

3.4 Transient Trap Limited Theory

The previous two sections introduced the principles of the TOF and IFTOF experiments. The expressions for the I- and V-mode transient responses due to the injection and subsequent drift of a sheet of charge carriers in a high resistivity solid were also developed. These expressions, however, do not reflect the transient response that is observed in specimens of amorphous semiconductors. Such materials are characterized by a large concentration of localized states within the mobility gap. These localized states act as capture centers (traps) for free carriers in the transport band, and, therefore, will have a significant influence on the charge carrier kinetics in these materials. Understanding the influence of these localized states on drifting carriers is key to understanding the transport properties of these solids. A transient trap limited theory is developed in this section to explain the transient response that is observed in amorphous semiconductors for three separate cases: a discrete monoenergetic trap distribution, a discrete binary trap distribution, and a continuous extended trap distribution.

3.4.1 Monoenergetic Trap Level

Consider a set of localized states distributed at a single, well-defined energy in the mobility gap of the solid. These localized states trap drifting carriers so that they are temporarily removed from the transport band. In order to develop an expression for the transient response due to the drift of free carriers in the presence of these traps, an expression for the time dependence of the charge density in the packet must first be developed. Consider the flow of excess hole carriers in a semiconductor solid as illustrated in Figure 3.5. The number of free holes in an infinitesimal slice of thickness *dx* changes due to the current flowing through the slice and due to the thermal release of holes from traps in the slice. The rate of change in the number of free holes in the slice can, therefore, be expressed as

$$\frac{\partial p(x,t)}{\partial t} = -\frac{1}{e}\frac{\partial J(x,t)}{\partial x} - \frac{\partial p_t(x,t)}{\partial t} \qquad 3.16,$$

where $p(x,t)$ is the instantaneous free hole density, $J(x,t)$ is the current density, and $p_t(x,t)$ is the density of the holes occupying the traps in the slice.

The total current density $J(x,t)$ flowing into the slice is composed of the

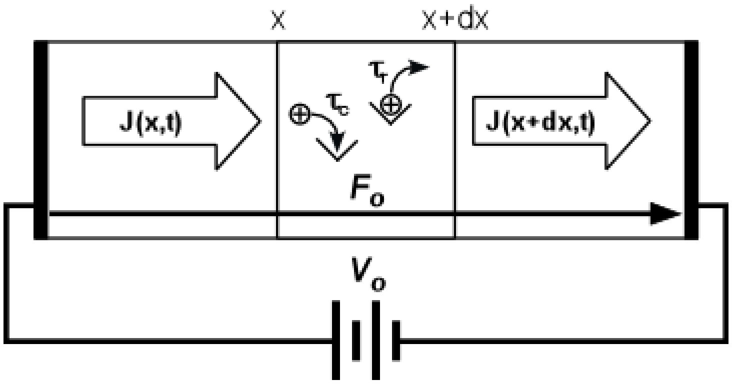

Figure 3.5 The number of holes within a semiconductor slice of thickness *dx* increases due to the flow of holes into the slice and due to the release of trapped holes within the slice.

conduction current and the diffusion current. The conduction current is due to the drift of the holes under the influence of the electric field, i.e.

$$J_C(x,t) = e\mu_O p(x,t)F(x,t) \qquad 3.17,$$

where μ_o is the conduction mobility, and $F(x,t)$ is the applied field. The diffusion current is due to the spatial variation in the concentration of charge carriers and is given by

$$J_D(x,t) = -eD\frac{\partial p(x,t)}{\partial x} \qquad 3.18,$$

where D is the diffusion coefficient.

The total current density can be expressed as the sum of the conduction current density and the diffusion current density, so Equation 3.16 can be expressed as

$$\frac{\partial p(x,t)}{\partial t} = -\mu_0 F(x,t)\frac{\partial p(x,t)}{\partial x} - \mu_0 p(x,t)\frac{\partial F(x,t)}{\partial x} + D\frac{\partial^2 p(x,t)}{\partial x^2} - \frac{\partial p_t(x,t)}{\partial t} \qquad 3.19.$$

Equation 3.19 is known as the one-dimensional continuity equation for holes. The one-dimensional continuity equation for electrons can be similarly derived, and it is expressed as

$$\frac{\partial n(x,t)}{\partial t} = \mu_o F(x,t)\frac{\partial n(x,t)}{\partial x} + \mu_o n(x,t)\frac{\partial F(x,t)}{\partial x} + D\frac{\partial^2 n(x,t)}{\partial x^2} - \frac{\partial n_t(x,t)}{\partial t} \qquad 3.20,$$

where $n(x,t)$ is the instantaneous electron density, and $n_t(x,t)$ is the density of electrons occupying deep traps.

The rates of change in the number of trapped holes and trapped electrons, $\partial p_t(x,t)/\partial t$ and $\partial n_t(x,t)/\partial t$ respectively, are known as rate equations and they represent the difference in the instantaneous trapping and release rates of the carriers. If τ_c and τ_r are the capture time and release time respectively, then the rate equations for holes and electrons are expressed as

$$\frac{\partial p_t(x,t)}{\partial t} = \frac{p(x,t)}{\tau_c} - \frac{p_t(x,t)}{\tau_r} \qquad 3.22,$$

and

$$\frac{\partial n_t(x,t)}{\partial t} = \frac{n(x,t)}{\tau_c} - \frac{n_t(x,t)}{\tau_r} \qquad 3.21,$$

respectively.

An expression for the time dependence of the carrier density in the charge packet can be derived by simultaneously solving the rate equation and the continuity equation of the carrier species in question. If small signal conditions are met in the TOF experiment, then the electric field *F(x,t)* is uniform with respect to time and position in the sample, i.e. $\partial F(x,t)/\partial t = 0$. Also, the diffusion portion of the current density flowing through the slice can be neglected since the diffusion of the charge carriers in the packet is assumed to be negligible.

The following derivation is considered only for hole transport, however, a similar discussion can also be developed for electron transport. The boundary conditions required to solve Equations 3.19 and 3.22 may be defined by considering the TOF experiment developed in the previous section. At time t = 0, a short excitation pulse generates carriers at a position x = 0. If the absorption depth of the radiation is small compared to the length of the sample, then the distribution of generated holes $p(x,0)$ may be approximated by a delta function $\delta(x)$, i.e.

$$p(x,0) = P_o \delta(x,0) \qquad 3.23,$$

where P_o is the number of generated holes. As the holes have yet to traverse the sample, it follows that the hole traps are initially unoccupied, i.e.,

$$p_t(x,0) = 0 \qquad \text{for } x > 0 \qquad 3.24.$$

Once the injected hole packet drifts across the length of the sample, it is collected by the electrode, so that

$$p(x,t) = 0 \qquad \text{for } x > L \qquad 3.25.$$

It follows also that there are no traps located outside of the sample, so that

$$p_t(x,t) = 0 \qquad \text{for } x > L \qquad 3.26.$$

A solution to Equations 3.19 and 3.22 can be found using the above boundary conditions and Laplace transform techniques as outlined in References [54, 55]. The resulting expression for the free hole density as the hole packet traverses the solid is

$$p(x,t) = \frac{P_0}{\mu_0 F}\exp(-\frac{z}{\tau_c})\delta(t-z) + \frac{P_0}{\mu_0 F}\exp\left[-\frac{z}{\tau_c} - \frac{(t-z)}{\tau_r}\right]\frac{\xi}{2}\frac{I_1(\xi)}{(t-z)}U(t-z) \qquad 3.27,$$

where $z = x/\mu_0 F$, $I_1(\xi)$ is the first order hyperbolic Bessel function, $U(x)$ is the unit step function, and $\xi = 2\sqrt{\tau_c z(t-z)/\tau_r}/\tau_c$. The first term, which contains the delta function $\delta(x)$, represents the number of charge carriers remaining in the injected hole packet as it drifts across the sample. The number of charge carriers in the delta packet decreases exponentially as $\exp(-t/\tau_c)$. The carriers that remain in the packet are not delayed through trapping events and exit the sample after the transit time $t_T = L/\mu_0 F$, where μ_o is the conduction mobility. The second term containing the Bessel function represents the charge carriers that have been removed from the delta packet and, at time t, are released back into the transport band. These carriers have suffered at least one trapping and release event, and therefore lag behind the delta packet. These charges contribute to the photocurrent for times longer than $t_T = L/\mu_0 F$.

An expression for the time dependence of the total number of free holes in the charge packet can be found by integrating Equation 3.27 over the length of the sample. The resulting expression can be used to obtain an expression for the I-mode transient current response in a medium with a monoenergetic distribution of traps. However, an explicit expression for the time dependence of the number of mobile charge carriers is rather cumbersome to handle. The transient current response can be more easily evaluated for two limiting cases: low field drift and high field drift. In practice, this does not impose a serious restriction on the use of these expressions for predicting the transient response of the charge carriers since these conditions can readily be met by appropriate choice of sample thickness, operating voltage, and temperature. The hole TOF I-mode current response is determined for both low field and high field conditions in the following two sections.

3.4.1.1 Low Fields

In this case, the carrier transit time t_T is much larger than the carrier capture time τ_c and is comparable to the release time τ_r of trapped carriers, i.e. $\tau_c << L/\mu_0 F \approx \tau_r$. Free carriers are removed from the injected charge packet as it traverses the sample by a set of localized traps that are relatively close to the transport band edge. When a trapped carrier is released, it will continue its motion towards the collecting electrode. The carriers will therefore make their way towards the collecting electrode through successive trapping and release events. Since the release time is comparable to the transit time, the time derivative of the free carrier density in Equation 3.19 and 3.20 will vanish over a sufficiently long time interval [56]; i.e., the number of free carriers in the transport band will eventually reach a steady state value. Using the principle of charge conservation and the rate equation for holes, it can be shown that the number of free holes P is related to the total injected charge by

$$P = P_o \frac{\tau_c}{\tau_c + \tau_r} \qquad 3.28,$$

where $P_o = p_o A w$ is the number of injected holes.

The magnitude of the hole photocurrent is obtained by substituting Equation 3.28 into Equation 3.6, i.e.,

$$i_{ph} = \frac{eP_o \mu_o F}{L} \frac{\tau_c}{\tau_c + \tau_r} = \frac{eP_o \mu F}{L} \qquad 3.29.$$

Inspection of Equation 3.29 reveals that it resembles the expression for the trap-free photocurrent signal with the mobility μ_o reduced to μ via

$$\mu = \frac{\tau_c}{\tau_c + \tau_r}\mu_o = \theta\mu_o \qquad 3.30.$$

where $\theta = \tau_c/(\tau_c + \tau_r)$. The corresponding I-mode signal is derived by substituting Equation 3.29 into Equation 3.8. The effective carrier drift mobility is reduced because the carriers are delayed on their drift through the solid by trapping and release events. This transport mechanism is referred to as *shallow trap-controlled transport*, and the scalar θ is referred to as the *shallow trap-controlled transport factor*.

There is one disadvantage of neglecting the time derivative of the number of charge carriers; an analytical expression cannot be obtained to reflect the relative spreading of the charge carrier packet during transit. Charge packet spreading is evident in the characteristic photocurrent tails observed in typical TOF investigations, and is due to the random nature of the trapping and release events. This spreading has been shown to be considerably higher than that due to simple diffusion alone [34].

3.4.1.2 High Fields

In this case, the transit time of the injected carriers is sufficiently short so that a portion of the injected charge traverses the entire length of the solid without becoming trapped, i.e. $L/\mu_o F << \tau_c$. Marini et al. [57] developed expressions for the TOF transient signal in two different time ranges. For $0 < t < L/\mu_o F$, the expression for the photocurrent due to the drift of the charge packet is

$$i_{ph}(t) = \frac{eP_o}{t_T}\left[\frac{\tau_c}{\tau_c + \tau_r} + \frac{\tau_r}{\tau_c + \tau_r}\exp\left(-\frac{\tau_c + \tau_r}{\tau_c \tau_r}t\right)\right] \qquad 0 < t < \frac{L}{\mu_o F} \qquad 3.31,$$

where P_o is the number of injected holes. Note that if the release of carriers is neglected by letting $\tau_r \to \infty$, then Equation 3.31 reduces to Equation 3.11, the expression for the photocurrent derived for the case of deep trapping.

The photocurrent for times $t > L/\mu_o F$ is due to the carriers that have been trapped and subsequently released into the transport band. Once released, the majority of these carriers will leave the sample without being trapped again since the transit time is much shorter than the capture time. It can be shown that the transient response due to the release of trapped carries is [57],

$$i_{ph}(t) = \frac{eP_o}{2}\frac{t_T}{\tau_c \tau_r}\exp\left(-\frac{t}{\tau_r}\right) \qquad t > L/\mu_o F \qquad 3.32.$$

Equations 3.31 and 3.32 indicate that, for the high field case, the transient photocurrent response will decay exponentially as the injected charge packet traverses the sample. At $t = L/\mu_o F$ a step change will occur in the current magnitude, followed by a slow exponential decay to zero as trapped carriers are released back into the transport band and are drifted to the collection electrode.

3.4.2 Binary Trap Distribution

A distribution of localized states at two discrete energy levels is characterized by two capture times, τ_{c1} and τ_{c2}, and two release times, τ_{r1} and τ_{r2}. An expression for the transient photocurrent response in this case is necessarily more complex than for the case of a monoenergetic distribution of traps with single capture and release times. In order to simplify the analysis, it is assumed that the concentration of injected charge carriers is much less than the concentration of traps at each energy level so that the effect of trap filling can be neglected. It is also assumed that the number of carriers at a trap level may only increase due to trapping of carriers from the transport band and not from the release of carriers from a deeper level of traps. The hole rate equations for the binary trap system can be expressed as

$$\frac{\partial p_{t1}(x,t)}{\partial t} = \frac{p(x,t)}{\tau_{c1}} - \frac{p_{t1}(x,t)}{\tau_{r1}} \qquad 3.33,$$

and

$$\frac{\partial p_{t2}(x,t)}{\partial t} = \frac{p(x,t)}{\tau_{c2}} - \frac{p_{t2}(x,t)}{\tau_{r2}} \qquad 3.34.$$

The time evolution of the number of holes in the injected charge packet can be derived by simultaneously solving Equations 3.33, 3.34 and 3.19; note that the total trapped charge concentration is the sum of the charge concentration at each trap level, i.e. $p_t(x,t) = p_{t1}(x,t) + p_{t2}(x,t)$. Essentially, a binary trap distribution can be represented as a superposition of two mono-energetic trap distributions. Blakney and Grunwald [58] developed the following expression for the transient photocurrent in the presence of a binary trap distribution:

$$j(t) = A\exp(-\alpha t) + B\exp(-\beta t) + j_\infty \qquad 3.35,$$

where

$$\alpha + \beta = \frac{1+\theta_1}{\tau_{c1}} + \frac{1+\theta_2}{\tau_{c2}} \qquad 3.36,$$

$$\alpha\beta = \frac{[\theta_1 + \theta_2(1+\theta_1)]}{\tau_{c1}\tau_{c2}} \qquad 3.37,$$

$$\alpha A + \beta B = \frac{j_o}{\tau_{c1}} + \frac{j_o}{\tau_{c2}} \qquad 3.38,$$

$$A + B + j_\infty = j_o \qquad 3.39,$$

and

$$j_\infty = \frac{j_o\theta_1\theta_2}{[\theta_1 + \theta_2(1+\theta_1)]} \qquad 3.40,$$

where $\theta_1 = \tau_{c1}/\tau_{r1}$ and $\theta_2 = \tau_{c2}/\tau_{r2}$. The term j_∞ represents the steady state current that flows after the injected charges have come into equilibrium with the traps.

A noteworthy situation occurs when one species of traps is located deep such that the thermal release of captured carriers is long compared to the transit time, i.e. $\tau_{r2} \to \infty$. In this case $\theta_2 = 0$, and it can be shown that Equation 3.35 reduces to

$$j(t) = A\exp\left(-\frac{t}{\tau_{c1}}\right) + B\exp\left(-\frac{\theta_1 t}{\tau_{c2}}\right) \qquad 3.41.$$

The transport mechanism in this case is referred to as *shallow trap-controlled with deep trapping*, and it is commonly used to describe electron transport in amorphous selenium [59, 60]. The first term in Equation 3.41 represents an initial exponential decaying spike that occurs while the injected carriers equilibrate with the shallower set of traps. This is followed by a slower decaying exponential curve with a characteristic decay rate given by τ_{c2}/θ_1.

3.4.3 Extended Trap Distribution

An analytic derivation for the transient trap limited response for the case of an extended distribution of trap energy levels is necessarily more complex. One approach, proposed by Schmidlin [61], is to divide the continuum of traps into a finite number of isoenergetic levels. The solution for the time evolution of the charge density can be derived from arguments similar to those presented in the previous section; however, a detailed review of the solution is not presented here as it is beyond the scope of the current investigation. A description of the results may be found in Noolandi [62], Schmidlin [63], and Rudenko [64]. It can be shown that, for a sufficiently narrow distribution of traps that forces the charge carriers to become trapped and released several times during transit, the dispersion of holes in the drifting packet can be approximated by a Gaussian function. The photocurrent response under this condition exhibits a tail that follows the approximate normal probability function with a variance given by

$$\Delta t = \frac{2\tau_r^2 L}{\tau_c \mu_o F} \qquad 3.42.$$

This spread is greater than that expected from carrier dispersion alone, and it is observed in a number of materials such as a-Se:As$_{0.2\%}$ [65].

3.5 Summary

In this chapter, the principles of the time-of-flight and interrupted-field time-of-flight transient photoconductivity measurements were introduced. Essentially, these techniques measure the transient response due to the drift of carriers across a highly resistive medium. The former technique lends itself readily to the determination of the carrier mobility, while the later may be used to accurately evaluate the carrier lifetime at different positions in the sample. Accurate measurements of the carriers' mobilities and lifetimes are important for studying amorphous semiconductors used in photoreceptor applications, as the mobility-lifetime product determines the photoreceptor performance.

This chapter also developed expressions for the transient signals for various trap distributions commonly encountered in amorphous semiconductors. For an energetically shallow set of traps, trapping and release events prolong the carrier transit time because of the finite dwell time for the carriers occupying the traps. Traps located deeper in the mobility gap cause the photocurrent signal to decay exponentially with a characteristic decay rate that corresponds to the trapping time τ_c. It is apparent from the discussions in this chapter that the TOF technique may be used to probe the distribution of gap states in amorphous semiconductors. The TOF and IFTOF experiments described in this chapter are therefore very important because they may be used to study the fundamental charge transport processes in amorphous semiconductors.

4. EXPERIMENTAL PROCEDURE

4.1 Introduction

The experimental procedures that were used to study the transport properties in stabilized amorphous selenium (a-Se) photoconductive layers are described in this chapter. In Section 4.2, the process of fabricating x-ray photoconductor layers from selenium and the preparation of the samples for transient photoconductivity measurements is described. In Section 4.3, the experimental setup required to perform the TOF and IFTOF techniques is described, the procedures for measuring the carrier drift mobilities and lifetimes are outlined, and the experimental difficulties associated with transient photoconductivity measurements are explained. In Section 4.4, a detailed description of the TOF/IFTOF measurement system that was built for this investigation is presented. In Section 4.5, the x-ray system that was used to irradiate the a-Se photoconductor layers in order to investigate the effects of x-ray exposure on the samples is described; the procedures to safely operate the x-ray system and to prolong the useful lifetime of the x-ray tube are also explained.

4.2 Sample Preparation

The samples of a-Se were prepared using conventional vacuum deposition techniques; vitreous selenium pellets heated in a stainless steel boat produce a selenium vapor, which condenses onto an aluminum substrate to form an a-Se layer. Pure a-Se layers are not thermally stable and tend to crystallize with time. The rate of crystallization is reduced significantly by alloying pure selenium with a small amount of As (~0.2%). Typically, a small amount (~10ppm) of a halogen such as Cl is also added to compensate for the decrease in the hole lifetime that occurs with the addition of As. The resulting thermally stable alloy is called *stabilized a-Se* and is denoted, for example as a-Se:$As_{0.5\%}$ + 10ppm Cl; henceforth, stabilized a-Se will simply be referred to as a-Se. For the purpose of this investigation, various samples were prepared with different amounts of As (0.2-0.7%) and Cl (0-40 ppm) to examine the effects of alloy composition on the transport properties. The source material used to fabricate the samples was obtained from Anrad Corporation of Montreal, QC.

Oxidized Al substrates were used to form the bottom electrode and to provide a surface for the deposition of the a-Se layer. A general requirement for TOF transient photoconductivity measurements is that the contacts be blocking in order to prevent charge injection into the sample. This ensures that, when a bias is applied to the sample, the dc conduction level will be smaller than the magnitude of the photocurrent signal. The oxide layer on the surface of the substrate provides a sufficient barrier between the substrate and the a-Se film to prevent charge injection [66]. It also provides an amorphous base onto which the film may be grown.

The Al substrates were rigorously cleaned prior to insertion in the vacuum deposition system. In the first step of the cleaning process, the protective polymer coating on the aluminum surface was removed using ultrasonic baths in a sequence of acetone, distilled water, methanol, and distilled water. Next, the existing oxide layer was partially removed by placing the substrates into a heated (65°C) etch solution of sodium carbonate, sodium phosphate and distilled water. The substrates were then dipped into a nitric acid solution and washed with repeated cycles of distilled water and detergent solutions. Finally, the substrates were placed in a furnace at 300°C for 4-5 hours to replenish the oxide layer.

The a-Se layers were evaporated onto the Al substrates using the NRC 3117 stainless steel vacuum coater system illustrated in Figure 4.1. The substrate and source material were loaded into the system and the chamber was evacuated to a base pressure of ~ 10^{-6} Torr. The molybdenum boat containing the source material was heated to ~ 250

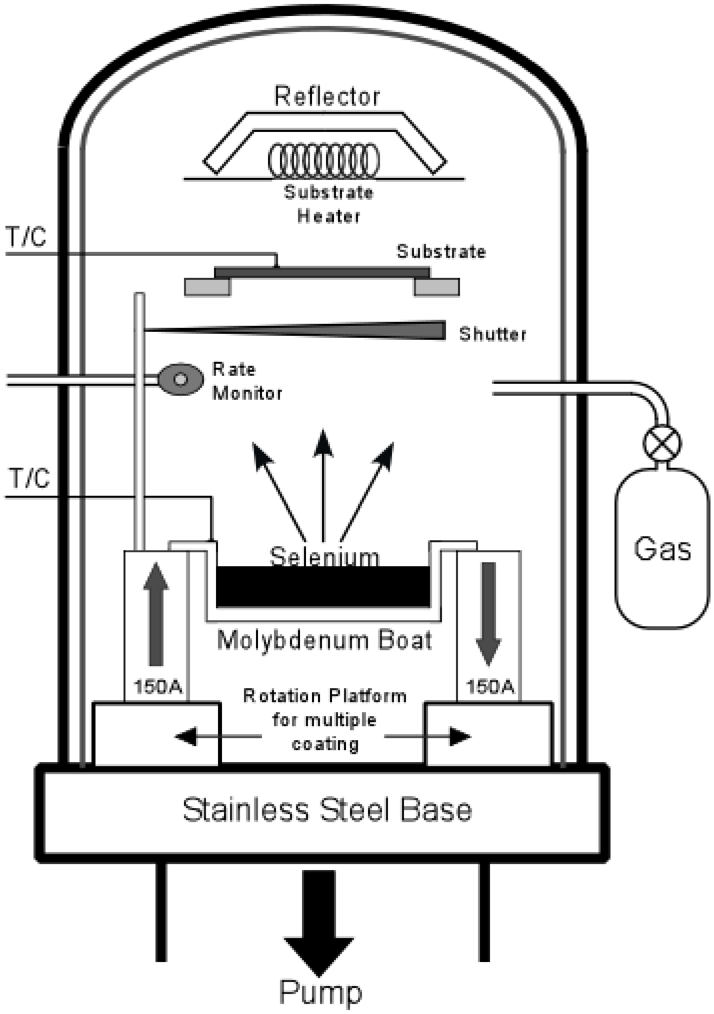

Figure 4.1 Schematic diagram of the NRC 3117 vacuum deposition system that was used to fabricate the films in this study.

°C by the application of a large (100-150A) ac current. The properties of the film depend on the deposition conditions; therefore, two thermocouples (T/C) were used to carefully monitor the temperature of the boat and substrate, and a digital quartz crystal rate monitor was used to monitor the evaporation rate of the selenium. A mechanical shutter prevented the selenium vapor from condensing on the substrate until a steady evaporation rate of ~ 2 μm/min was reached.

During the deposition of the film, the temperature of the substrate was carefully maintained at a constant value above the glass transition temperature for a-Se (typically 60°C). In order to produce a homogeneous sample, the deposition was stopped before the source material in the boat was completely evaporated by closing the shutter. For each deposition, approximately 40-50 g of material was used in order to produce films that were approximately 100 μm thick. The substrate and boat heaters were then shut off to allow the system to cool while the chamber was pressurized. The sample was then removed from the system, and the thickness of the evaporated layer was measured using a digital micrometer. The sample was then placed in a dark location at room temperature for 2-3 days to allow its physical properties to stabilize.

The final step in the preparation of samples for transient photoconductivity measurements was to sputter semitransparent and conducting gold electrodes onto the surface of the film using a Hummer VI sputtering system, shown in Figure 4.2. Low injecting, but non-ohmic metallic electrodes applied directly to the surface of the sample were used to reduce the amount of charge injection during the TOF experiment. To deposit the electrodes, the amorphous selenium sample was covered with an aluminum mask exposing a circular contact area of 0.5 cm^2 and placed in the vacuum chamber of the Hummer VI sputtering system. The chamber was pumped down to a pressure of 100 mTorr and then flooded with argon gas. A high voltage applied between the anode and cathode ionizes the argon gas molecules in the chamber. The positively charged ions then collide with the negatively charged gold target, dislodging gold particles that

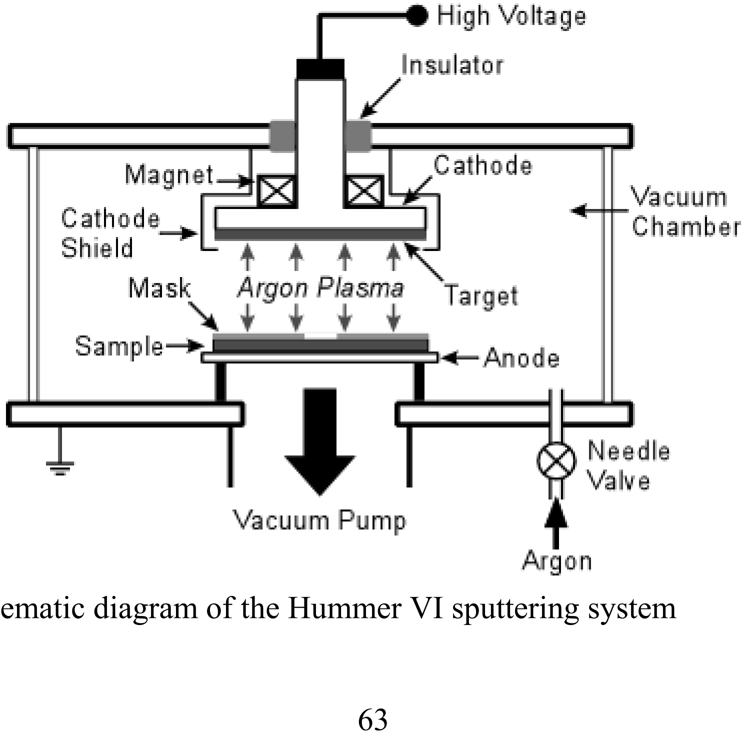

Figure 4.2 Schematic diagram of the Hummer VI sputtering system

uniformly coat the unmasked region of the sample.

Once the top electrode was deposited onto the surface of the film, the sample could be loaded into the TOF/IFTOF system sample holder in preparation for the transient photoconductivity measurements. The electrical connections to the top electrode and the substrate were made using stainless steel pressure contacts. Small indium disks were used to improve the electrical connection and to prevent the pressure contact from damaging the thin Au electrode. Figure 4.3 shows a sample loaded into the sample holder, ready for TOF and IFTOF measurements.

4.3 Charge Transport Measurements

The charge transport properties of a-Se photoconductor layers were investigated using conventional Time-of-Flight (TOF) and Interrupted-Field-Time-of-Flight (IFTOF) transient photoconductivity measurements. These experiments measure the transient response resulting from the drift of charge carriers across the high field region of a semiconductor or insulator as discussed in Chapter 3. Figure 4.4 depicts a system capable of I-mode transient photoconductivity measurements and illustrates the principles of the experimental setup. A switchable, high voltage power supply is triggered by the

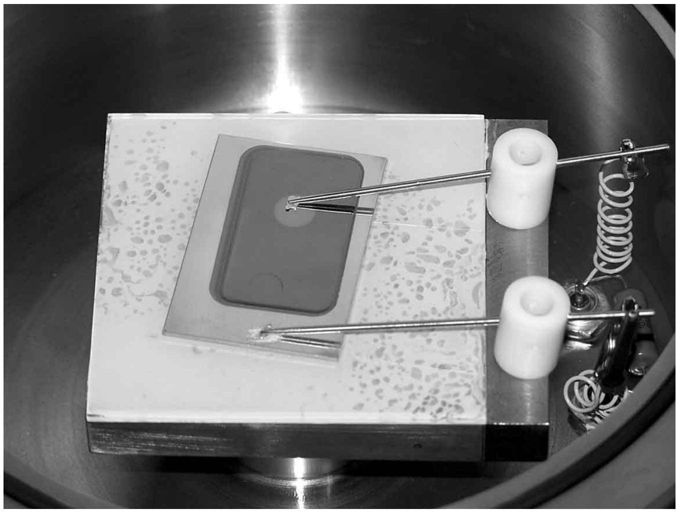

Figure 4.3 The sample loaded in the sample holder ready for TOF and IFTOF transient photoconductivity measurements.

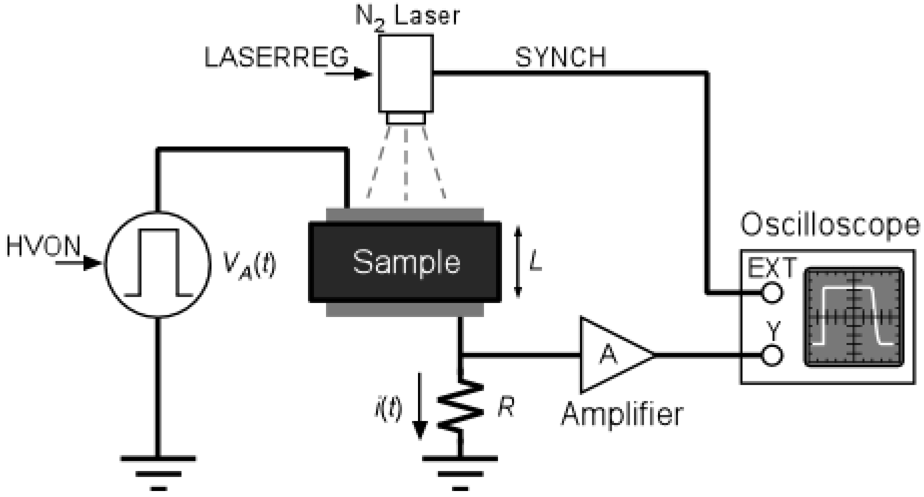

Figure 4.4 A schematic diagram of the transient photoconductivity experimental setup for measuring the charge transport properties of a-Se. HVON modulates the bias voltage for the TOF and IFTOF measurements and LASERREG triggers the short photo-excitation pulse. The oscilloscope trigger is synchronized with LASERREG in order to capture and record the generated signal.

signal HVON to apply a voltage bias V to the sample. After a short settling period to allow the high voltage switching transients to settle, a short duration pulse of strongly absorbed light injects a narrow sheet of charge carriers into the sample. The drift of the charge sheet across the sample induces a transient photocurrent $i(t)$ through the sampling resistor R. The resistor converts the current signal into a voltage signal $v(t) = Ri(t)$, which is then amplified and recorded by the oscilloscope; the oscilloscope trigger is synchronized with the laser trigger in order to capture the entire transient response.

Note that the captured signal is directly proportional the value of the sampling resistor; the magnitude of the signal can, therefore, be maximized by increasing R at the expense of an increase in the RC time constant of the circuit, where C is a combination of the sample capacitance and the stray capacitances introduced by the cables and signal conditioning electronics. If RC is too large, the bandwidth of the sampling circuit will be limited, and the captured signal will be distorted. For proper I-mode TOF detection, R should be selected such that $RC \ll t_T$, where t_T is the minimum expected TOF pulse width.

The TOF technique provides a direct means to evaluate the drift mobilities of either holes or electrons in a wide range of materials including liquids, amorphous semiconductors, and semiconductors exhibiting negative differential mobilities. The technique was first pioneered in the fifties and sixties by Spear [33], Kepler [67], Leblanc [68], and Brown [69], and several variations of the experimental system have appeared in the literature including different photoexcitation sources, pulsed or dc bias schemes, and delayed or advanced photoexcitation techniques for studying bulk space charge buildup effects [70] and charge carrier recombination [71] respectively. The most common method used for charge carrier injection is a short duration pulse of strongly absorbed light. The spectral output of the photoexcitation source must be closely matched to the band gap of the material under investigation in order to prevent bulk photogeneration. Some of the optical sources used in the literature for drift mobility measurements include a continuous argon-ion laser coupled with an acousto-optic modulator, a xenon flash lamp and Kerr cell, a N_2 flash lamp, a condenser powered air spark gap, a nitrogen-pumped dye laser, and a Q-switched ruby laser [57,59, 72, 73, 74, 75].

Figure 4.5 (a) depicts the timing for the TOF experiment and a representative hole I-mode voltage transient signal for the experimental setup depicted in Figure 4.4. A transient voltage signal for electrons can also be generated using this system by reversing the polarity of the bias voltage (note that the captured signal would then be an inverted pulse). At time $t = 0$ the laser injects a narrow sheet of charge into the sample. The drift of the charge sheet across the sample thickness induces a transient photocurrent pulse in the external circuit. The mobility of the carriers in the charge sheet (i.e. holes) can be calculated by noting that the time width of the transient pulse corresponds to the transit time t_T of the charge sheet (the time it takes for the charge sheet to drift from the point of generation to the collecting electrode).

The TOF photocurrent pulse in a-Se typically exhibit a broadened falling edge, as depicted around the time t_T in Figure 4.5 (a). This so called *photocurrent tail* reflects the dispersion of the carriers in the charge sheet during transit, and it may be attributed to affects such as carrier diffusion, the mutual Coulombic repulsion between the charges,

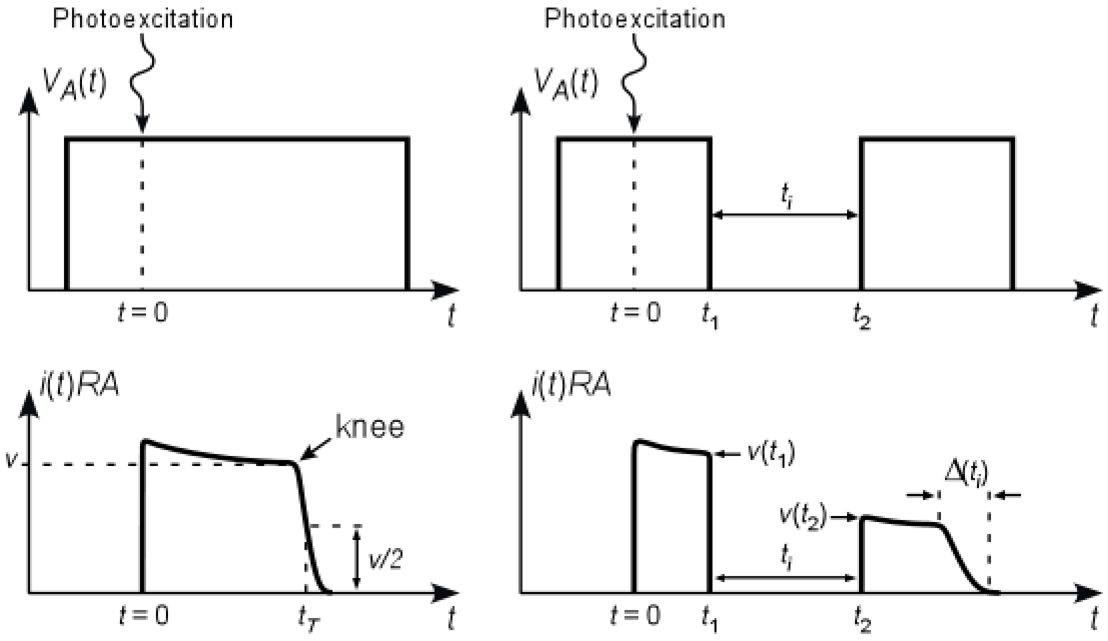

(a) (b)

Figure 4.5 The transient voltage response for the (a) TOF and (b) IFTOF signal. The signals are due to the drift of injected holes. The hole mobility is determined by measuring the width t_T of the TOF pulse. The hole lifetime is determined by interrupting the hole drift by temporarily removing the applied field. The magnitude of the recovered signal at time t_2 reflects the loss of holes to deep traps during time t_i.

and the multiple trapping to shallow states as described in Chapter 3. The carrier transit time is typically measured at the half magnitude point on the photocurrent tail, as shown in Figure 4.5 (a). This corresponds roughly to the time where half of the injected carriers have been collected and represents the mean transit time for the carriers in the charge packet. The mean carrier transit time may also be located by finding the "knee" in the photocurrent or by determining the inflection point on the photocurrent tail [76].

The drift mobility is determined from the measured transit time as follows. Since the holes are generated near the sample surface, it can be assumed that the charge sheet travels essentially the entire length L of the sample. Therefore, the average drift velocity of the charge sheet is $v_d = L/t_T$. Assuming that the internal field $F = V/L$ is uniform, the drift velocity of the charge sheet is constant and related to the effective hole drift mobility μ_h by $v_d = \mu_h F$. It is straightforward to show that

$$\mu_h = \frac{L^2}{Vt_T} \qquad 4.1,$$

where V is the magnitude of the applied bias. The same arguments can be made to calculate the effective electron drift mobility μ_e from the electron TOF waveform.

The timing of the IFTOF experiment and a representative IFTOF hole transient signal are illustrated in Figure 4.5 (b). Reversing the polarity of the applied voltage generates an electron IFTOF signal, and the following discussion may be applied to study the trapping kinetics of electrons. At time $t = 0$ a short duration laser pulse injects a narrow sheet of charge into the biased sample, and the drift of the injected charge sheet induces a photocurrent signal in the external circuit. At time $t = t_1$, the bias is removed from the sample so that the drift of the injected charge sheet is interrupted and the transient signal falls to zero. The charge sheet remains at this position until the bias is reapplied at time $t = t_2$ at which point the drift of the charge sheet resumes, inducing a post-interruption photocurrent signal is in the external circuit.

During the interruption time $t_i = t_2 - t_1$, some of the holes become trapped in localized states located deep in the mobility gap of the material and are effectively removed from the charge sheet for the remainder of the experiment. The loss of carriers is reflected in the magnitudes of the captured voltage transient signals before and after the bias interruption. For a discrete set of hole traps with a well defined capture time τ_h, it can be shown that the fractional recovered photocurrent signal $v(t_2)/v(t_1)$ is related to t_i by [77]

$$\frac{v(t_2)}{v(t_1)} = \exp\left(-\frac{t_i}{\tau_h}\right) \qquad 4.2.$$

The IFTOF measurement is repeated several times at the same interruption point to measure $v(t_2)/v(t_1)$ for various values of t_i. The slope of a semi-logarithmic plot of $v(t_2)/v(t_1)$ versus t_i determines the value of the carrier lifetime.

The main advantage of the IFTOF technique is that the trapping lifetime is measured at single position in the sample under zero field conditions. This position may be determined by noting that, in time t_1, the charge sheet drifts a distance ℓ, such that

$$\ell = \frac{\mu V t_1}{L} = L\frac{t_1}{t_T} \qquad 4.3.$$

By varying the location of the interruption position, the lifetime may be determined at several different locations in the sample to study the effects of in-homogeneities on the trapping time. Furthermore, the IFTOF technique is ideally suited to study materials with very long carrier lifetimes, because the interruption time may be varied over an interval that is much longer than the carrier transit time.

During the bias interruption, the mean position of the injected carrier sheet does not change; however, the carriers in the packet are still mobile, and the width of the packet will broaden due to the effects of diffusion and Coulombic repulsion. This spreading is reflected in the width $\Delta(t_i)$ of the IFTOF photocurrent tail as depicted in Figure 4.5 (b). When performing the experiment with a long interruption time or near an electrode, some of the carriers in the charge sheet may reach an electrode and be extracted from the sample. The magnitude of the recovered photocurrent will then reflect, not only the loss of carriers due to trapping, but also the loss of carriers due to this extraction effect. Therefore, care must be taken to ensure that charge carrier extraction has not occurred during the interruption interval. Provided that the broadened tail in the IFTOF signal does not extend to the interruption time, then it can be assumed that charge extraction did not occur.

The IFTOF experiment, though very useful, is a difficult technique to implement. In Figure 4.6, the high voltage switch is used to apply and remove the bias from the sample, while a laser injects charge carriers into the sample and a resistor converts the subsequent photocurrent into a voltage signal. The sample essentially consists of a high resistivity dielectric material sandwiched between two parallel metallic electrodes and can be modeled as a parallel plate capacitor with capacitance C_S. The switching of the

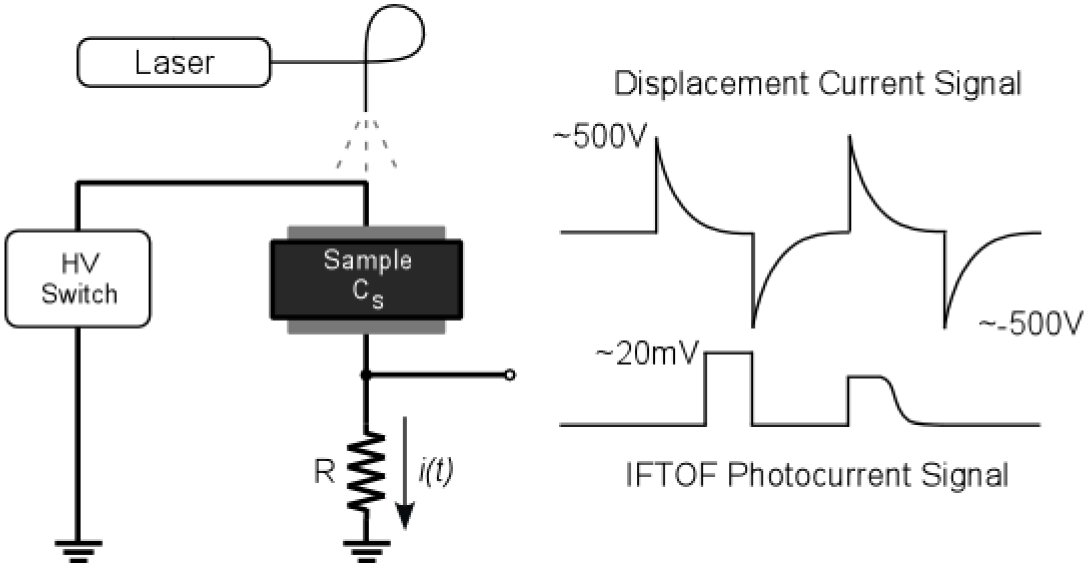

Figure 4.6 Application and removal of the high voltage bias during charge carrier transit produces a large displacement current signal which must be eliminated to implement the IFTOF technique.

bias across the sample results in a *displacement current* with a characteristic decay time equal to RC_S to accommodate the redistribution of charge on the electrodes of the sample. Depending on the magnitude of the applied bias, the displacement current signal can be quite large (i.e. > 100 V) and is generally orders of magnitude larger than the desired photocurrent signal (~ 20mV). These large displacement currents obliterate the desired IFTOF photocurrent and may damage the sensitive electronics required to amplify and capture this signal.

In the TOF experiment, protection of the signal electronics may be achieved by placing a relay between the sample and the input of the amplifier. The relay is normally open when the high voltage bias is applied or removed to the sample; after a time delay to allow the high-voltage switching transients to decay to negligible levels, the relay is closed to connect the amplifier to the sample in order to capture the photocurrent signal. In the IFTOF experiment, a relay protection scheme is not applicable because the switching time of typical relays (~1 ms) is several orders of magnitude larger than the minimum drift time (~1 μs) of typical IFTOF measurements.

Several other techniques for eliminating displacement currents in transient photoconductivity experiments have been published in the literature. Kasap and coworkers [60] used a complementary bias switching technique to eliminate the displacement current for voltages up to 200 volts. However, differences in the transient outputs of the switches made this technique impractical for larger values bias voltage. Helfrich and Mark [78] used a resistance ratio bridge network to eliminate the displacement current appearing in transient space charge limited current measurements in anthracene crystals. In their arrangement, the voltage power supply and bridge were floating, and only half of the applied voltage appeared across the sample. More recently, Polishuck and Kasap [79] used a floating Schering bridge configuration to produce displacement current free IFTOF measurements for bias voltages up to 1 kV. However, the floating voltage supply introduced significant stray capacitance into the circuit that made the bridge difficult to balance properly.

In the present investigation, a grounded bridge network was used to eliminate the displacement current signal. The advantage of this technique is that a grounded voltage supply may be used to bias the sample to allow for good RFI shielding. The concept of the bridge circuit is illustrated in Figure 4.7. The application and removal of the high voltage bias produces a displacement current signal in both branches of the bridge. If the variable capacitor C_N is adjusted so that it is equivalent to the sample capacitance C_S, then the displacement currents in the two bridge resistors will be the same and can be eliminated by performing a differential measurement across the bridge. The differential amplifier will detect the photocurrent signal because it appears in only one branch of the bridge.

Although it is conceptually simple, a pure differential measurement scheme is difficult to implement because of the stringent requirements that are placed on the differential amplifier; it should have a very large CMRR (~100dB) over a wide bandwidth, and it should be capable of withstanding very large common mode input signals without going into saturation. These requirements were overcome by placing back-to-back rectifiers across each bridge resistor to limit the magnitude of the displacement current signal to the nominal value of ~ 0.7 V (voltage drop across a

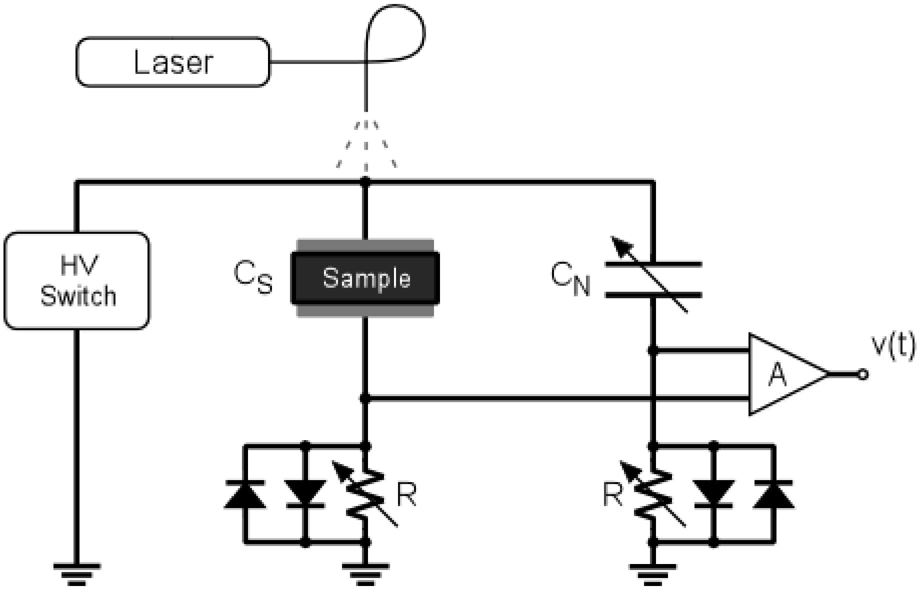

Figure 4.7 A grounded bridge network to eliminate the displacement current signal from IFTOF transient photoconductivity measurements.

forward biased diode) as shown in Figure 4.7. In such an arrangement, the high speed rectifiers limit the magnitude of the displacement current signal, and prevent the differential amplifier from entering saturation. The remaining common mode signal may be easily rejected using an amplifier with a modest 60dB CMRR provided that the bridge resistors are carefully matched.

4.4 TOF/IFTOF Experimental System

4.1.1 System Overview

A system capable of performing both TOF and IFTOF measurements is shown in Figure 4.8; it is based on a grounded bridge network to eliminate the displacement current signal in the IFTOF measurements. A variable, open-air capacitor C_N with a large breakdown voltage was used to balance the bridge. The large common mode switching transients were limited by placing two ultra-fast switching rectifiers (MUR120) across each of the bridge resistors. A differential amplifier placed across the bridge rejects the remaining common mode signal and amplifies the differential photocurrent transient

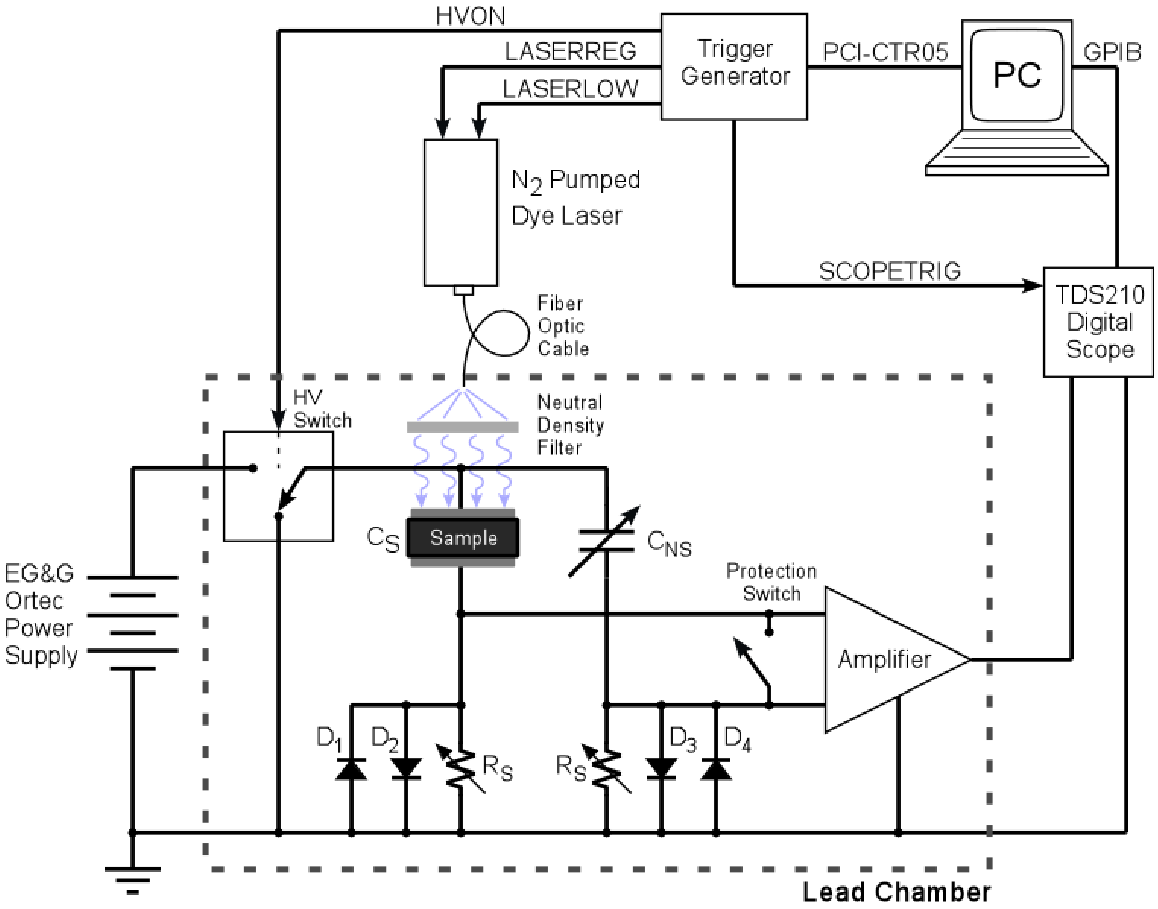

Figure 4.8 The TOF/IFTOF system schematic for 1kV displacement current-free measurements based on a grounded bridge network. Timing for the trigger signals is generated by a Computer Boards PCI-CTR05 counter board installed in the PCI bus of the PC. The photocurrent is captured by the digital oscilloscope and transferred to the PC via a GPIB interface.

signal as discussed above. To protect the amplifier from the switching transients, a CMOS analog protection switch shorts the amplifier input terminals during the switching of the high voltage.

The voltage bias was supplied by an EG&G Ortec high voltage (HV) power supply and was applied to the sample through a fast switching HV HEXFET switch. The trigger signals for the switches, laser, and oscilloscope were generated using a PCI-CTR05 counter board installed in the PCI bus of a Pentium II personal computer (PC) running Windows 95. The experiment operator controlled the timing of the experiment using a custom graphical user interface that was running on the PC. A Tektronix

TDS210 digital oscilloscope digitized and captured the photocurrent signal, and the digitized signal was uploaded to the PC for storage and analysis using a GPIB interface. The computer, trigger generator, oscilloscope, laser and high voltage power supply are shown in Figure 4.9.

An x-ray source was required to study the effects of x-ray exposure on the transport properties of a-Se alloys, and it was positioned directly above the sample holder. In order to protect the experiment operator from the hazardous effects of unnecessary exposure to x-ray radiation, the sample holder and x-ray source were placed in a large lead cabinet. The lead cabinet also provided a dark environment to perform the transient photoconductivity measurements; a fiber optic pigtail cable routed the optical excitation into the lead chamber. The HV switch, bridge network, and amplifier were also placed in the lead cabinet in order to be physically close to the sample holder as

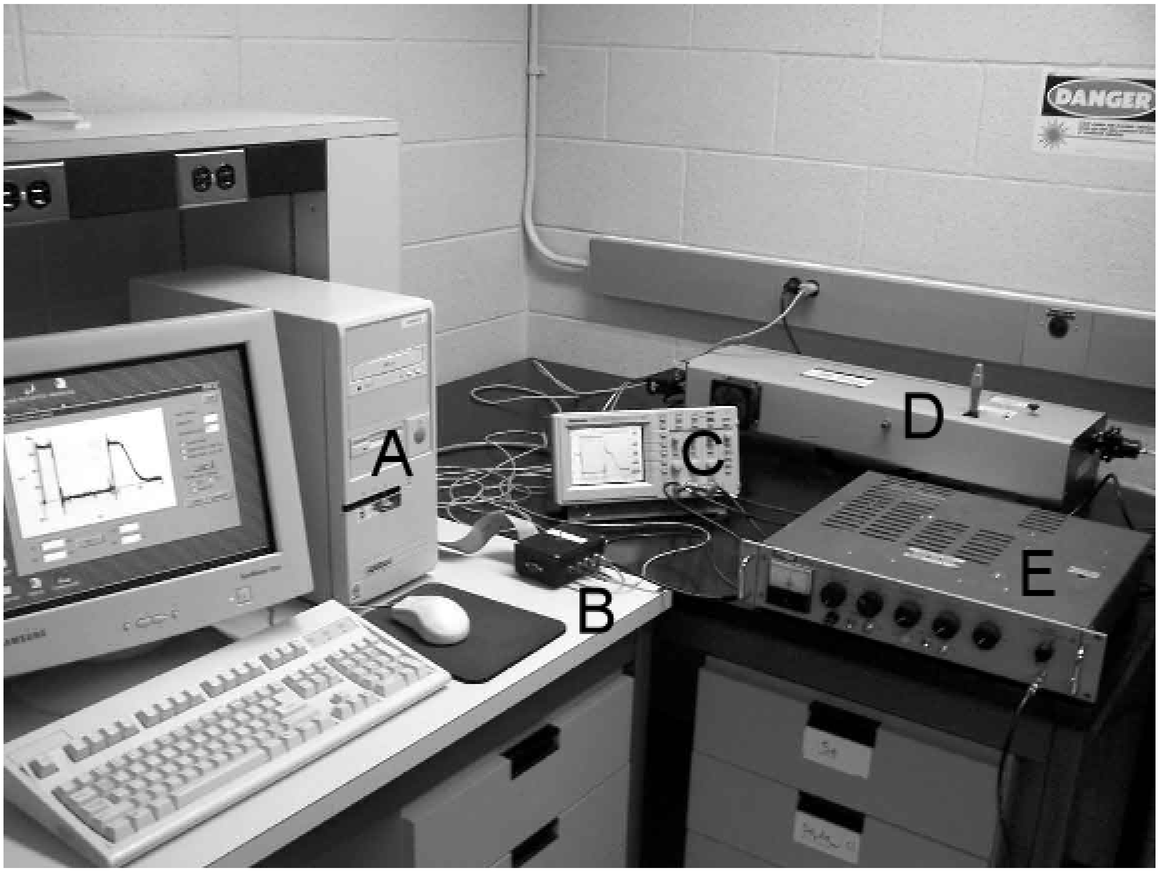

Figure 4.9 Picture of the experimental setup showing the (A) computer, (B) trigger generator, (C) the TDS210 oscilloscope, (D) the laser, and (E) the HV power supply.

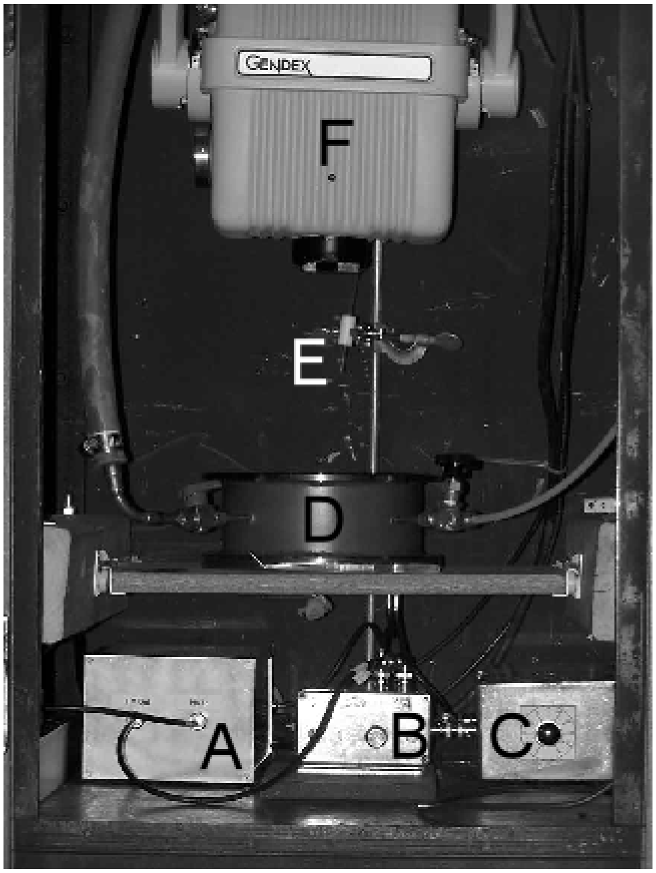

Figure 4.10 Picture of the inside of the lead chamber showing (A) the HV switch, (B) the variable capacitor, (C) the differential amplifier, (D) the sample holder, (E) the fiber optic cable, and (F) the x-ray tube.

shown in Figure 4.10. Co-axial cable was used throughout to route the various trigger signals, the HV bias, and the photocurrent signal.

By properly adjusting the variable air capacitor in the bridge it was possible to eliminate most of the displacement current signal. However, the dark current in the a-Se samples is not totally negligible, and increases sharply with the applied field F. In addition, the dark current typically decays with time. Such a time dependent dark current is equivalent to having a resistor $R_S(t,F)$ in parallel with the sample, where R_S depends both on time and on the applied field. Clearly it is very difficult to completely null out the transient current associated with this parallel C_S and $R_S(t,F)$ combination. Therefore, the bridge was adjusted until the net magnitude of the switching transients was on the order of magnitude of the photocurrent signal. To extract the net photocurrent signal, the

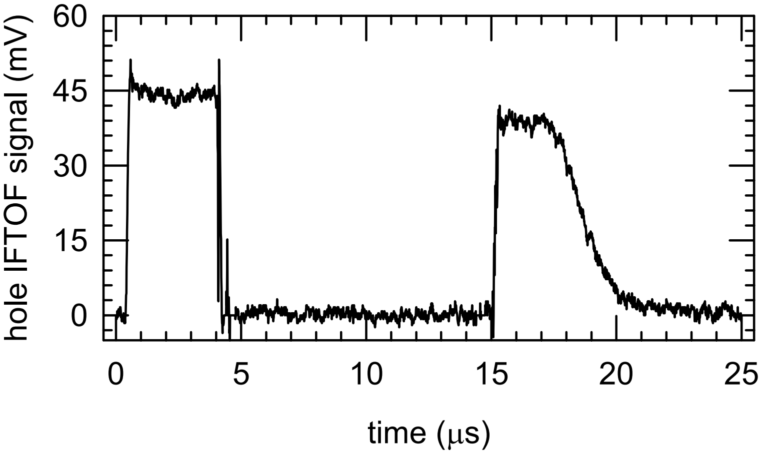

Figure 4.11 Displacement current free IFTOF signal for holes in a 102 μm thick sample of a-Se:As0.5% + 5 ppm Cl.

bridge was energized twice from the high voltage switch, once with photoexcitation and once without. The two waveforms were captured and digitally subtracted from one another to yield the net displacement current free photocurrent signal. It should be noted that digital subtraction techniques have been used before to successfully capture displacement current free IFTOF photocurrent signals [77,80].

Figure 4.11 illustrates the capabilities of the IFTOF system. This figure shows the hole IFTOF photocurrent signal from a 102 μm sample of a-Se:$As_{0.5\%}$ + 5ppm Cl where the displacement current is entirely eliminated using the hardware and digital subtraction techniques. The interruption time is 10 μs and the hole lifetime was measured to be 70 μs. The interruption time appears longer in Figure 4.11 because the amplifier protection switch is closed slightly before the HV bias is removed, and it is opened slightly after the HV is reapplied.

4.1.2 High Voltage Switch

In order to measure the bulk transport properties of low mobility materials such as a-Se photoconductors, a large bias must be applied to the sample. The samples investigated in the course of this work were relatively thick (~ 100 μm). Also, the carrier mobilites for the a-Se layers are generally in the range of 0.1 cm^2/Vs for holes and 2×10^{-3} cm^2/Vs for electrons. The relatively large thickness of the samples and the low mobility of the charge carriers mean that a very large bias $\leq$ 1kV must be applied to the sample in order to perform transient photoconductivity measurements. Further, with typical transit times for holes in the microseconds range, the removal and application of the voltage bias for the IFTOF experiment must have rise and fall times on the order of 0.1 μsec or less.

A high voltage (HV) switch capable of switching voltages up to 1kV was built using two fast switching n-chanel IRFBG30 HEXFETs connected in a totem pole configuration as shown in Figure 4.12. The gate voltages required to drive the HEXFETs quickly into conduction are supplied by two HCPL-3120 optocouplers, which also serve to isolate the control circuitry from the high voltage output of the switch. A floating, +18V power supply for the upper optocoupler prevents the gate-source voltage of the HEXFET from exceeding its maximum rated value of ±20V. An additional grounded

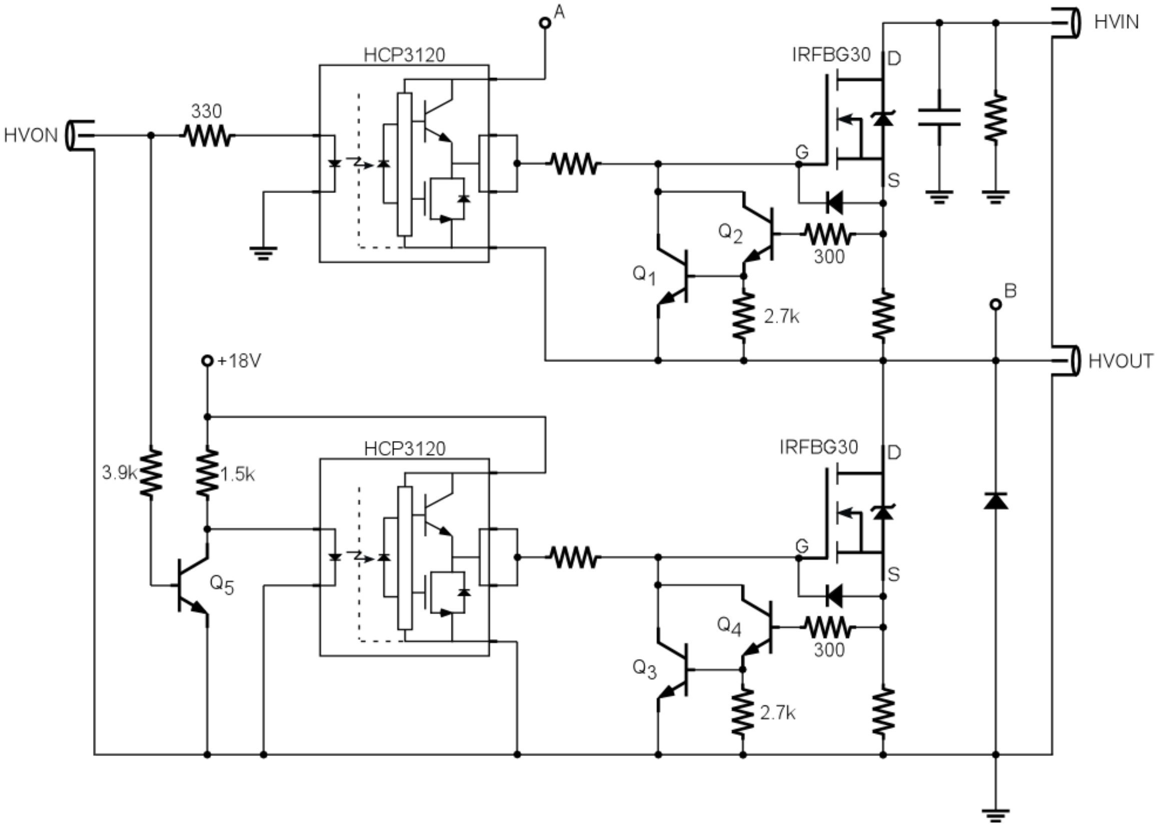

Figure 4.12 A 1kV fast switching high voltage HEXFET switch.

+18V power supply provides power to the lower optocoupler. The power supplies and decoupling capacitors have been omitted from the switch schematic for clarity. The BJT networks (Q_1-Q_4) between the gate and source of each HEXFET were designed to protect the power transistors in the case of a fault at the output of the switch. If the output current exceeds its maximum rated value, then the followers will turn off the HEXFET switches by providing a short circuit path between the gate and source terminals through the BJT follower, i.e., Q_1 and Q_3.

The bias voltage was supplied by an EG&G Ortec 556 high voltage power supply, which was connected to the input of the HV switch (HVIN). To provide a positive bias for the transient photoconductivity measurements, the output of the HV switch (HVOUT) was connected to the top electrode on the sample. The HV switch functions as a single-pole double-throw (SPDT) switch with the output normally connected to ground through the lower HEXFET. A +5V pulse at the trigger input (HVON) connects the high voltage power supply to the sample through the upper HEXFET for the duration of the trigger pulse. A BJT inverter (Q_5) at the input of the lower optocoupler ensures that only one HEXFET is conducting at a given time. Note that the HV switch will only work with a positive voltage input. Therefore, in order to capture transient photoconductivity measurements for electrons, the output of the switch was connected to the sample substrate, and the top electrode was connected to the sampling resistor and signal electronics.

4.1.3 Amplifier

A wide bandwidth, 2-stage differencing amplifier was designed to detect and amplify the differential photocurrent signal from the common mode displacement current signal. The schematic diagram of the amplifier is shown in Figure 4.13. The first stage consists of a wide bandwidth, high CMRR video amplifier from Analog Devices (AD830) configured as a unity gain differential amplifier. This amplifier is specified to have a unity gain bandwidth of 85 MHz and a CMRR of 60 dB at 4 MHz. The second stage is a non-inverting amplifier designed using an Analog Devices high-speed

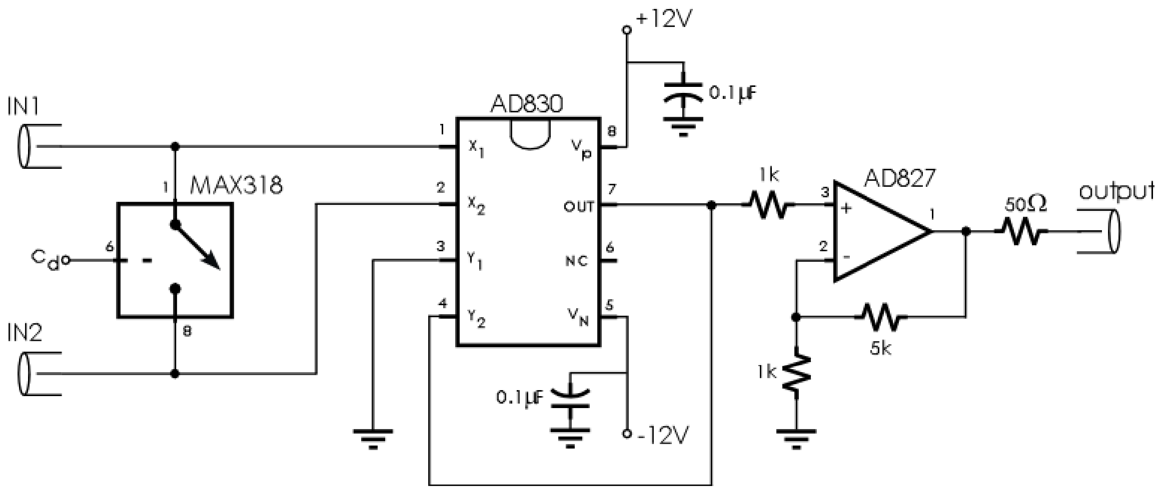

Figure 4.13 A 2-stage wide bandwidth difference amplifier with 16 dB of gain.

operational amplifier (AD827) to drive the relatively large capacitance introduced by the coaxial cable connecting the amplifier output to the oscilloscope. This stage was designed with a gain of 16 dB to raise the photocurrent signal above of the noise floor of the digital oscilloscope. The power supply and decoupling capacitors have been omitted from the amplifier schematic for clarity of presentation.

A precision, normally open CMOS analog SPST switch from Maxim (MAX318) was placed across the inputs of the amplifier to protect the signal electronics from the high voltage transients during switching. The switch was selected for its low charge injection (~10 pC). The trigger pulse for the analog switch was generated using a monostable multivibrator (LS123) and a positive-edge-clocked D flip-flop (LS74) as shown in Figure 4.14 (a). The timing diagram for the switch control signal is shown in Figure 4.14 (b). The amount of post interruption delay t_S may be adjusted by varying the resistance in the resistor-capacitor network connected between pins 15 and 14 of the LS123. The CMOS switch may be permanently damaged if the absolute maximum ratings of the device are exceeded. Therefore, two small diodes (1N914) were placed in series with the supply pins in order to provide overvoltage protection.

The small signal pulse response of the amplifier is depicted in Figure 4.15 (a). The width of the input pulse is ~ 1.2 µs, characteristic of the minimum pulse widths

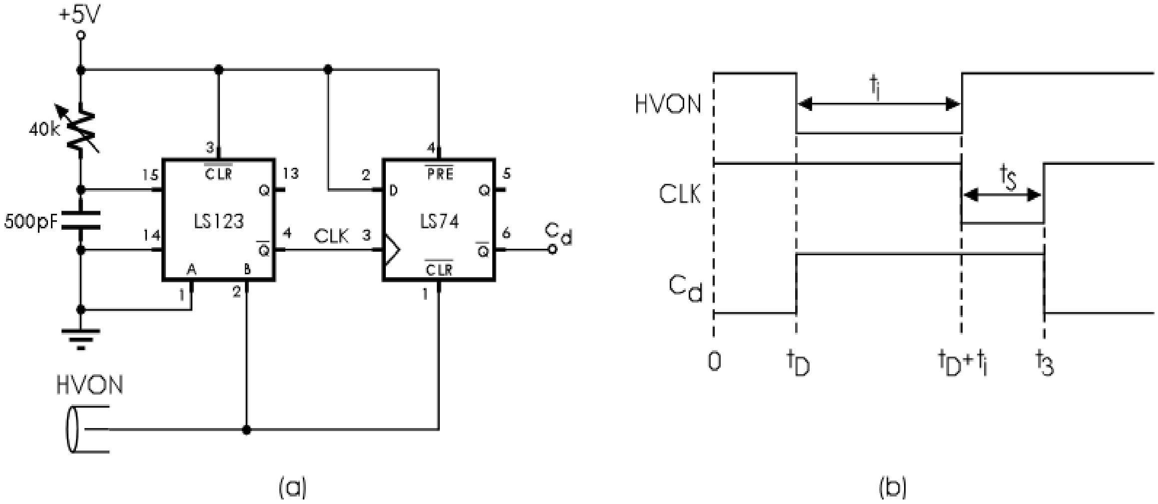

(a)
(b)

Figure 4.14 The trigger signal for the MAX318 analog switch is generated using the circuit in (a). The timing diagram for the signal is shown in (b). The delay time t_S may be adjusted using the 40kΩ potentiometer.

expected for this investigation, its magnitude is 100 mV. The small signal gain of the amplifier was measured to be 16dB. The small signal bandwidth may be estimated from the rise time of the output pulse. For the pulse shown in Figure 4.15 (b), the rise time is 48ns, which corresponds to a small signal bandwidth of 12MHz. Since the smallest expected transit times are ≥ 1 μs, the performance of this amplifier is suitable for carrying out TOF and IFTOF measurements on samples of a-Se.

4.1.4 Laser

A Laser Photonics LN103C nitrogen-pumped dye laser was used to inject charge into the samples. The laser incorporates a patented spark gap design to produce a 300ps output pulse with a ±2ns jitter. The peak power of the nitrogen laser is rated at 250kW and the spectral output has a peak energy wavelength of 337.1 nm with a 0.1nm spectral spread.

The LN103C laser was triggered by the application of two TTL level signals to BNC inputs located on the rear panel of the instrument. First, a +5V pulse of at least 100 ns in duration is applied to the *Trigger Reg* input to charge the laser. Between 30 and 50

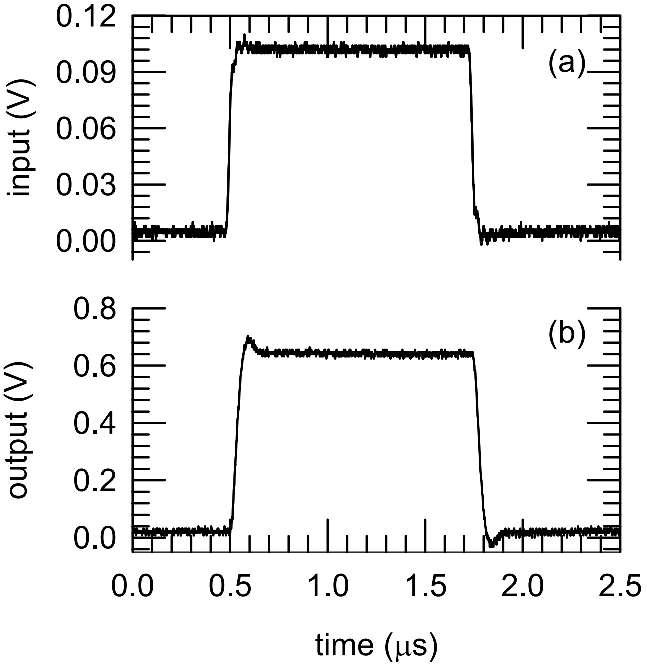

Figure 4.15 (a) A 100 mV pulse is applied to the input of the amplifier. (b) The output pulse. The differential pulse gain of the amplifier was measured to be 16 dB, and the signal bandwidth was estimated from the pulse rise time to be 12 MHz.

μs later, a second +5V pulse of at least 100 ns in duration must be applied to the *Trigger Low* jack to fire the laser, producing laser radiation at the exit aperture. If the second pulse does not occur within the firing window, the laser will self fire at 60 μs, with a self jitter of 50 ns or less. The jitter with respect to the pulse applied to the *Trigger Low* is approximately 2 ns when the spark gap is adjusted for optimal performance as described in the LN-Series Nitrody/Nitromite operating/service manual. Figure 4.16 is a plot of the timing sequence required to fire the nitrogen laser correctly. The firing of the laser requires a high voltage discharge through a spark gap circuit. In order to reduce the feedback of the large switching transients into the control circuitry of the IFTOF system, the laser trigger signals were optically coupled to the laser control inputs.

The exit aperture of the LN103C laser was fit with a Newport Optical Fiber adapter (model MM-2A) to allow efficient coupling of the laser light into a fiber optic pigtail cable. The cable is routed into the lead chamber containing the sample holder and the cable end is situated ~ 10 – 20 cm above the sample to provide uniform illumination

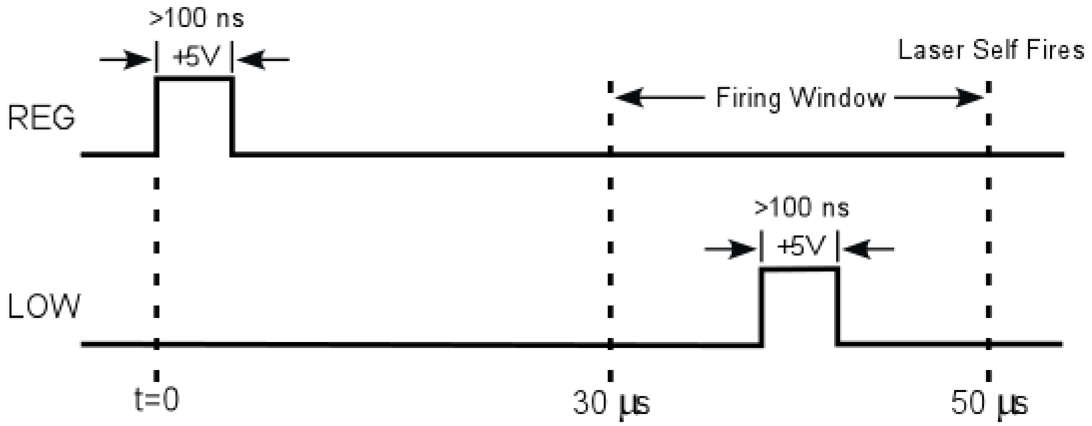

Figure 4.16 Trigger timing requirements of the LN103C nitrogen laser.

of the semitransparent contact area. A mask placed overtop of the sample is used to eliminate photogeneration near the edges of the contact where the field is not uniform. One or more neutral density optical filters may be placed between the fiber end and the sample to control the intensity of the light used for charge carrier photogeneration.

4.1.5 Trigger Generator

The trigger signals for the IFTOF system were generated using a Computer Boards PCI-CTR05 counter board installed in the PCI bus of a personal computer (PC). The heart of the counter board is an AMD 9513 counter/timer chip that contains five 16 bit up/down counters. The counter board is fully supported by the Computer Boards Universal Library of programming functions, which provides high-level software control of the counter registers on the 9513. The trigger generator code was written in C++ and was integrated into the TOF/IFTOF user interface software.

The output of the counter board was interfaced with the IFTOF system using the trigger generator circuit shown in Figure 4.17. A ribbon cable connected the output of the counter board to the interface circuit, which was placed in a separate aluminum case. Power for the logic gates was supplied from the power bus of the PC. The state of the high voltage bias could be manually controlled using the switch to select one of three settings; on, pulsed, and off. A normal IFTOF experiment would be performed with the

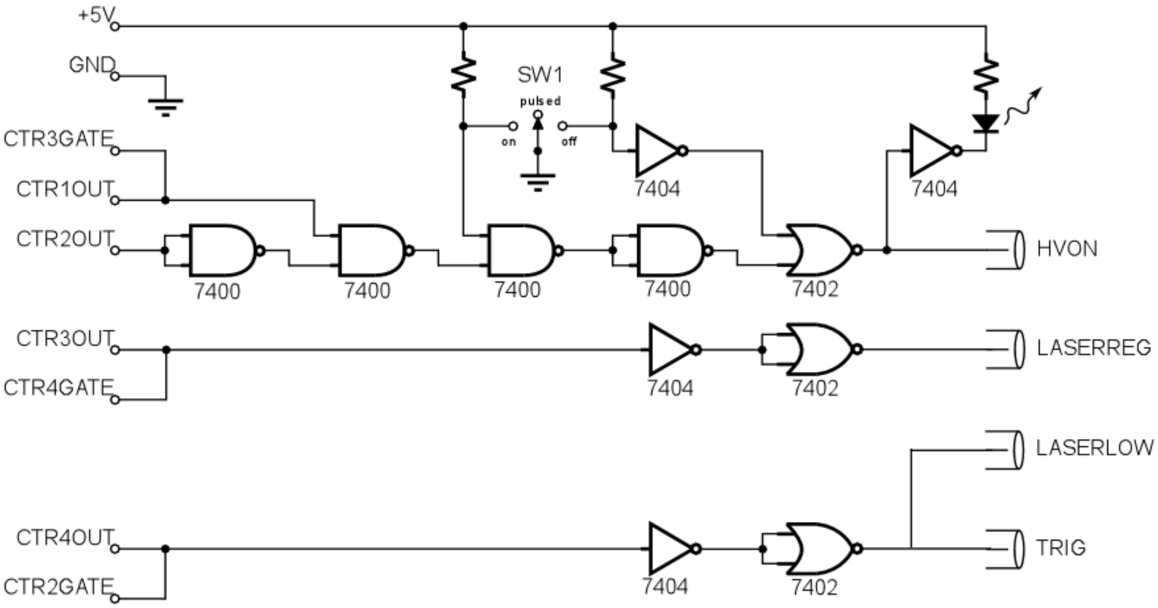

Figure 4.17 The PCI-CTR05 interface circuit for generating the trigger signals for the IFTOF system.

switch set to the pulsed position. An LED mounted on the top of the trigger generator case provided visual feedback as to the state of the HV bias.

The timing of the counter board output and the resulting trigger signals are shown in Figure 4.18 when the switch is in the HV pulsed or normal position. The HVON trigger signal controls the application of the bias to the sample by triggering the high voltage switch. A delay of t_{HV1} seconds allows the displacement current due to the application of the bias to the sample to decay to negligible levels. Following this delay, a 100 ns LASERREG pulse initiates the charging of the laser. After a delay of 40 μs, a 100 ns LASERLOW pulse is generated to fire the laser and inject charge into the sample. The scope is simultaneously triggered with the firing of the laser in order to capture the resulting photocurrent pulse.

In the TOF experiment, the HVON signal is not interrupted and the bias remains applied for a sufficient time in order that all the charge carriers may be collected at the collection electrode (i.e. ~100 ms). In the IFTOF experiment, the bias is interrupted after a user specified delay time t_D. After an interruption period of t_i seconds, which is also

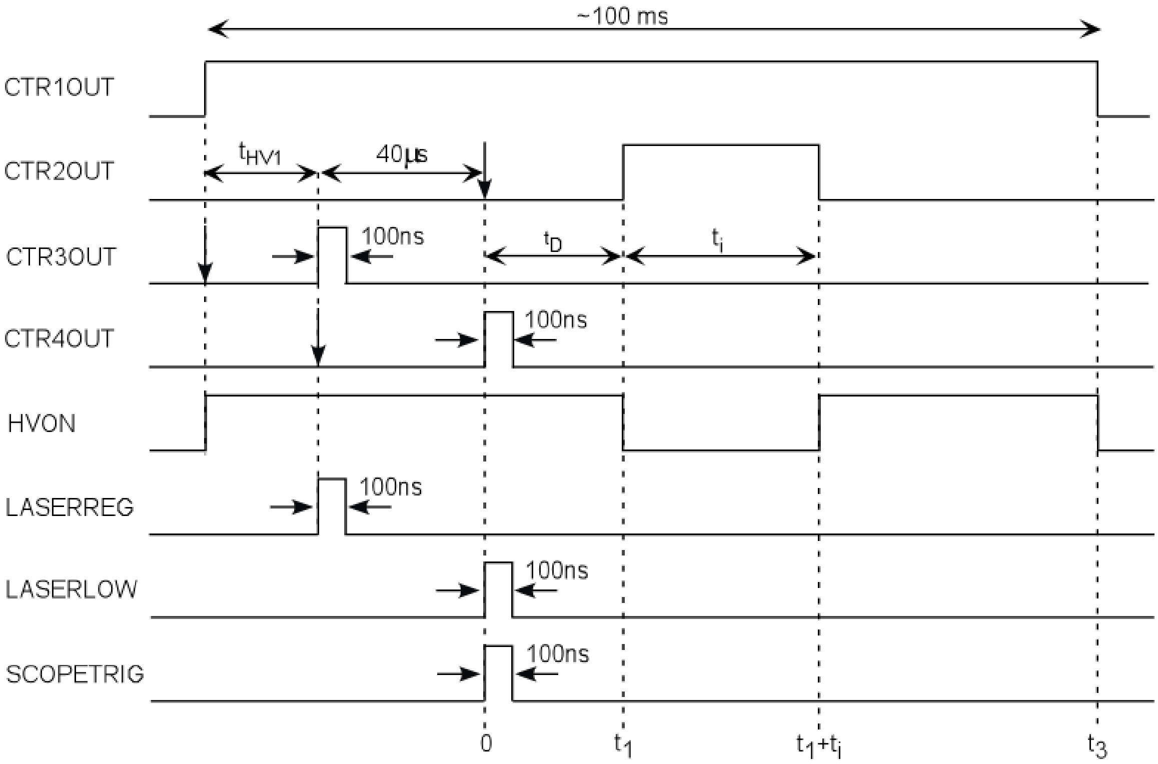

Figure 4.18 Timing signals from the PCI-CTR05 counter board and the interface circuit. The timing sequence t_D and t_i are set by the experimental operator.

specified by the user, the bias is reapplied for a sufficient period such that all the charge carriers that remain in the charge sheet are collected (~100ms).

4.1.6 Signal Capture and System Interface

The photocurrent signal was captured using an 8-bit Tektronix TDS210 digital oscilloscope with a sampling rate of 1 GS/s. The obvious advantage of using a digital oscilloscope is that the waveform data may be directly downloaded to a PC for storage and analysis. This was facilitated using a GPIB connection between the oscilloscope and the PC. The vertical and horizontal settings on the oscilloscope were adjusted as necessary to capture a wide range of signal pulse magnitudes and durations. In order to limit the amount of noise in the captured signal, the bandwidth of the oscilloscope was limited to 20 MHz.

A custom software program was created using Visual C++ to control the timing signals of the experiment, communicate with the digital oscilloscope, and display the captured signal to the experiment operator. The front end of the program consisted of a dialog window containing fields for the user to specify the delay time t_D and the interruption time t_i. In order to capture a TOF waveform, both of these fields should be set to 0. The transient photoconductivity experiment was then initiated by clicking on a button in the program window. The bridge was excited without photoexcitation, and the baseline signal was captured and uploaded to the computer. The bridge was then automatically re-excited after a short pause, this time with photoexcitation, to capture and upload the photocurrent signal. A software routine subtracted the two signals and the resulting waveform was displayed on the screen. The digitized signal was saved as a tab delimited text file and exported to numerical analysis software, such as Microsoft Excel, for measurement and analysis.

4.5 X-ray System

The X-ray source used to irradiate the a-Se photoconductor layers was a Gendex GX-1000 dental x-ray system. This system consists of an x-ray tube head and a separate control unit. The tube head contains a tungsten anode and a hot filament cathode to release electrons. The electrons are accelerated by a large electric field and impact the anode at high velocity to produce wide spectrum x-ray radiation and heat. The tube head is encased in an oil-filled lead enclosure to facilitate the dissipation of heat from the target. The exit aperture of the x-ray tube was was positioned ~30cm directly above the sample holder inside the lead x-ray cabinet. The x-ray tube contains an inherent 2.5 mm of Al filtering. Additional metal filters may be placed between the exit aperture and the sample as required to adjust the mean x-ray energy of the beam.

The tube current can be set to either 10 or 15 mA while the tube voltage may be varied continuously from 50-100 kVp. The x-ray beam consists of a series of 1/60th second impulses due to the self rectifying nature of the tube and the 60 Hz power supply voltage. The duration of the beam could be varied from a minimum of 3 impulses to a 5 second long “train” of impulses. Over the duration of the beam, the temperature of the anode increases, so the duration of the x-ray output must be limited to prevent damage to the tube head. The maximum continuous duty cycle is 4,000 heat units per minute where Heat Units = mA × kVp × Exposure Time (in seconds). The maximum continuous duty cycle can be thought of in terms of the maximum number of exposure-seconds allowed in a five minute interval. These values depend on the selected kVp and mA, as shown in Table 4.1, and may be applied continuously to consecutive 5 minute intervals.

Table 4.1 Maximum number of exposure seconds that may be allowed a five minute interval.

KVp	**Exposure-seconds in 5 minutes (s)**	
	10 mA Setting	**15 mA Setting**
50-70	30	20
80	26	17.5
90	23	15.5
100	21	N/A

Proper safety guidelines must be observed when operating x-ray equipment. Therefore, the x-ray tube was installed in a lead lined cabinet manufactured by X-ray Products Corporation of Pico Rivera, California, shown in Figure 4.19. The control panel for the x-ray system was mounted on the side of the unit, and a door on the front of the unit facilitated access to the cabinet interior. The door was fitted with a magnetic disable switch to prevent accidental triggering of the x-ray tube with the cabinet door open. A red light located above the door serves as a warning that the x-ray system is turned on and that proper precautions should be observed. A specially designed “maze” located in the top portion of the cabinet allowed the electrical and optical cables to be routed into the interior of the cabinet.

Figure 4.19 This lead cabinet shields the experiment operator from exposure to x-ray radiation. The controls for the x-ray system are mounted on the right hand side of the cabinet. The light above the door indicates that the x-ray system is activated.

The effects of x-rays in a-Se photoconductor layers were measured as a function of x-ray exposure, the unit of which is the Roentgen (R). This unit quantifies exposure to ionizing radiation such that 1 R of x-ray exposure produces ions resulting in a charge of 0.000258 C/Kg in air under standard conditions. The total exposure depends on the distance from the exit aperture of the x-ray tube head, the mA and kVp settings of the tube, the amount of filtration, and the duration of the x-ray beam.

The x-ray exposure for a given set of conditions was measured using a Keithley 96035 ionization chamber connected to a Keithley 35050 dosimeter. The ion chamber and dosimeter were calibrated at the Cancer Center at the Royal University Hospital, University of Saskatchewan, Saskatoon. To measure the exposure, the ion chamber was placed at the position of the sample underneath the x-ray tube, and the output of the dosimeter was connected to a Fluke 8000A digital multi-meter. The dosimeter produces a voltage reading that is proportional to the x-ray radiation, and the x-ray exposure can be characterized for a given set of conditions. This measurement was performed several times to determine the exposures for the various settings used during the course of this investigation.

4.6 Summary

This chapter provided a comprehensive outline of the various experimental procedures employed during the course of this investigation. Samples of stabilized a-Se were prepared using conventional vacuum techniques; a semi-transparent metal electrode was sputtered onto the surface of the film to facilitate transient photoconductivity measurements. In the TOF experiment, the carrier drift mobility is measured by capturing the transient pulse generated due to the drift of a photo-injected charge sheet. In the IFTOF experiment, the drift of the injected charge sheet is interrupted by temporarily removing the applied bias; the carrier lifetime is determined by measuring the fractional recovered photocurrent. The displacement current associated with removing the applied bias in the IFTOF technique is very large, and it obliterates the desired photocurrent signal. A grounded bridge network arrangement was used to eliminate this displacement current signal; high-speed rectifiers limit the magnitude of the displacement current signal, and a differential amplifier detects the photocurrent signal from the remaining switching transients. A detailed description of the IFTOF system constructed for the present investigation was presented. A description of the x-ray system used to examine the effects of x-ray exposure on the charge transport properties was also presented.

5. RESULTS AND DISCUSSION

5.1 Introduction

In the previous chapters, the theoretical and experimental details of the TOF and IFTOF transient photoconductivity techniques were explained. In this chapter, the experimental results of the application of these techniques to various samples of stabilized a-Se photoconductive layers are presented. The TOF and IFTOF were used to determine the charge carrier drift mobility and trapping time (lifetime). The effects of the alloy composition on these transport parameters were systematically examined; the product of the mobility and lifetime determines the carrier range, which is an important parameter in determining the x-ray sensitivity of the photoconductor layer. The effects of negative bulk space charge on the transient photocurrent signal were examined, and a method to calculate the recombination coefficient between drifting holes with trapped electrons using a combination of TOF and IFTOF was derived. The effects of x-ray exposure on the transport properties of stabilized a-Se photoconductor layers were also examined.

5.2 Charge Carrier Transport in Stabilized a-Se

The inherent charge transport properties of stabilized a-Se photoconductors were measured using TOF and IFTOF transient photoconductivity techniques. These techniques capture the transient signal generated when a narrow sheet of charge is injected into a biased sample with a short pulse of strongly absorbed optical radiation. Both holes and electrons may be examined by properly selecting the polarity of the applied bias. The time width of resulting I-mode TOF pulse corresponds to the transit time of the injected carriers, and may be used to determine the carrier drift mobility μ. In the IFTOF technique, the drift of the carriers, and hence the photocurrent signal, is temporarily interrupted during the transit across the sample. The lifetime τ of the injected carriers in the presence of deep traps at the location of the interruption is determined by examining the ratio of the photocurrent signal before and after the interruption period.

The proper interpretation of the transient photoconductivity experiments involves the assumption that the internal electric field set up by the applied voltage V is uniform and determined by V/L, where L is the sample thickness. Following the application of the bias, a small amount charge is injected into the layer at the electrodes and becomes trapped in the bulk of the sample. Eventually the concentration of this bulk space charge is sufficient to alter the profile of the internal field. The time at which this occurs is known as the transition time t_{sc}; prior to this point it may be assumed that the internal field is uniform [81].

For a-Se films, it has been shown that t_{sc} is on the order of 100 ms [50]. In the present work, the photoexcitation pulse occurred a few milliseconds after the application of the bias to ensure that the internal field in the sample was uniform during the TOF experiment. This is readily confirmed by examining the shape of the TOF photocurrent pulse in samples with sufficiently long lifetimes; a pulse with an almost rectangular shape indicates a constant field and carrier drift velocity. Furthermore, a plot of the hole transit time t_T versus $1/V$ in stabilized a-Se layers is linear [33]; this indicates that the field is indeed uniform for the TOF measurements, provided that small signal conditions are observed during the experiment.

If the photoexcitation occurs well beyond t_{sc}, then the photocurrent will either decay or increase depending on the sign of the bulk space charge as demonstrated by Kasap and Juhasz for Cl-doped selenium [70]. The same effect can also be observed by repeating the TOF experiment at a constant repetition frequency [82] for a long period of time. In the case of hole drift, the photocurrent will increase because trapped holes reduce the field near the positive electrode in a similar fashion to the case of space charge limited conduction in insulators. The photocurrent then follows the electric field profile, which is determined by the Poisson equation $dE/dx = \rho/\varepsilon$, where ρ is the density of the space charge. The bulk space charge can be discharged through recombination with photogenerated carriers by shorting the sample and pulsing it several times with the optical source. Therefore, the sample was discharged and rested between each experiment in order to eliminate the effects of bulk space charge on the TOF and IFTOF measurements.

Figure 5.1 shows the typical I-mode hole and electron TOF photocurrent signals measured on a 224 μm thick sample of a-Se:$As_{0.2\%}$. The hole waveform in Figure 5.1 (a) exhibits an almost rectangular shape which indicates that there is no effect from bulk space charge and that there is negligible trapping during the transit time of the holes. The electron photocurrent signal in Figure 5.1 (b) displays a rapid initial decay followed by plateau region of constant magnitude. This phenomenon may be due to either carrier thermalization or the effects of fractionation. In the first case, a certain amount of time is necessary for the photo-injected electrons to reach equilibrium with the shallow traps in the mobility gap of the semiconductor. In the later case, a larger concentration of As near the surface of the film alters the transport behavior of the electrons in this region.

All TOF photocurrent signals exhibit a photocurrent tail due to the dispersion of the carriers in the charge packet during transit. The width of the photocurrent tail increases with the transit time t_T, so it is important to establish a consistent method of measuring the width of the photocurrent pulse in order to compare the carrier mobility measured in different samples and for different fields. The half peak-magnitude method measures the time width of the photocurrent pulse between the leading edge of the pulse and the half magnitude point on the photocurrent tail as shown in Figure 5.1. In the case of a strongly decaying TOF signal, the magnitude of photocurrent tail is determined at the location of the “knee” in the waveform pulse. The inflection-point method measures the time distance between the inflection point of the leading edge of the pulse and the inflection point of the photocurrent tail. This is readily determined by numerically calculating the

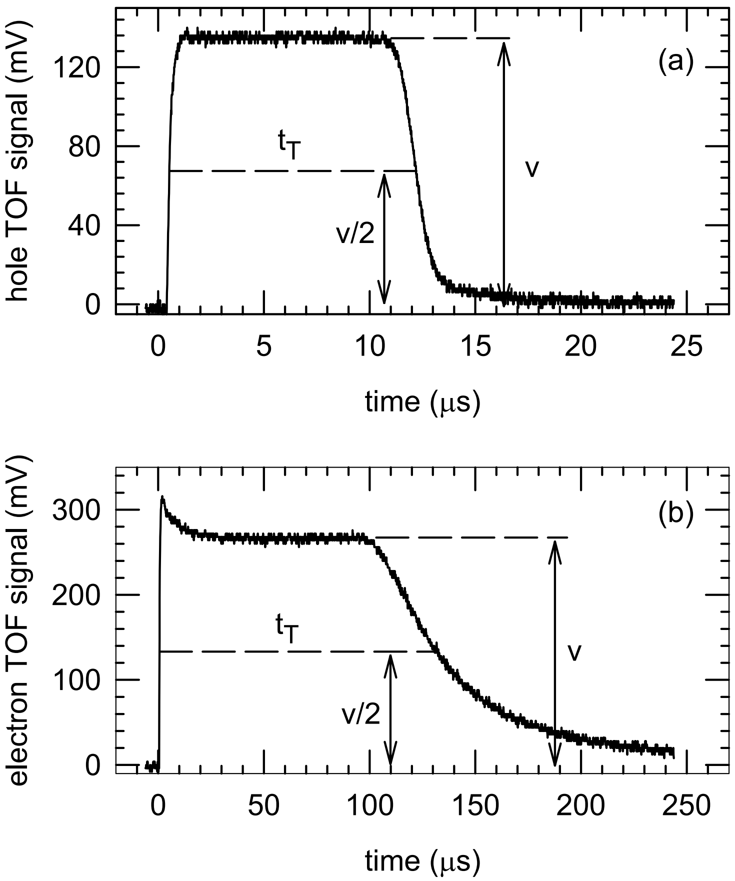

Figure 5.1 The I-mode TOF waveforms from a 224μm thick film of stabilized a-$Se:As_{0.2\%}$. (a) The hole waveform was captured with an applied field of 1.34V/μm, and transit time was determined to be 11.67μs. (b) The electron waveform was captured with an applied field of 4.02V/μm, and the transit time was determined to be 130μs.

derivative of the TOF waveform and finding the distance between the maximum and minimum points on this curve as shown in Figure 5.2. The algorithm that was used to calculate the numerical derivative of the TOF signal is outlined in reference [50].

Once the transit time is determined, the carrier mobility may be calculated from $\mu = L^2/Vt_T$. For the TOF signals illustrated in Figure 5.1, the hole transit time was determined to be 11.7±0.2 μs from the half peak-magnitude method and 11.5±0.2 μs from the inflection point method. These values correspond to a hole mobility of 0.143±0.006 $cm^2V^{-1}s^{-1}$ and 0.144±0.006 $cm^2V^{-1}s^{-1}$ respectively. The transit time for the electron TOF waveform was determined to be 130±2 μs from the half peak-magnitude

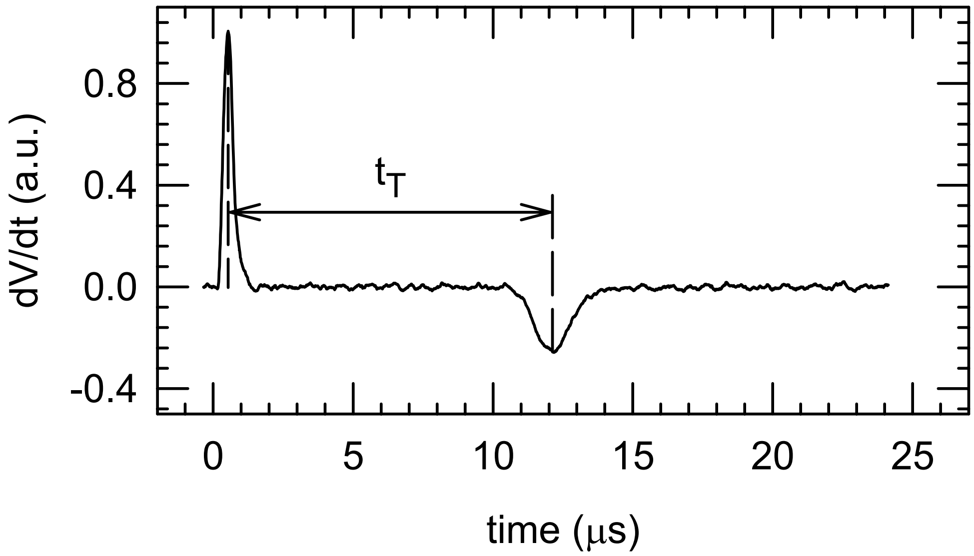

Figure 5.2 The derivative of the hole TOF photocurrent from Figure 5.1. The maxima in the waveform correspond to the inflection points in the leading edge and photocurrent tail of the TOF signal. The distance between these points determines t_T. In this figure, t_T = 11.58 μs.

method and 117±2 μs from the inflection method. The corresponding electron mobilities are $(4.3\pm0.2)\times10^{-3}\mathrm{cm^2V^{-1}s^{-1}}$ and $(4.7\pm0.2)\times10^{-3}$ $\mathrm{cm^2V^{-1}s^{-1}}$ respectively. For the subsequent discussion, the transit time will have typically been calculated using the half magnitude method because it is computationally simpler to perform.

IFTOF measurements were used to measure the mean charge carrier lifetime in the bulk of stabilized a-Se x-ray photoconductor layers. The magnitude of the photocurrent signal is proportional to the mean concentration of mobile photo-injected charge carriers and their average drift velocity, i.e. $i(t) \approx ep(t)v_d(t)$. If the experiment is performed under small signal conditions, i.e. the concentration of injected charge $p(t)$ is much less than the charge residing on the electrodes, then the drift velocity v_d remains constant for the charge carrier packet inasmuch as the mobility is a material property and the electric field is uniform. At time t_1, the applied field is removed and the drift of the carriers is halted. While the packet remains at this position, carriers are lost due to trapping events, so that, when the field is reapplied at time t_2, the magnitude of the recovered photocurrent has decreased. By measuring the magnitude of the photocurrent signal at times t_1 and t_2, the fraction of carriers lost during the interruption time can be determined since

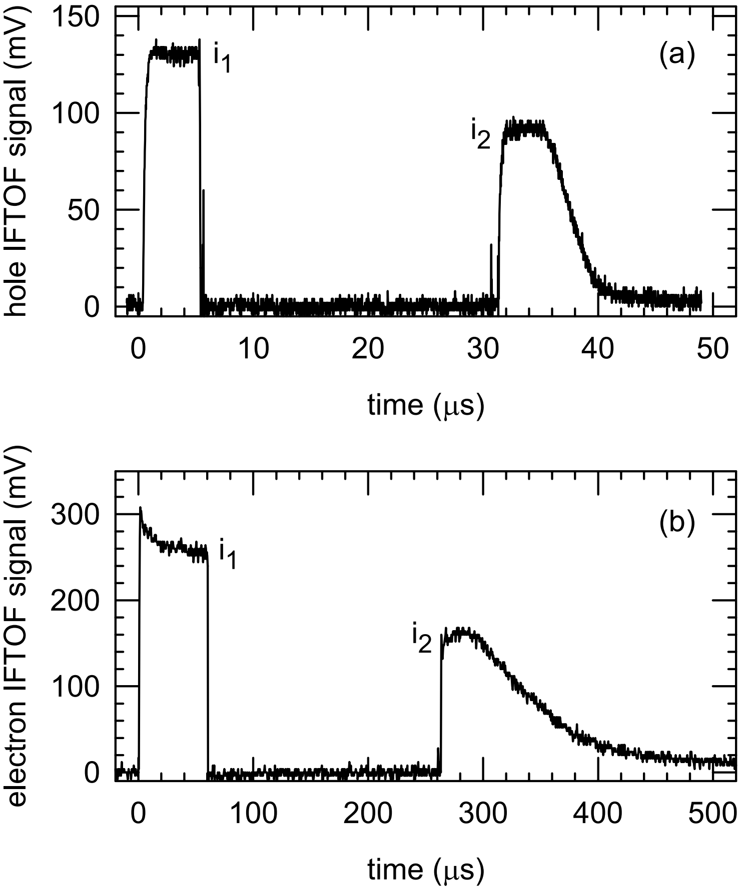

Figure 5.3 IFTFO signals captured for a 224μm sample of a-Se:As$_{0.2\%}$. (a) The hole interruption location was 96μm and the interruption time was 25μs. (b) The electron interruption location was 103μm and the interruption time was 200μs.

$i(t_2)/i(t_1) = n(t_2)/n(t_1)$. In the presence of a discrete set of deep traps with a well-defined capture time τ, it can be shown that $n(t_2)/n(t_1) = \exp(-t_i/\tau)$ where $t_i = t_2 - t_1$ is the interruption time. A semilogarithmic plot of $i(t_2)/i(t_1)$ versus t_i will therefore be a straight line, the slope of which corresponds to the deep trapping lifetime.

Figure 5.3 shows typical IFTOF signals that were measured for the holes and the electrons in the same 224μm thick sample of a-Se:As$_{0.2\%}$ that was mentioned previously. The interruption times for the signals in Figure 5.3 were 25μs for the hole IFTOF measurement and 200μs for the electron IFTOF measurement. The location of the interruption point can be determined from $x_1 \approx t_1 L/t_T$, where t_T was measured in a

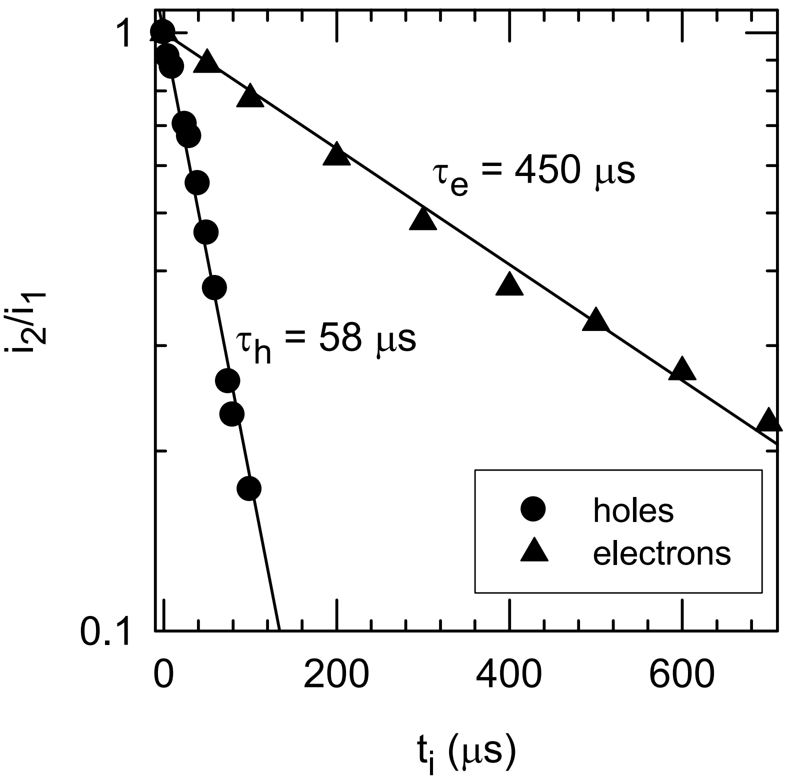

Figure 5.4 A plot of the fractional recovered photocurrent i_2/i_1 versus interruption time for holes and electrons in a 224 μm thick a-Se:As$_{0.2\%}$ specimen.

conventional TOF measurement performed at the same applied bias as the IFTOF measurement, and L is the thickness of the sample. For the signals shown in Figure 5.3, the interruption location x_1/L is 0.43 for holes and 0.46 for electrons. IFTOF experiments were repeated at these interruption locations for various values of t_i and the fractional recovered photocurrent $i(t_2)/i(t_1)$ was measured in each case. The results are plotted in Figure 5.4. As expected, the semilogarithmic plot of $i(t_2)/i(t_1)$ versus t_i reveals a pure exponential dependence. The hole and electron lifetimes, as calculated from the slope of the best-fit lines to the plots in Figure 5.4, are 58 μs and 450 μs respectively.

5.3 The Effects of Alloy Composition on the Charge Carrier Range

In this section, the results of the study on the effects of alloy composition on the charge transport properties in stabilized a-Se films are presented. Device quality a-Se layers are typically alloyed with As in order to prevent crystallization of the film. The resulting alloy, called stabilized a-Se, is thermally stable; however, the introduction of As atoms into the a-Se structure increases the concentration of deep hole traps, thereby reducing the hole lifetime and the x-ray sensitivity of the film. The reduction in the hole lifetime may be compensated for by adding a halogen (typically Cl) in the ppm range. The charge transport properties of stabilized a-Se films are important inasmuch as the product of the mobility and lifetime determines the carrier range and, hence, the x-ray sensitivity of the photoconductor.

5.3.1 Background

In the past, the effects of As and Cl addition on the charge transport properties of stabilized a-Se photoreceptor films were studied using either xerographic or conventional TOF experiments. In the xerographic experiment, the residual potential that results from photo-discharging an electrostatically charged a-Se photoconductor film is measured and used to calculate a value for the carrier range $\mu\tau$. However, this value depends on the model used to interpret the measured potential [83, 84], and is, therefore, only an approximation to the actual value of $\mu\tau$ in the film. Furthermore, since the surface of a-Se films cannot always be charged to a high negative voltage, it is difficult to study the effects of the alloy composition on the electron range in these films.

Conventional TOF measurements can be used to study the carrier range for both electrons and holes in a-Se films. The carrier trapping time τ is typically determined in the TOF experiment by decreasing the applied bias until the carrier transit time t_T is comparable to τ. Under such conditions, the magnitude of the photocurrent decays exponentially with a time constant that represents the deep trapping time [85, 86]. However, the determination of τ from the shape of the TOF photocurrent is not reliable for several reasons. First, in a-Se alloys, photogeneration depends on the field; if the field is reduced too much the photocurrent is effectively extinguished. For films with very long lifetimes, the captured signal may become too small to reliably measure the time constant of the photocurrent decay. Secondly, the shape of the photocurrent may be affected by fractionation effects or the presence of bulk space charge, and may not exhibit a true exponential decay.

In this investigation, both TOF and IFTOF measurements were used to study the effects of the alloy composition on μ and τ. The benefit of using the IFTOF technique for carrier $\mu\tau$ studies is that it accurately measures the value of both the hole and the electron lifetimes in the bulk of the photoconductor. For this study, a number of samples with varying amounts of As (0.3 to 0.7 at. %) and Cl (0-40 wt. ppm Cl) were obtained from ANRAD Corporation. The samples were deposited at ANRAD onto glass substrates using conventional vacuum coating techniques similar to those described in Chapter 4. The glass substrates were pre-coated with a conductive layer of Indium Tin Oxide (ITO) to form the bottom electrode, and semitransparent Au contacts were sputtered onto the sample surface using the Hummer IV system as discussed in Chapter 4.

5.3.2 Results

The results for the hole experiments are presented in Figure 5.5. The hole drift mobility μ_h was unaffected by the composition of the alloy, as shown in Figure 5.5 (b) and (e). The hole lifetime τ_h, however, showed a relatively strong dependence on the alloy composition, as shown in Figure 5.5 (c) and (f). The measured value of τ_h decreased as the concentration of As was increased, and it increased as the concentration of Cl was increased. The amounts of As and Cl in the stabilized a-Se layer, therefore, have opposite effects on the hole lifetime, which is reflected in the hole range $\mu\tau_h$ as shown in Figure 5.5 (a) and (c). Furthermore, these effects compensated each other; the reduction in the hole lifetime with the addition of As can be compensated for by increasing the amount of Cl doping in the alloy composition, as shown in Figure 5.5 (a). Conversely, the gain in τ_h with the addition of Cl can be compensated for by increasing the As concentration, as shown in Figure 5.5 (d).

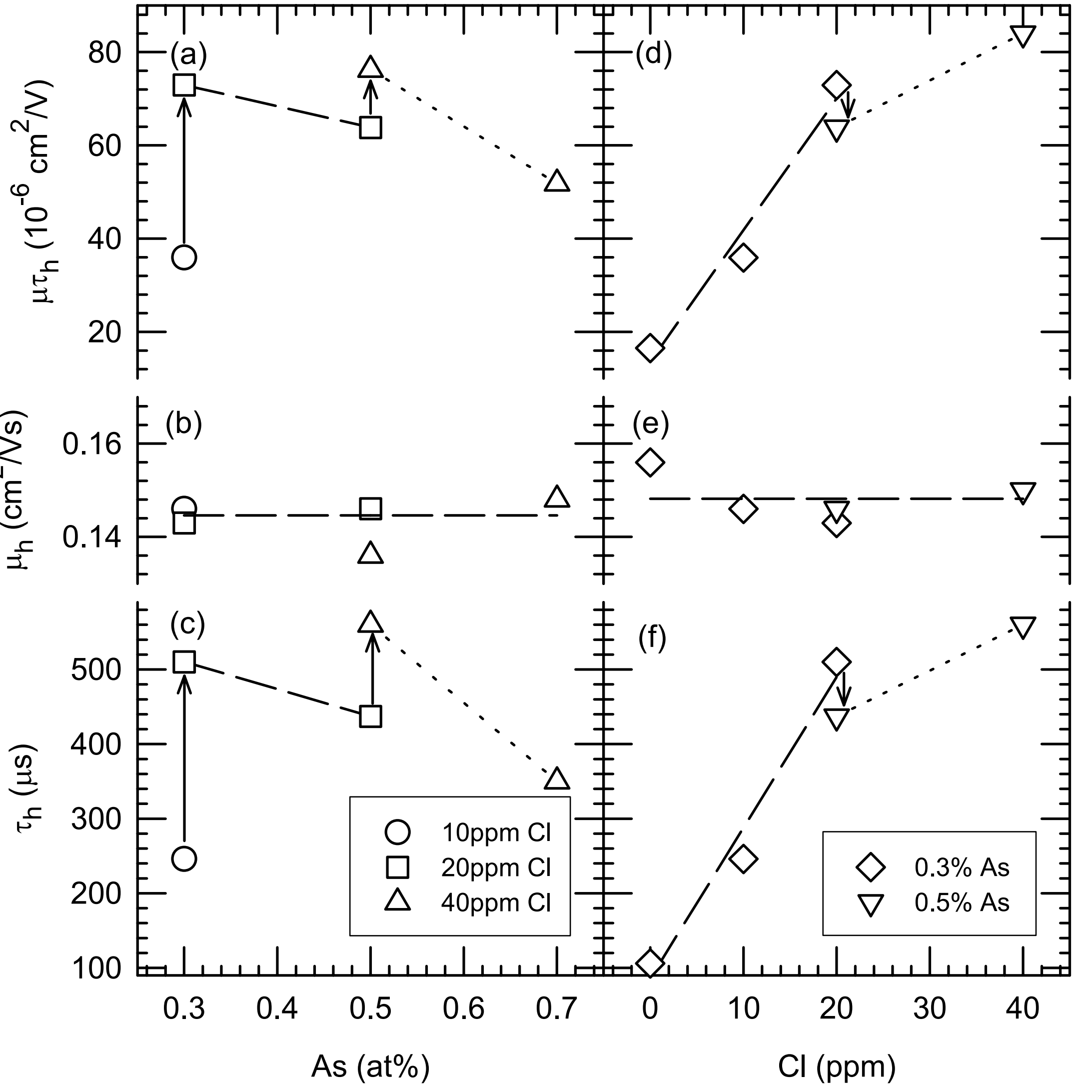

Figure 5.5 The influence of the addition of As and Cl on the hole lifetime, mobility and range in stabilized a-Se layers.

The influence of As and Cl on the electron lifetime and drift mobility in stabilized a-Se films was also investigated. The electron mobility μ_e in stabilized a-Se films exhibits a strong dependence on the magnitude of the electric field [87]. Therefore, in order to compare the values of the electron mobility measured in different films of varying thickness, the field dependence of μ_e was measured, as shown in Figure 5.6, and the values of μ_e corresponding to a nominal electric field of 4 V/µm were determined.

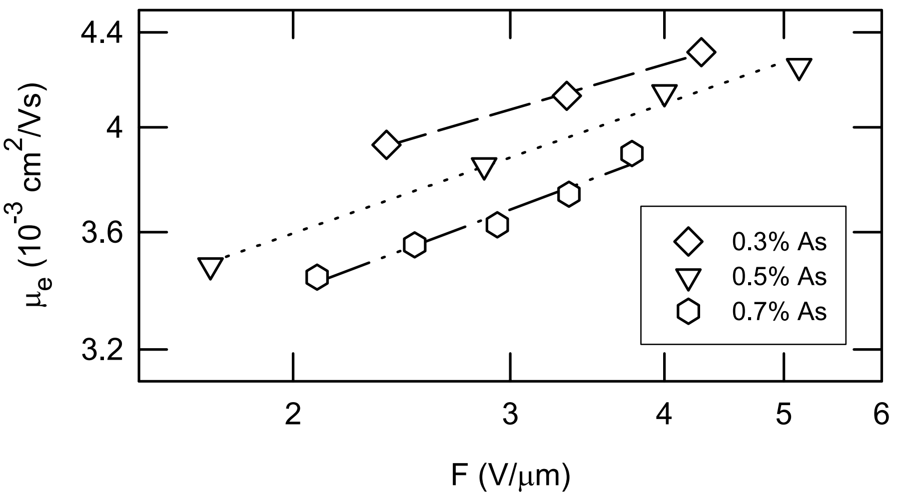

Figure 5.6 The dependence of electron mobility versus applied electric field F in a-Se:As + Cl. Note that both axes are logarithmic.

The effects of As and Cl composition on electron transport in stabilized a-Se films are shown in Figure 5.7. It is apparent that the electron lifetime τ_e dependence on the alloy composition is opposite to that observed for holes. An increase in the concentration of As increased τ_e, whereas an increase in the amount of Cl decreased τ_e. The electron mobility μ_e decreased as the concentration of As was increased; however, τ_e exhibited a stronger dependence on the concentration of As, and, therefore, the electron range $\mu\tau_e$ increased with the concentration of As. The electron mobility was not affected by Cl doping, as shown in Figure 5.7 (e).

These results are qualitatively summarized in Table 5.1. The most important technological conclusion from these experiments is that, by appropriately choosing the relative amounts of As and Cl, the hole and electron transport properties in the x-ray photoconductive layer can be controlled. Ideal photoconductor layers can be fabricated by selecting suitable alloy compositions that maximize the carrier ranges. Furthermore, knowledge of the effects of alloy composition can be used to design a-Se layers with certain transport properties. For example, “p-type” layers of a-Se can be fabricated by choosing a film composition with limited electron transport. This facilitates the design of novel a-Se structures, such as blocking layers to reduce the dark current in direct conversion x-ray photodetectors.

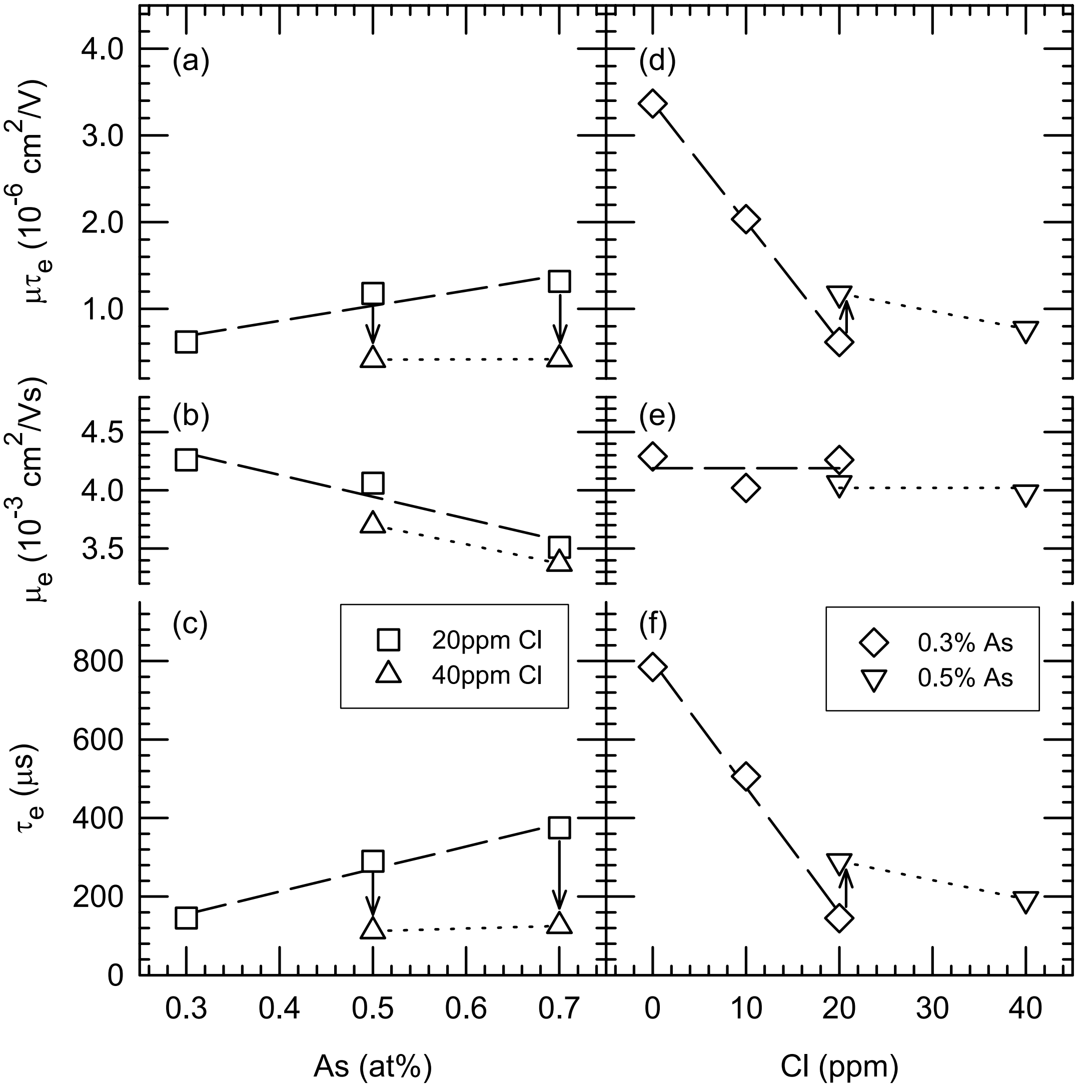

Figure 5.7 The influence of the addition of As and Cl on the electron lifetime, mobility and electron range in stabilized a-Se.

It should be noted that there is some latitude in choosing the composition of stabilized a-Se for a given $\mu\tau$ product. For example, the hole range for 20 ppm Cl doped a-Se:As$_{0.3\%}$ is about the same as that for a-Se:As$_{0.5\%}$ doped with 40 ppm Cl. Furthermore, it is interesting that only small amounts of Cl are needed to observe large changes in the properties compared with the amount of As needed for similar changes. For example, the reduction in hole lifetime induced by an increase of As concentration from 0.3 to 0.5 at. % may be compensated by the addition of only 20 ppm of Cl.

A detailed analysis of the effects of the alloy composition on the transport properties of stabilized a-Se films is beyond the scope of the present work. However, it is nonetheless speculated that under- and over-coordinated charged defects that result from the integration of As and Cl atoms into the a-Se structure play an important role. For example, the reduction in τ_h with As addition may indicate an increase in the concentration of Se_1^- type defects, which are considered to act as hole traps [88]. There have been attempts in the literature to explain the compensation mechanism between As and Cl [43], although to date there is no accepted model that can explain all of the observations.

Table 5.1 The influence of As and Cl doping on the properties of stabilized a-Se. Double arrows are used to stress the strength of the influence.

	Holes			**Electrons**		
	τ_h	μ_h	$\mu\tau_h$	τ_e	μ_e	$\mu\tau_e$
As	↓	**0**	↓	↑	↓	↑
Cl	↑↑	**0**	↑↑	↓↓	**0**	↓↓

5.4 Bulk Space Charge Effects and Recombination

Bulk space charge refers to a distribution of immobile charges occupying deep traps from a previous TOF experiment or x-ray exposure. A distribution of trapped charge in the bulk of the specimen alters the internal field in the a-Se photoconductor and may act as recombination centers for subsequent photogenerated charge, thereby decreasing the effective carrier lifetime. The presence of bulk space charge can lead to temporal imaging artifacts in a-Se based flat-panel x-ray detectors, such as a decrease in the sensitivity of the detector with x-ray exposure.

This section considers the effect of negative bulk space charge, i.e. trapped electrons, on the hole TOF and IFTOF transient photocurrent signals in stabilized a-Se photoconductive layers. An expression is developed which can be used to calculate the concentration of trapped electrons at a position in the sample using a combination of hole TOF and IFTOF measurements. This calculation can then be used to estimate the value of the capture coefficient between drifting holes and trapped electrons. The value of the capture coefficient is an important parameter for the accurate modeling of the effects of charge trapping on the performance of a-Se direct conversion x-ray image detectors.

5.4.1 Background

Recently, flat panel detectors based on self-scanned readout of a-Se using active matrix thin-film transistor (TFT) arrays have been developed and commercialized for general radiography. It has become an attractive technology because of the compact detector size, fast image readout and high x-ray sensitivity. Currently, there is some interest in studying the temporal imaging characteristics, which are known as lag and ghosting, in these types of x-ray image detectors [89]. Lag is the carry-over of image charge generated by previous x-ray exposures into subsequent image frames, and it manifests itself as image readout without an x-ray exposure. Preliminary measurements of lag in prototype a-Se flat-panel detectors for fluoroscopy show that the lag in the first frame after an x-ray exposure is less than 5% [90]. Ghosting is the change of x-ray sensitivity, or gain, of the detector as a result of previous exposures to radiation, and it can only be seen in subsequent x-ray exposures. The decrease in the x-ray sensitivity is a well known phenomenon in xeroradiography, and is often referred to as x-ray “fatigue”.

Lag and ghosting may be attributed to the presence of trapped bulk space charge in the a-Se layer from previous x-ray exposures. Stabilized a-Se films contain a significant concentration of localized hole and electron traps, which are distributed across the bulk of the film. Bulk trapping contributes to lag in fluoroscopic detectors because charge carriers trapped during the first image frame can be released and collected in subsequent frames. Bulk trapping contributes to ghosting in any x-ray detector because the trapped charge may recombine with subsequently generated image charge, thus reducing the amount of charge that is collected for a given x-ray exposure; it has been found that both trapped electrons and holes can form such recombination centers [89].

Furthermore, the trapped charge alters the electric field in the a-Se layer so that the field at one of the electrode interfaces increases; this increases the charge injection at that electrode and contributes further to lag. The non-uniform field may also result in changes in the conversion gain throughout the layer and hence affect the x-ray sensitivity.

5.4.2 Technique

The principle of the bulk space charge measurement technique is illustrated in Figure 5.8. Initially, electron trapping is induced in the sample by performing multiple electron TOF experiments as shown in Figure 5.8 (a). The TOF type experiment ensures that only electrons drift across the sample, so a distribution of negative space charge $N(x)$ will build up due to electron trapping. The polarity of the applied bias is then reversed, and a hole TOF experiment is performed to examine the effects of the trapped electron distribution on the hole drift, as shown in Figure 5.8 (b).

The trapped electron distribution will modify the electric field profile, as shown in Figure 5.8 (c), so that the average drift velocity of the photo-injected hole packet will vary on its transit across the sample thickness L. Also, the number of free holes in the packet will decrease during the transit because some will be captured by deep hole traps and some may recombine with the trapped electrons. Since $i(t)$ is proportional to both the drift velocity and the concentration of the holes in the packet, the magnitude of the captured hole photocurrent will decay with time as shown in Figure 5.8 (d).

The quantitative analysis of the effect of the trapped electrons on the hole TOF transient phorocurrent signal in Figure 5.8 (d) can be simplified by making the following assumptions. If a strongly absorbed source is used to inject holes into the sample, then the concentration of drifting holes in the packet $p(x,t)$ can be represented by a delta function with a mean hole concentration $\overline{p}(t)$ and a width $w << L$. The hole photocurrent in a-Se can be classified as non-dispersive [36], so the width of the hole packet does not change significantly as it drifts across the sample length. Furthermore, since the hole mobility in a-Se is independent of the electric field, it can be assumed that the hole packet

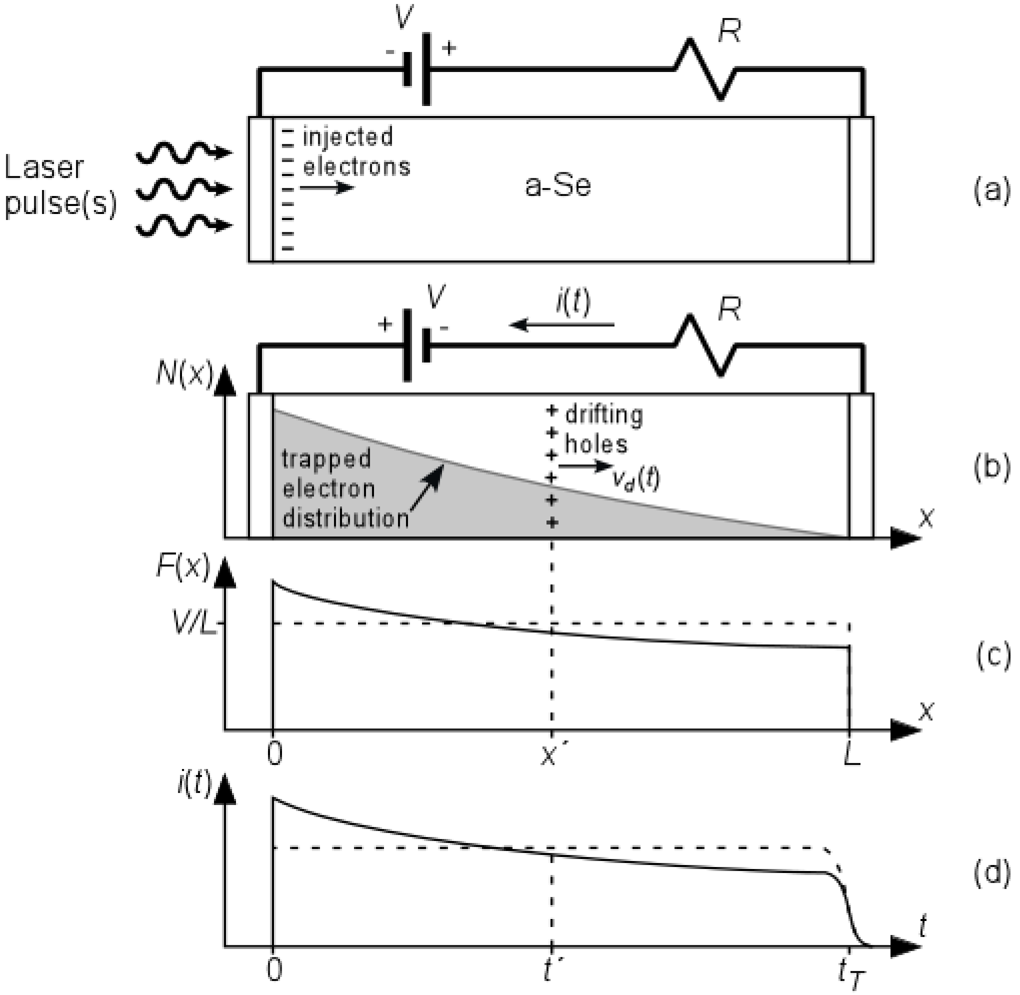

Figure 5.8 (a) An electron TOF experiment is performed one or more times so that electrons become trapped in the bulk of the sample. (b) A hole TOF experiment is performed, and the hole transient photocurrent signal *i*(*t*) is captured. (c) The distribution of trapped negative charge alters the profile of the electric field. (d) The captured hole TOF will decay due to the non-uniform field and the effects of recombination and trapping.

drifts with a constant mobility μ_h. Therefore, the drift velocity of the hole delta packet depends only on the magnitude of the electric field, i.e. $v_d(x,t) = \mu_h F(x,t)$.

Consider the hole delta packet at a position $x = x'$ in the a-Se layer as shown in Figure 5.8 (b); the instantaneous photocurrent density for the TOF experiment in the presence of the trapped negative charge distribution can be determined from Ramo's theorem [91],

$$j(t) = \frac{e\mu_h}{L}\int_0^L p(x,t)F(x,t)dx \approx \frac{ew\mu_h \overline{p}(t)}{L}F(x',t) \qquad 5.1,$$

where $F(x',t)$ is the magnitude of the electric field at the position of the hole delta packet. In time dt the packet drifts a distance dx, and the magnitude of the photocurrent decreases due to the effects of the trapped electrons. These effects may be examined by taking the time derivative of Equation 5.1 at the position of the hole packet $x = x'$, i.e.

$$\left.\frac{dj(t)}{dt}\right|_{x=x'} = \frac{ew\mu_h F(x',t)}{L}\frac{d\overline{p}(t)}{dt} + \frac{ew\mu_h \overline{p}(t)}{L}\frac{\partial F(x',t)}{\partial t} \qquad 5.2.$$

It is clear from Equation 5.2 that the rate of change in the instantaneous photocurrent density is proportional to the rate of change in the number of holes in the hole delta packet and on the profile of the electric field in the a-Se layer due to the trapped electron distribution.

The rate of change in the number of holes in the delta packet depends on the distribution of traps in the a-Se layer and on the concentration of trapped electrons at $x = x'$. In a-Se films, it can be assumed that the hole traps are distributed at a discrete level in the mobility gap with a well defined capture time τ_h. These traps are energetically deep so that the thermal release of holes can be neglected for the time it takes the delta packet to traverse the sample length. It is also assumed that free holes in the charge packet can recombine with the trapped electrons. The recombination time τ_r is inversely proportional to the concentration of trapped electrons at $x = x'$, i.e.

$$\tau_r = \frac{1}{C_r N(x')} \qquad 5.3.$$

The coefficient C_r in Equation 5.3 is the *capture coefficient* between the drifting holes and the trapped electrons. The total rate of change in the concentration of holes in the presence of deep traps and trapped electrons can be represented as,

$$\frac{d\bar{p}(t)}{dt} = -\frac{\bar{p}(t)}{\tau_h} - \frac{\bar{p}(t)}{\tau_r} \qquad 5.4.$$

The instantaneous current density also depends on the hole drift velocity and hence the magnitude of the electric field at the position of the hole delta packet. The electric field profile varies across the length of the a-Se layer due to the presence of the trapped bulk space charge *N*(*x*). The negative space charge density at the location $x = x'$ is $-eN(x')$, and the profile of the internal electric field at this location can be found from Gauss's law in point form, i.e.

$$\left.\frac{\partial F_N(x,t)}{\partial x}\right|_{x=x'} = -\frac{e}{\varepsilon}N(x') \qquad 5.5,$$

where ε is the permitivity of the a-Se layer.

The net positive charge in the hole packet also perturbs the instantaneous electric field profile as discussed in Chapter 3. The rate of change in the electric field profile at the position of the hole packet due to this perturbation can be determined by taking the derivative of either Equation 3.1 or 3.2, i.e.,

$$\left.\frac{\partial F_p(x',t)}{\partial x}\right|_{x=x'} = \frac{ew\bar{p}(t)}{\varepsilon L} \qquad 5.6.$$

The effect described by Equation 5.6 is related to the concentration of holes in the packet, and can be minimized by performing the TOF experiment under small signal conditions.

The time rate of change in the electric field at the instantaneous position of the charge packet in Equation 5.2 can be determined by multiplying the spatial variation of the electric field profile with the rate of change in the position of the hole packet. In time *dt*, the packet moves a distance *dx* and encounters a different electric field $F(x'+dx,t+dt)$. The profile of the electric field at position $x = x'$ is found by combining Equations 5.5 and 5.6. The rate of change in the position of the hole packet is simply the drift velocity,

$dx/dt = v_d(x', t) = \mu_h F(x', t)$. Therefore, the time rate of change of the electric field encountered by the drifting hole packet is,

$$\frac{dF(x',t)}{dt} = -\frac{e}{\varepsilon}\left[N(x') - \frac{w\bar{p}(t)}{L}\right]\mu_h F(x',t) \qquad 5.7.$$

Equations 5.4 and 5.7 can be substituted into Equation 5.2, and the resulting expression rearranged in terms of the ratio of the photocurrent density to its time derivative is

$$\frac{1}{j(t')}\frac{dj(t')}{dt} \equiv \frac{j'(t')}{j(t')} = -\frac{1}{\tau_h} - \frac{1}{\tau_r} - \frac{e\mu_h}{\varepsilon}\left[N(x') - \frac{\bar{p}(t')w}{L}\right] \qquad 5.8.$$

The ratio $j'(t')/j(t')$ can readily be evaluated at the time $t = t'$ on the TOF photocurrent signal, and the effective hole lifetime τ_{eff} due to the trapping and recombination of holes can be measured by performing an IFTOF experiment at a location that corresponds to the same time $t = t'$. The recombination time τ_r between the drifting holes and the trapped electrons is then determined by noting that

$$\frac{1}{\tau_{eff}} = \frac{1}{\tau_h} + \frac{1}{\tau_r} \qquad 5.9,$$

where τ_h is the deep trapping time for holes. Therefore, by performing both a hole TOF and a hole IFTOF experiment, the concentration of trapped electrons at a position in the film may be determined from Equation 5.8.

In order to apply the bulk space charge measurement technique to a-Se films, a sequence of TOF-IFTOF-TOF experiments was performed as shown in Figure 5.9. The first experiment, shown in Figure 5.9 (a), is a hole TOF measurement that captures the shape of the transient photocurrent $j_1(t)$, and the ratio of the photocurrent j_1 to its time derivative $j_1'(t') = dj_1/dt$ at a point $t = t'$ is determined. The second experiment, shown in Figure 5.9 (b), is a hole IFTOF measurement that measures the effective hole lifetime, i.e.,

$$\tau_{eff} \approx -t_i / \ln\left(j_2(t'+t_i)/j_2(t')\right) \qquad 5.10,$$

at the same point $t = t'$. The inherent hole trapping time τ_h is known from initial IFTOF measurements, thus the recombination lifetime τ_r can be determined using Equation 5.9. The third and final experiment is another hole TOF measurement that captures the shape of the transient photocurrent $j_3(t)$ as in Figure 5.9 (c). The ratio of the actual photocurrent j_3 to its time derivative $j_3'(t') = dj_3/dt$ is again evaluated at point $t = t'$. Three experiments are carried out because the trapped electron concentration is slightly modified in each experiment due to recombination with the injected holes.

The thermal release of electrons from deep traps is not expected to occur during the experiment. Electron traps are distributed at an energy deep in the mobility gap of a-Se (~ 1.0 eV below E_c). This implies a release time for trapped electrons of at least a few hours. The sequence of TOF-IFTOF-TOF experiments may be performed in a matter of seconds; therefore, it can be assumed that there will be a negligible change in the trapped negative charge distribution due to thermal release over the time scale of the experiments.

The time point $t = t'$ on the TOF waveforms corresponds to the interruption

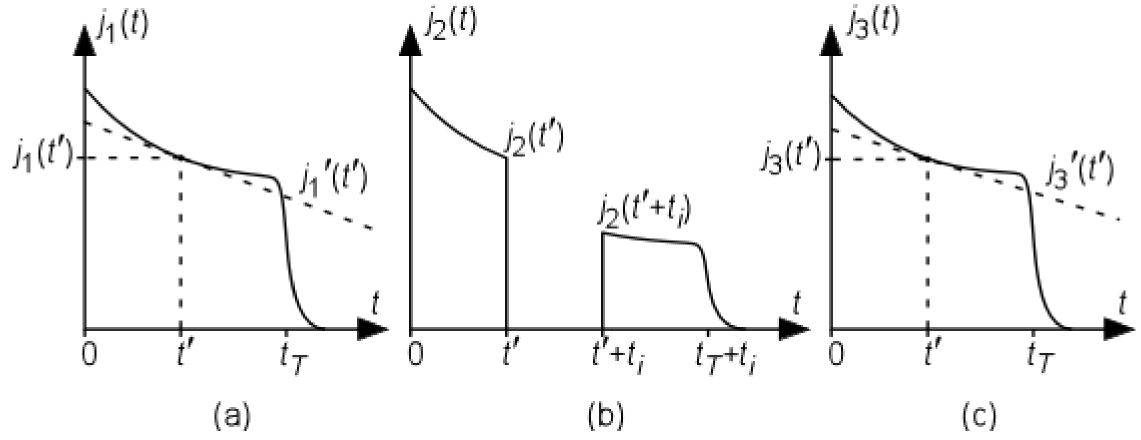

Figure 5.9 The technique for calculating the recombination coefficient is based on carrying out three successive experiments. (a) The first, a TOF experiment, probes the profile of negative space charge in the sample. (b) The second, an IFTOF experiment, measures the recombination time τ_r. (c) The third, a TOF experiment, again probes the profile of negative space charge in the sample. The third experiment ensures that any change in the number of negative charge centers is accounted for in the final calculation.

location $x = x'$ of the hole packet during the IFTOF experiment. If N_1 is the initial trapped electron concentration and p_1 is the concentration of holes at this position, then Equation 5.8 can be applied to the first hole TOF experiment by setting $N(x') = N_1$ and $\overline{p}(t') = p_1$. Similarly, Equation 5.8 can be applied to the final TOF experiment by setting $N(x') = N_3$ and $\overline{p}(t') = p_3$, where N_3 is the trapped electron concentration and p_3 is the hole concentration in the final TOF experiment. The recombination lifetime measured in the IFTOF experiment is related to the electron concentration N_2. The change in the trapped electron concentration between successive TOF experiments is assumed to be small, so that $N_2 \approx (N_1 + N_3)/2$. Therefore, by applying Equation 5.8 to the first and third experiments, adding them up and using the latter arguments, the concentration of trapped electrons N_2 can be determined from the TOF-IFTOF-TOF experiment sequence shown in Figure 5.9 from the following expression;

$$N_2 = \frac{\varepsilon}{\mu_h e}\left(-\frac{1}{\tau_h} - \frac{1}{\tau_r} - \frac{1}{2}\left(\frac{j_1'}{j_1} + \frac{j_3'}{j_3} \right) + \frac{1}{2}\left(\frac{j_1}{F_1} + \frac{j_3}{F_3} \right) \right) \qquad 5.11.$$

Alternatively, Equation 5.11 can be rearranged in terms of the capture coefficient between trapped electrons and drifting holes by noting that $N_2 = (C_r \tau_r)^{-1}$, i.e.,

$$C_r = \frac{e\mu_h / \varepsilon}{-1 - \frac{\tau_r}{\tau_h} - \frac{\tau_r}{2}\left(\frac{j_1'}{j_1} + \frac{j_3'}{j_3} \right) + \frac{\tau_r}{2\varepsilon}\left(\frac{j_1}{F_1} + \frac{j_3}{F_3} \right)} \qquad 5.12.$$

In Equations 5.11 and 5.12, the terms F_1 and F_3 are the magnitudes of the electric field in the first and final TOF experiments at the position of the hole packet. It is assumed that these values can be approximated by the nominal value $F_1 = F_3 \approx V/L$, where V is the magnitude of the applied bias.

5.4.3 Results

The bulk space charge measurement technique was applied to four samples of stabilized Se:As$_{0.5\%}$ doped with varying amounts of Cl (5-40ppm). The samples were prepared for transient photoconductivity experiments following the procedures outlined

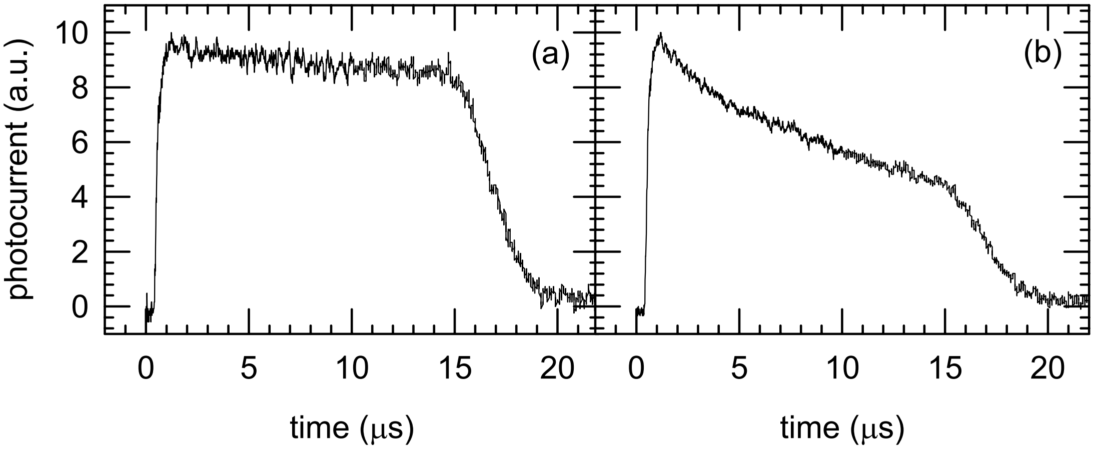

Figure 5.10 (a) A typical TOF photocurrent signal in a 103 μm thick, well-rested sample of a-Se:As$_{0.5\%}$ +10ppm Cl. (b) A TOF signal in the same sample showing the effects of purposefully trapped negative charge in the bulk of the sample. Small signal conditions were used during the TOF experiments.

in Chapter 3, and their transport properties were characterized by performing conventional TOF and IFTOF experiments prior to commencing the bulk space charge experiments; Figure 5.10 (a) shows a typical hole TOF waveform captured in a well rested sample. The results of the conventional hole TOF and IFTOF measurements are summarized in Table 5.2. The locations of the interruption x'/L in the initial IFTOF experiments is also indicated in the table. The same locations were used for the intermediate hole IFTOF measurements during the bulk space charge measurement experiments.

Prior to beginning the bulk space charge measurement, the samples were initially rested, in the dark with the electrodes shorted together, for a period of at least 24 hours to ensure that there was negligible bulk space charge in the sample at the beginning of the experiment. Trapped electrons were then introduced into the bulk of the sample by carrying out repetitive electron TOF experiments as described above. The polarity of the applied bias was reversed, and a hole TOF experiment was captured. The effects of the trapped electrons on the hole TOF signal can be clearly seen in Figure 5.10 (b); the hole photocurrent decays as expected due to the distribution of trapped electrons in the sample. Subsequent hole IFTOF and TOF experiments were then performed, and the concentration of trapped electrons at a position in the sample was calculated using Equation 5.11.

Table 5.2 The thickness, Cl doping, and inherent hole transport properties of the samples used in this investigation. The bulk space charge measurements were performed at a location in the sample identified by x'/L. The results of these measurements were used to calculate the average recombination coefficient C_r for each sample.

Sample	L (μm)	Cl (ppm)	μ_h (cm^2/Vs)	x'/L	τ_h (μs)	C_r (cm^3/s)
1	103	10	0.13	0.45	60.0	3.68×10^{-8}
				0.50	58.6	3.41×10^{-8}
2	102	5	0.13	0.55	83.9	3.97×10^{-8}
3	95	10	0.13	0.51	77.4	3.96×10^{-8}
4	75	40	0.12	0.51	90.3	3.15×10^{-8}

This process was repeated several times with each sample for varying amounts of electron trapping. The relative amount of electron trapping in a particular experiment could be controlled by varying the number of times that the electron TOF experiment was repeated; increasing the number of repetitions leads to an increase in the trapped electron concentration. The results are presented in Figure 5.11, which shows the relationship between the calculated electron concentration N_2 at x' and the hole recombination lifetime τ_r measured in the intermediate IFTOF experiments for all of the samples in this investigation. Note that the bulk space charge measurement was performed in two locations in Sample 1.

The relationship between the trapped electron concentration and the hole recombination lifetime is important as it defines the capture process between the drifting holes and the trapped electrons, i.e. $N_2 = (C_r \tau_r)^{-1}$, where C_r is the recombination coefficient. It is clear from Figure 5.11 that this process is the same for all of the samples studied in this investigation, as the relationship between N_2 and τ_r^{-1} is linear within experimental errors. Furthermore, this relationship passes through the origin, which is expected since the probability of recombination between a drifting hole and a trapped

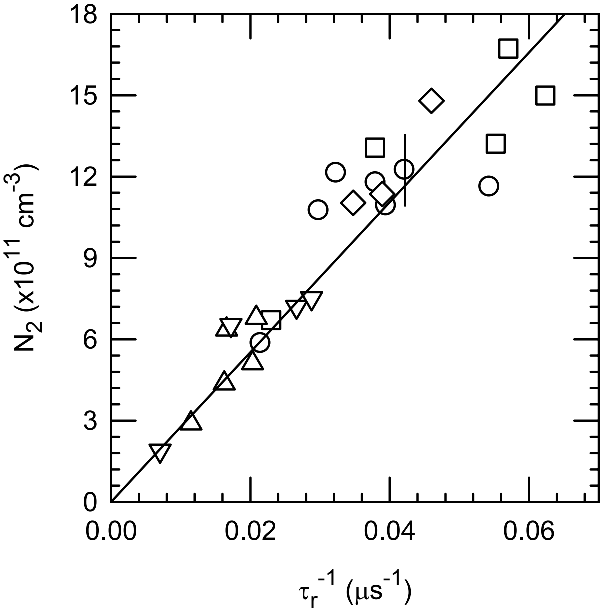

Figure 5.11 The results of bulk space charge measurements performed on various samples of stabilized a-Se$_{0.5\%}$. The calculated trapped electron concentration at x' is plotted against the inverse of the measured hole recombination lifetime: (○) Sample 1 at x'= 46.4μm, (□) Sample 1 at x'= 51.5μm, (△) Sample 2 at x'= 56.1μm, (▽) Sample 3 at x'= 48.5μm, and (◇) Sample 4 at x'= 38.3μm. The line represents the expected relationship between N_2 and τ_r^{-1} as defined by the Langevin recombination coefficient C_L.

electron approaches zero if there are no trapped electrons in the sample. The recombination coefficient $C_r=(\tau_r N_2)^{-1}$ was calculated from the data, and the average value for each sample is presented in Table 5.2.

Previously, double photoexcitation measurements in a-Se photoconductive layers have shown that the recombination between drifting (free) holes and drifting (free) electrons is described by a Langevin process [92], where the rate of recombination is proportional to the concentration of drifting holes p and drifting electrons n, i.e.

$$\frac{dp}{dt} = -C_L pn \qquad 5.13.$$

The constant of proportionality C_L in Equation 5.13 is defined as the Langevin coefficient, and is related to the effective drift mobilities of the carriers, i.e.

$$C_L = \frac{e}{\varepsilon}(\mu_h + \mu_e) \qquad 5.14,$$

where μ_h is the effective hole drift mobility and μ_e is the effective electron drift mobility.

It is reasonable to assume that the recombination between free holes and trapped electrons follows a similar relationship in a-Se layers. In this case, the Langevin coefficient would be determined by setting $\mu_e = 0$ since the electrons are trapped (immobile). The expected Langevin coefficient for the a-Se layers in this investigation can be calculated by noting that the average effective hole drift mobility from Table 5.2 is 0.128 cm^2/Vs and that the relative permitivity ε_r of a-Se is 6.2. Therefore, the expected Langevin recombination coefficient is $C_L=3.73\times10^{-8}$ cm^3/s. This represents the maximum recombination coefficient one would expect between a drifting hole and a trapped electron in a-Se. This value is compared to the experimental data by plotting $N_2 = (C_L \tau_r)^{-1}$ as a line in Figure 5.11. It is clear that the experimental data agrees quite nicely with the theoretical expected relationship.

The average recombination coefficient determined from the data in Figure 5.11 is $C_r=(3.63\pm0.35)\times10^{-8}$ cm^3/s. Since the measured recombination coefficient C_r is the same as the Langevin coefficient C_L, i.e. $C_r \approx C_L$, it is concluded that drifting holes holes are recombining with the trapped electrons that were introduced into the bulk of the sample by performing repetitive electron TOF experiments. Furthermore, the recombination with the trapped electrons can be described by a Langevin process, which implies that a free hole drifts diffusively with a short mean-free-path and experiences a Coulombic capture field from a trapped electron. The rate of recombination is then proportional to the concentrations of the photoinjected holes and trapped electrons, i.e.,

$$\frac{dp}{dt} = -C_L p N_2 = -\frac{p}{\tau_r} \qquad 5.15.$$

These results may be used to suitably model the effect of trapped electrons on the performance of a-Se based direct conversion x-ray image detectors.

5.5 X-ray Induced Trapping and Recombination

As discussed previously, the sensitivity of a-Se based flat panel x-ray detectors decreases with exposure to x-ray radiation. This phenomenon is called ghosting, and it may be attributed to the presence of either trapped bulk space charge or x-ray induced structural defects. Trapped charge from previous x-ray exposures alters the internal electric field and acts as recombination centers for subsequent photogenerated carriers, which effectively reduces the carrier lifetime. X-ray induced structural defects, such as a negatively charged coordination defect Se_1^-, increase the concentration of deep traps and reduce the deep trapping time of the carriers. Both effects would result in a decrease in the x-ray sensitivity of the detector because the amount of collected charge for a given x-ray exposure is reduced. In this section, the results of a systematic study of the effects of x-ray exposure on the charge transport properties in stabilized a-Se photoconductive layers are presented.

5.5.1 Results

The effects of x-ray exposure on the transport properties of stabilized amorphous selenium were initially investigated in a 95 μm thick sample of a-Se:$\mathrm{As}_{0.5\%}$ + 10 ppm Cl. For this portion of the investigation, the controls on the Gendex DX-1000 x-ray unit were set to 50 $\mathrm{kV_p}$ and 10 mA, and aluminum (Al) filters with a total thickness of 5.5 mm were placed between the source and the sample. The timing control of the x-ray unit was set to produce a one second long series of x-ray impulses; each one second burst resulted in an average x-ray exposure of ~0.008R. The unit was allowed to cool for a period of one minute following each x-ray exposure to prevent the x-ray tube anode from overheating. An IFTOF measurement was performed following every fifth x-ray exposure to examine the cumulative effects of x-ray exposure on the carrier lifetimes. After the final exposure, the sample electrodes were short circuited, and the sample was rested in the dark at room temperature. Several IFTOF measurements were performed periodically during the rest period to examine the recovery of the carrier lifetimes.

The hole and electron drift mobilites were measured to be 0.13cm^{2}V^{-1}s^{-1} and 3.0×10^{-3}cm^{2}V^{-1}s^{-1} respectively prior to x-ray exposure, and these values did not change after an x-ray exposure of 0.48R (holes) and 1.0R (electrons). Exposure to 0.48R caused the hole lifetime to decrease from an initial value of 50μs to 27μs. Since the rate of deep trapping is proportional to the number of capture centers N_t, the change in the inverse of the lifetime is a measure of the increase in N_t provided that the capture cross-sections are not affected by the x-rays, i.e.,

$$\Delta N_t \propto \frac{1}{\tau} - \frac{1}{\tau_0} \qquad 5.16,$$

where τ_0 and τ are the lifetimes before and after exposure respectively. Figure 5.12 shows that the x-ray induced hole capture centers increased linearly with x-ray exposure. In contrast, the electron lifetime was not affected by exposures of up to 1 R as shown in Figure 5.13.

The hole lifetime slowly recovered to its initial value in the period following the x-ray exposure. The decay in the number of induced capture centers calculated from Equation 5.16 was exponential in time with a time constant of 5±1×10^4 s as shown in Figure 5.14. The time constant was the same within error for initial exposures of 0.48R and 0.24R, and a qualitatively similar decay was observed for an initial exposure of 0.08R. Note that the calculated value for N_t has larger relative error as the lifetime approaches the pre-exposure value.

These results suggest that electrons captured into localized gap states are in turn acting as recombination centers for holes. The electron schubweg $\mu\tau F$ is 310μm for the field of 5.5V/μm applied during irradiation. Since the sample is 95μm thick, most of the x-ray generated electrons are swept from the sample, but about 14% will be trapped. The number of trapped electrons should increase linearly with exposure as observed. As the electrons are thermally excited out of the deep states the number of hole traps decreases and the hole lifetime recovers. The observed decay time constant for the induced traps should then be related to the trap depth E_t by $\nu_o^{-1}\exp(E_t/kT)$ where ν_o is the phonon

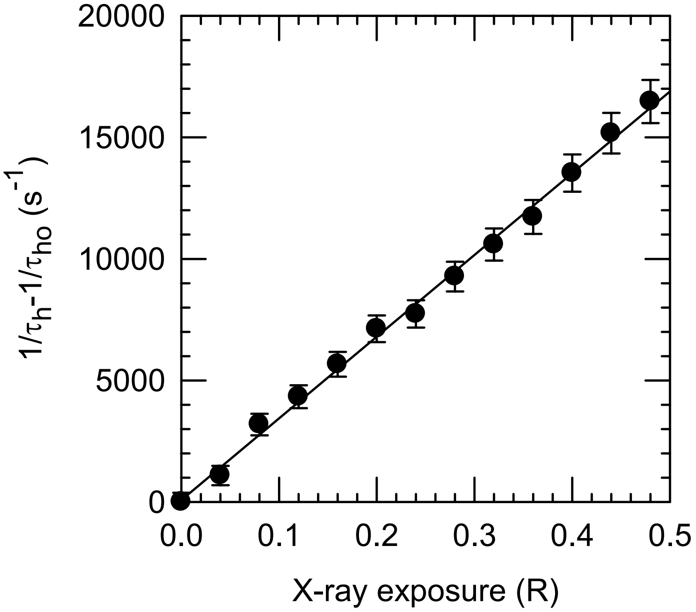

Figure 5.12 The hole lifetime in a 95μm layer of a-Se:$As_{0.5\%}$ + 10ppm Cl decreases with x-ray exposure. The difference between the inverse effective lifetime and the initial inverse lifetime is plotted as this is proportional to the number of hole capture centers induced by the x-ray exposure. The line is a linear fit to the data.

frequency, typically ~$10^{12}s^{-1}$. The measured time constant of 5×10^4s corresponds to the release of trapped charge from a trap depth of 0.96eV, which is near the center of the gap for a-Se and close to the accepted trap level for electrons. In contrast, the schubweg for holes is 3500μm resulting in only 1% being trapped. Comparatively few holes are captured and thus there is no change in the number of electron traps or the electron lifetime.

In the second stage of this investigation, the capture coefficient between x-ray induced hole capture centers and drifting holes was measured using the technique developed Section 5.4.2. If the x-ray induced hole capture centers are indeed trapped electrons, then one would expect that the capture coefficient measured using this technique would be similar to the Langevin recombination coefficient that was measured in Section 5.4.3. Once the value of the capture coefficient is known, it is possible to calculate the absolute concentration of trapped electrons at a given position in the sample as a function of x-ray exposure.

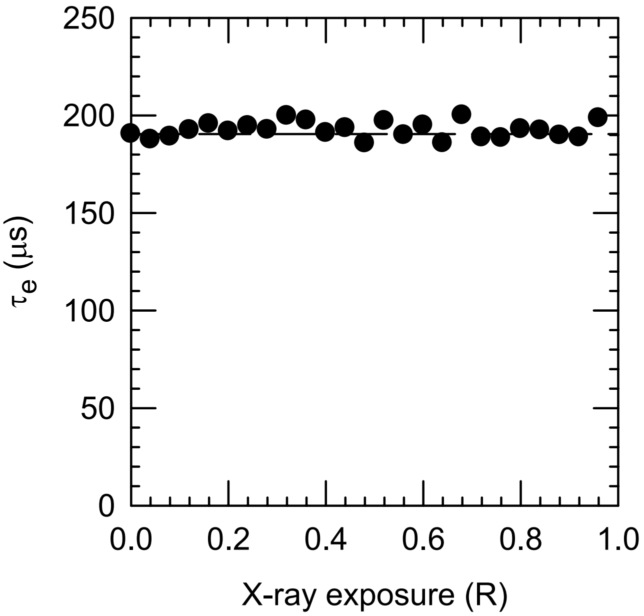

Figure 5.13 The electron lifetime in a 95μm layer of a-Se:As$_{0.5\%}$ + 10ppm Cl as a function of x-ray exposure.

The capture coefficient was measured in a 102 μm layer of a-Se:As$_{0.5\%}$ + 5ppm Cl deposited onto an aluminum substrate. The values of the charge carrier transport parameters were initially measured using TOF and IFTOF experiments prior to x-ray exposure. The hole drift mobility and deep trapping time were determined to be 0.13 $cm^2V^{-1}s^{-1}$ and 84 μs, respectively. The electron dirft mobility and deep trapping lifetime were determined to be 2.5×10^{-3} $cm^2V^{-1}s^{-1}$ and 530 μs, respectively. The Gendex DX-1000 dental x-ray unit was set to 70 kVp and 10 mA, and Al filters with a total thickness of 2.5 mm were placed between the source and the sample. The timing control on the unit was set to produce a burst of 24 x-ray impulses, which resulted in an average exposure of 0.036R per x-ray burst. A sequence of TOF-IFTOF-TOF experiments was performed after each x-ray exposure to measure the capture coefficient, and the process was repeated for a total exposure of 0.36 R.

A positive bias of 0.98V/mm was applied to the sample during each x-ray exposure. Care was taken to select a proper voltage bias to ensure that there was sufficient electron trapping and negligible hole trapping during the exposure. X-rays, unlike the laser light used to photoinject charge in the TOF experiment, generate charge

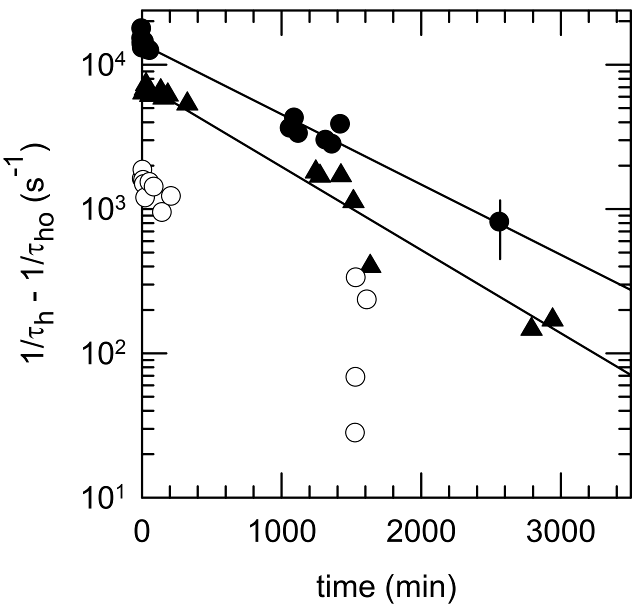

Figure 5.14 The recovery of the hole lifetime after x-ray exposure. The same quantity is plotted as in Figure 5.12. The x-ray exposures were: closed circle 0.48 R, triangle 0.24 R, and open circle 0.08 R. The lines are exponential fits to the data.

throughout the bulk of the sample. Therefore, it cannot be implicitly assumed that only electrons occupy deep trap states in the sample following x-ray exposure as holes may also become trapped. Furthermore, the bias was applied only during the x-ray exposure to minimize the amount of charge injected by the electrodes.

The amount of charge deposited in the sample due to trapping during the x-ray exposure can be qualitatively determined by analyzing the carrier schubwegs $\mu\tau F$, as this value determines the average distance that an x-ray generated charge carrier will travel in the sample before becoming trapped. A positive bias of 0.98V/μm applied to the L=102μm sample during the x-ray exposure results in $\mu\tau F_h$=1070.2μm for holes and $\mu\tau F_e$=129.9μm for electrons. Since $\mu\tau F_h >> L$, it can be assumed that there is negligible deep trapping of holes during the x-ray exposure. However, since $\mu\tau F_e \sim L$, there should be significant trapping of electrons. For the subsequent analysis, it is assumed that there were only trapped electrons in the bulk of the sample due to the x-ray exposure.

Figure 5.15 (a) and (b) show the conventional TOF photocurrent waveforms before and after a 0.29 R exposure to x-rays. There is a clear decay in the hole TOF photocurrent captured after x-ray exposure, which is similar to the effect observed Section 5.4.3. Similar results have been reported by Schiebel *et al.* [93] for xerographic TOF measurements on x-ray irradiated xeroradiographic a-Se plates, where the decay was attributed to the recombination of drifting holes with trapped electrons. This same interpretation has also been used to explain x-ray induced fatigue in a-Se xeroradiographic plates [94]. Figure 5.15 (c) and (d) show the IFTOF experiments carried out before and after an x-ray exposure of 0.29R. The location of the photocurrent interruption was $x' \approx 0.42L$, and the interruption time was 10μs. Comparison of the fractional recovered photocurrents before and after x-ray exposure clearly indicates that the effective hole lifetime is reduced due to the x-ray exposure.

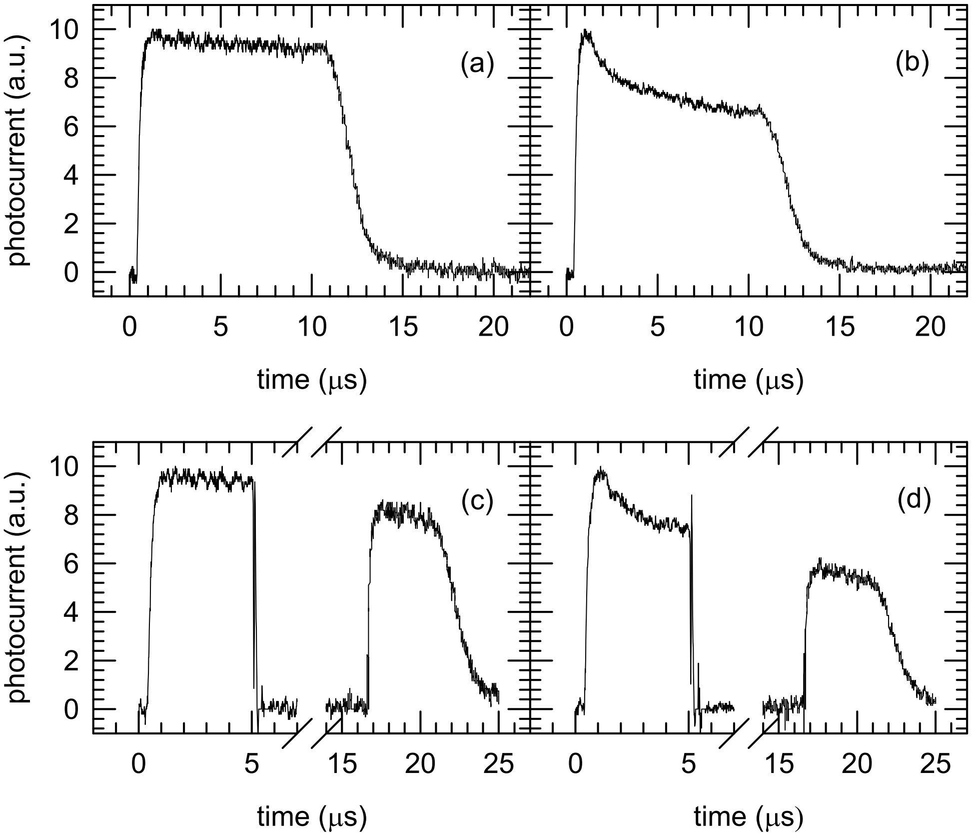

Figure 5.15 (a) TOF signal before x-ray radiation and (b) after an x-ray exposure of 0.29 R. (c) IFTOF signal before x-ray radiation and (d) after an x-ray exposure of 0.29 R. Interruption time used in the IFTOF experiments was 10 μs. A field of 0.98 V/μm was applied during x-ray exposure.

A sequence of TOF-IFTOF-TOF experiments were performed following each x-ray exposure, and the recombination coefficient C_r was calculated using Equation 5.12. The results are presented in Figure 5.16 where C_r has been normalized to the value of the Langevin coefficient $C_L = e\mu_h/\varepsilon$. The value of C_r/C_L does not change significantly with an exposure of 0.36R, which suggest that the capture process between the drifting holes and the x-ray induced capture centers is unaffected with exposure to x-rays. The average value of the data plotted in Figure 5.15 is 0.92, and the standard deviation σ is 0.15. Since $C_r \approx C_L$, it can be assumed that the interaction between the drifting holes and the x-ray induced capture centers follows a Langevin type mechanism. The mean value of the calculated capture coefficient is C_r=(3.41±0.2)×10^{-8} cm^3/s.

Once the value of C_r has been determined, it is relatively simple to calculate the concentration of x-ray induced negative capture centers N, since $N = 1/C_r\tau_r$. This value calculated for N represents the effective concentration of negative capture centers (electrons) at the location of the hole interruption from the intermediate IFTOF experiment. Figure 5.17 shows the dependence of the concentration of the x-ray induced negative centers as a function of x-ray exposure. It is apparent that, as expected, N depends linearly on the x-ray exposure. Note that Figure 5.17 is similar to Figure 5.12; however, in the previous measurement the absolute concentration of capture centers could not be calculated because the capture coefficient was not known. These results confirm the tentative arguments made previously that the decrease in the hole lifetime upon exposure is due to the creation of negative centers that are probably trapped electrons.

It should be mentioned that there are various potential sources of error that contribute to the determination of C_r in irradiated samples of a-Se by the sequence of TOF-IFTOF-TOF experiments. Firstly, it was assumed that there were no trapped holes in the bulk as a result of exposure to x-rays. This was accomplished by choosing the applied field such that there is negligible hole trapping, and it is borne out experimentally since the electron lifetime does not change with exposure to x-rays. Further, the technique to measure C_r assumes that there is no release of trapped electrons during the

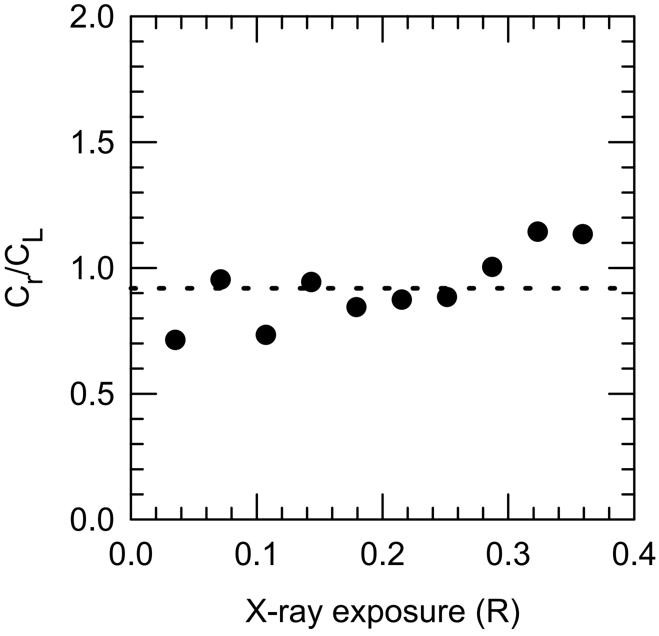

Figure 5.16 The capture coefficient C_r determined from TOF-IFTOF-TOF experiments is normalized to the value of the Langevin recombination coefficient C_L and plotted as a function of x-ray exposure. The mean value $\overline{C_r/C_L} = 0.92$ is plotted as the dashed line.

TOF-IFTOF-TOF sequence. This assumption is valid over the time scale of the experiment inasmuch as electron traps are located ~1.0eV below E_c in the mobility gap, which implies a release time for electrons of a few hours or longer. The main error in the calculation of C_r is in the differentiation of the TOF signal since any noise in the signal will be amplified by the derivative calculation. This error was minimized by choosing suitable line fitting and smoothing algorithms when analyzing the data.

Given the experimental errors, it is concluded that the capture of holes by x-ray induced capture centers is represented by a Langevin mechanism since $C_r \approx C_L$. It can further be concluded that these centers are trapped electrons as opposed to x-ray induced charged structural defects such as Se_1^-. Using this information, the hole capture process in a-Se x-ray detectors can be suitably modeled in order to predict the detector performance.

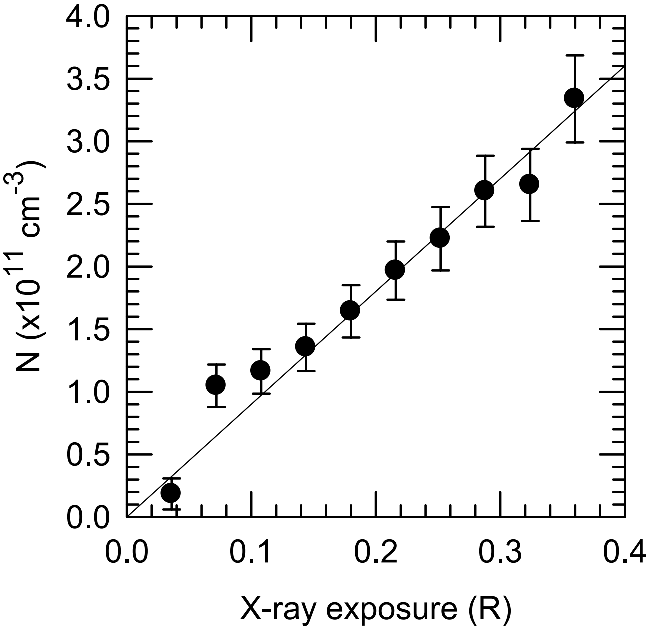

Figure 5.17 Concentration of x-ray induced negative centers at position x ≈ 0.42*L* as a function of the x-ray exposure.

5.6 Summary

This chapter presented the results of the various TOF and IFTOF measurements performed throughout the course of this project. The TOF and IFTOF techniques were successfully applied to the measurement of the carrier mobility and trapping time in samples of stabilized a-Se. The results of these measurements were used to the study the compositional effects of a-Se alloys on the carrier ranges in x-ray photoconductor films. It was found that the hole range decreased with As content, and increased with Cl content. The electron range, on the other hand, increased with As content and decreased with Cl content. These observations can be used to select suitable alloy compositions for the fabrication of stabilized a-Se x-ray photoconductive layers.

Next, the effect of bulk space charge on the transport properties in stabilized a-Se layers was examined. Negative bulk space charge alters the electric field in the a-Se layer and acts as capture centers for drifting holes. It was shown that a sequence of TOF-IFTOF-TOF measurements could be used to measure the capture coefficient between drifting holes and the negatively charged hole capture centers. This technique was applied to various samples of stabilized a-Se that contained a distribution of trapped electrons; trapped electrons were induced by initially performing repetitive electron TOF experiments. The measured capture coefficients corresponded to the Langevin recombination coefficient, which indicates that the drifting holes are recombining with the trapped electrons through a Langevin recombination mechanism.

The effect of x-ray exposure on the charge transport properties in stabilized a-Se layers was also investigated. It was found that only the hole lifetime is affected by exposure to x-ray radiation. The reduction in the measured hole lifetime with x-ray exposure corresponded to a linear increase in the number of x-ray induced capture centers in the sample. Following exposure, the number of hole capture centers decreased with a time constant that was equal the rate of release of electrons from mid-gap traps. Therefore, it was suggested that the temporary decrease in the measured hole lifetime could be attributed to the presence of x-ray induced recombination centers such as trapped electrons.

In order to verify this hypothesis, the TOF-IFTOF-TOF technique was applied to an irradiated sample of stabilized a-Se, and the capture coefficient between the drifting holes and the x-ray induced capture centers was measured as a function of x-ray exposure. It was observed that the measured capture coefficient was independent of x-ray exposure and equal to the Langevin recombination coefficient. Furthermore, the number of x-ray induced capture centers calculated using the measured value of the capture coefficient increased linearly with x-ray exposure. These results indicate that the x-ray induced decrease in the effective hole lifetime may be attributed to the presence of trapped electrons from previous x-ray exposures. Furthermore, the capture process between the drifting holes and the trapped electrons may be described by a Langevin mechanism. Knowledge of the recombination kinetics in irradiate a-Se layers is important, as these results may be used to accurately model the performance of a-Se based direct conversion x-ray image detectors.

6. SUMMARY AND CONCLUSIONS

Radiography is an important diagnostic tool that still relies on the cumbersome analog process of recording images on photographic films. A promising development for the realization of digital radiography is the concept of a flat-panel x-ray image detector. Such a detector consists of a direct conversion photoconductor coated onto the surface of a large-area thin-film transistor active-matrix array (AMA). Incident x-ray photons generate an electronic response in the photoconductor, which is converted into a digital image by the AMA. The detector is self-scanning, and the resulting image can be displayed almost immediately on a video monitor. Alloys of a-Se are an attractive x-ray photoconductor for medical imaging applications because large-area, uniform layers may be economically fabricated using conventional vacuum deposition techniques without damaging the AMA electronics.

One of the objectives of this work was to develop and utilize a system capable of performing time-of-flight (TOF) and interrupted field time-of-flight (IFTOF) transient photoconductivity experiments to measure the charge carrier mobility μ and trapping time τ in stabilized a-Se photoconductive layers. These are important electronic properties inasmuch as the $\mu\tau$ product is related to the x-ray sensitivity of the detector. TOF is well established as an experimental method for determining the charge carrier mobilities in a-Se and its alloys. IFTOF accurately measures the value of τ at a position in the bulk of amorphous semiconductor films; however, it has not been widely implemented for the characterization of stabilized a-Se alloys because of the difficulties associated with switching the large voltages ($\leq$ 1kV) required to bias these materials for transient photoconductivity measurements.

A system capable of performing both TOF and IFTOF transient photoconductivity measurements was successfully designed and built. This system was based on a grounded bridge network, a nulling capacitor, and four high-speed rectifiers to eliminate the large displacement current signals that result from switching the high voltage bias. A high-speed difference amplifier detects and amplifies the desired photocurrent signal. These experiments were applied to a range of a-Se alloy photoreceptors of various compositions as part of a number of investigations:

1. to measure the inherent charge transport properties,
2. to measure the effects of alloy composition on the carrier $\mu\tau$ product,
3. to examine the effects of negative bulk space charge, and
4. to examine the effects of x-ray exposure on the transport properties.

The conclusions from these investigations are outlined in the subsequent sections.

6.1 Charge Carrier Transport in Stabilized a-Se

TOF and IFTOF transient photoconductivity techniques were used to measure the inherent charge transport properties of stabilized a-Se photoconductive layers. The carrier drift mobility is determined by measuring the transit time from the TOF I-mode transient signal that results from the photoinjection of charge carriers into the sample. Two methods were presented for the determination of the transit time: the half peak method, and the inflection method. Both methods produce similar results for the drift mobility of holes and electrons; however, the half peak method is computationally simpler to perform. The hole and electron drift mobilites in a 224μm sample of a-Se:As0.2% were determined to be $0.14\text{cm}^2\text{V}^{-1}\text{s}^{-1}$ and $4.3\times10^{-3}\text{cm}^2\text{V}^{-1}\text{s}^{-1}$ respectively based on using the half peak method to evaluate the transit time from the TOF waveform.

The charge carrier trapping time is determined by temporarily interrupting the drift of the charge carriers by removing the applied field. The fractional change in the photocurrent before and after the field interruption is related to the number of carriers lost due to trapping at the interruption position. IFTOF measurements were performed on a 224μm sample of a-$\text{Se}_{0.2\%}$ at an interruption location of 96μm from the top surface of the film. A plot of the fractional recovered photocurrent versus the interruption time was exponential for both holes and electrons as expected. The values of the hole and electron lifetimes were determined to be 58μs and 450μs respectively. The IFTOF technique is a powerful tool for accurately measuring the deep trapping time of both electrons and holes in the bulk of a-Se photoconductor films.

6.2 The Effects of Alloy Composition on the Charge Carrier Range

TOF and IFTOF experiments were applied to the study of the effects of the alloy composition on the charge carrier drift mobility and lifetime in stabilized a-Se photoreceptor films. The product $\mu\tau$ is known as the carrier range, and it determines the charge collection efficiency of the photoconductor film. It is therefore desirable to understand the compositional effects on the $\mu\tau$ product in order to select an appropriate a-Se alloy for a particular x-ray detector design. The advantage of using IFTOF measurements for this investigation is that the charge carrier lifetimes can be accurately determined in the bulk of the film.

The hole mobility was unaffected by changes to the composition of the alloy. The hole lifetime however, showed a strong dependence on the concentrations of As and Cl in the alloy, and this was reflected in the observed hole ranges. As the concentration of As was increased in the alloy, the hole lifetime, and hence the hole range, decreased rapidly. This decrease could be compensated for with the addition of a small amount (i.e. ~20 ppm) of Cl to the alloy composition; the hole lifetime was observed to increase significantly even with small additions of Cl. The increase in the hole lifetime with Cl could likewise be compensated with the addition of As, thereby decreasing the hole range.

The electron mobility decreased with the concentration of As in the alloy, but it was unaffected by the amount of Cl in the alloy. The dependence of the electron lifetime on the alloy composition was opposite to that observed for the hole lifetime. The electron lifetime increased with an increase in the concentration of As and decreased with an increase in the concentration of Cl. These results were reflected in the dependence of the carrier ranges on the composition of the alloy. The electron range increased with the addition of As to the alloy composition, as the dependence of the electron lifetime was larger than that of the electron mobility, and it decreased with the addition of Cl.

An accurate measurement of the dependence of the carrier ranges on the alloy composition is important from a technological standpoint as it allows device designers to tailor the transport properties of an a-Se photoconductive layer for specific applications. For direct conversion x-ray detectors, this would typically be to maximize the carrier ranges in order to maximize the x-ray absorption and collection efficiency of the photoconductive layer. Additionally, novel a-Se layers may be fabricated to meet alternative design criteria. For example, 'p-type' layers with limited electron transport can be fabricated to function as blocking layers to decrease the dark current in a-Se based x-ray detectors.

The dependence of the carrier lifetimes on the composition of the alloy is attributed to under- and over- coordinated charged defects that result from the integration of As and Cl atoms into the a-Se structure. For example, the addition of As may increase the concentration of Se_1^- defects which act as hole traps and would explain the decrease in the hole lifetime. Furthermore, as only small amounts of Cl are required to observe large changes when compared to As, it is clear that the integration of Cl into the a-Se network has a significant impact on the properties of the film. The exact nature of the compensational effects of As and Cl on the properties of a-Se films is a current topic of research; however a detailed discussion of these processes is beyond the scope of the current investigation.

6.3 Bulk Space Charge Effects and Recombination

The effects of a distribution of trapped negative bulk space charge (electrons) on the hole TOF and IFTOF transient photocurrent signals in stabilized a-Se photoconductive layers was examined. The distribution of the trapped electrons alters the internal electric field and causes the hole TOF photocurrent to decay. The trapped charge also acts as recombination centers for holes, which decreases the effective hole lifetime as measured by the IFTOF experiment. A method to calculate the recombination coefficient between holes and the trapped charge using a sequence of TOF-IFTOF-TOF measurements was developed and applied to several samples of stabilized a-Se photoconductor films.

A technique to determine the capture coefficient between trapped negative bulk space charge and drifting holes was developed using a sequence of TOF-IFTOF-TOF experiments in order to investigate the process that leads to detector ghosting in flat panel x-ray detectors. Charge that is trapped in the bulk of the a-Se layer as a result of x-ray exposure will alter the electric field profile and act as recombination centers for subsequently generated carriers. These effects can be observed by performing TOF and IFTOF measurements in the presence of bulk space charge.

Trapped electrons were induced in various samples of stabilized a-Se by performing repetitive electron TOF experiments. The relative amount of electron trapping induced in a sample was varied by varying the number of times that the electron TOF experiment was repeated. Hole transient photoconductivity experiments in a TOF-IFTOF-TOF sequence were then performed on the sample in order to measure the hole recombination lifetime and the resulting concentration of trapped electrons. The relationship between these two values defines the capture process between the drifting holes in the TOF experiment and the trapped electrons through a value known as the capture coefficient. It was shown that capture coefficient was the same for each sample investigated in the study. Furthermore, it was shown that the capture process is described by a Langevin recombination process. This suggests that a free hole drifts diffusively with a short mean-free-path and experiences a Coulombic capture field from a trapped electron. The value of the capture coefficient between free holes and trapped electron in a-Se films can be used to more accurately model the effects of trapped charge on the performance of a-Se based direct conversion x-ray detectors.

6.4 X-ray Induced Trapping and Recombination

The sensitivity of a-Se based flat panel x-ray detectors decreases with exposure to x-ray radiation. This phenomenon is called ghosting, and it may be attributed to the presence of either trapped bulk space charge or x-ray induced structural defects. Trapped charge from previous x-ray exposures alters the internal electric field and acts as recombination centers for subsequent photogenerated carriers, which effectively reduces the carrier lifetime. X-ray induced structural defects, such as a negatively charged coordination defect Se_1^-, increase the concentration of deep traps and, hence, reduce the deep trapping time of the carries. Both effects would result in a decrease in the x-ray sensitivity of the detector since the amount of collected charge for a given x-ray exposure is reduced as the effective carrier lifetime is reduced.

The results of a systematic study of the effects of x-ray exposure on the charge transport properties in stabilized a-Se photoconductive layers were presented. The hole mobility, electron mobility and electron lifetime were unaffected by exposure to x-ray radiation. The effective hole lifetime τ_h, however, decreased significantly with exposure to x-rays; this decrease in τ_h corresponded to a linear increase in the number of hole capture centers as a function of x-ray exposure. Following the x-ray exposure, while the sample was short circuited and allowed to rest in the dark, τ_h slowly recovered to its initial value. The corresponding decrease in the number of hole capture centers followed an exponential dependence with a time constant that was equal to the release rate of electrons from mid-gap states (i.e. deep traps). Therefore, the effect of the x-ray exposure on the hole lifetime was temporary, and it was attributed to the presence of x-ray induced hole capture centers that may be trapped electrons from previous x-ray exposures.

This hypothesis was further examined by using the bulk space charge measurement technique to measure the capture coefficient C_r between drifting holes and the x-ray induced hole capture centers in a sample of stabilized a-Se. It was found that the value of C_r was independent of the x-ray exposure and equal to the Langevin recombination coefficient. This value was then used to calculate the concentration of x-ray induced capture centers *N* for a given x-ray exposure; it was found that *N* increased linearly with x-ray exposure, in agreement with the previous observations. These results provide strong evidence that the x-ray induced capture centers are indeed trapped electrons from previous x-ray exposures, as opposed to x-ray induced structural defects. This distinction is indispensable for device designers working on commercializing a-Se based direct conversion x-ray detectors, since accurate models may now be generated to predict the operating performance of their detector designs.

6.5 Suggestions for Future Work

The interrupted field time-of-flight transient photoconductivity apparatus provides a unique approach for measuring the charge carrier drift mobility and trapping lifetimes in high resistivity semiconductors. The focus of this work was to exploit the advantages of the IFTOF system for various studies involving a-Se based photoconductors suitable for use in direct conversion x-ray detectors. The most important extension of the present work would be to incorporate a cryostat into the existing system in order to measure the properties of a-Se films as a function of temperature. Specifically, TOF measurements performed at low temperatures can be used to resolve controversies surrounding the exact shape of the density of states in a-Se films. IFTOF measurements can be used to probe the temperature dependence of the hole lifetime recovery in x-ray irradiated a-Se photoconductive layers. The rate of the recovery should decrease with temperature because the release rate of electrons from deep traps decreases with temperature.

Furthermore, the existing experimental setup may be easily configured to measure the x-ray sensitivity of a-Se photoconductors as a function of temperature. The electron-hole-pair (EHP) creation energy is field dependent in a-Se. This field dependence can be attributed to recombination between the photogenerated electrons and holes. Currently there are two competing theories to explain this recombination process; the first is geminate recombination governed by the Onsager model, and the second is columnar recombination involving the recombination of non-geminate electrons and holes in the columnar track of a primary electron. Measurements performed over a wide enough range of temperatures could resolve this controversy.

7. REFERENCES

[1] Cowen A.R., “Digital x-ray imaging”, Measurement Science and Technology, **2**, 1991, pp. 691-707.

[2] Kallergi M., “Computer-aided diagnosis of mammographic microcalcification clusters”, Medical Physics, **31**, 2004, pp. 314-326.

[3] Guler N.F. and Ubeyli E.D., “Theory and applications of telemedicine”, Journal of Medical Systems, **26**, 2002, pp. 199-220.

[4] Kasap S.O. and Rowlands J.A., “Direct-conversion flat-panel x-ray image sensors for digital radiography”, Proceedings of the IEEE, **90**, 2002, pp. 591-604.

[5] Zhao W. and Rowlands J.A., “X-ray imaging using amorphous selenium: feasibility of a flat panel self-scanned detector for digital radiology”, Medical Physics, **22**, 1995, pp. 1595-1604.

[6] Kasap S.O. and Rowlands J.A., “Review: X-ray photoconductors and stabilized a-Se for direct conversion digital flat-panel x-ray image detectors”, Journal of Materials Science: Materials in Electronics, **11**, 2000, pp.179-198.

[7] Boone J.M., “Chapter 1: X-ray production, interaction, and detectin in diagnostic imaging”, *Handbook of Medical Imaging: Volume 1. Physics and Psychophysics*, edited by Beutel J., Kundel H.L., and VanMetter R.L., SPIE Press, Bellington, 2000, pp. 1-78.

[8] Yaffe M., “Digital mammography”, www.sunnybrook.utoronto.ca:8080/~yaffe/DigitalDetectors.html, Sunnybrook and Women’s College Health Sciences Centre, Toronto, 2004.

[9] Kasap S.O., “X-ray sensitivity of photoconductors: application to stabilized a-Se”, Journal of Physics D: Applied Physics, **33**, 2000, pp. 2853-2865.

[10] Suzuki K., *Amorphous and Microcrystalline Semiconductor Devices: Optoelectronic Devices*, edited by J. Kanicki, Artech House, Boston, 1991, Ch. 3.

[11] Kasap S.O. and Rowlands J.A, "Direct-conversion flat-panel x-ray image detectors", IEE Proceedings: Circuits, Devices, and Systems, **149**, 2002, pp. 85-96.

[12] Que W. and Rowlands J.A., "X-ray photogeneration in amorphous selenium: geminate versus columnar recombination", Physical Review B, **51**, 1995, pp. 10500-10507.

[13] Mort J., *The anatomy of xerography: Its invention and evolution*, McFarland and Company, Jefferson, 1989.

[14] Kasap S.O., "Photoreceptors: The Chalcogenides", Chapter 9 in *The Handbook of Imaging Materials: Second Edition, Revised and Expanded*, edited by A.S. Diamond and D.S. Weiss, Marcel Dekker Inc., New York, 2002, pp. 329-368.

[15] Street R.A., *Hydrogenated amorphous silicon*, Cambridge University Press, London, 1990.

[16] Madan A. and Shaw M.P., *The Physics and Applications of Amorphous Semiconductors*, Academic Press Inc., San Diego, 1988.

[17] Mott N.F., "Electrons in disordered structures", Advances in Physics, **16**, 1967, pp. 49-57.

[18] Anderson P.W., "Absence of diffusion in certain random lattices", Physical Review, **109**, 1958, pp. 1492-1505.

[19] Brodsky M.H., *Amorphous semiconductors*, Springer-Verlag, New York, 1979.

[20] Cohen M.H., Fritzsche H. and Ovshinski S.R., "Simple band model for amorphous semiconductor alloys", Physical Review Letters, **22**, 1969, pp. 1065-1072.

[21] Marshall J.M. and Owen A.E., "Drift mobility studies in vitreous arsenic triselenide", Philosophical Magazine, **24**, 1971, pp. 1281-1290.

[22] Lucovsky G., *Physics of selenium and tellurium*, edited by E. Gerlach and P. Grosse, Springer-Verlag, New York, 1979.

[23] Lucovsky G. and Galeener F.L., "Intermediate range order in amorphous solids", Journal of Non-Crystalline Solids, **35-36**, 1980, pp. 1209-1214.

[24] Meek P.E., "Structural interpretations of the vibrational spectra of models of amorphous As and Se", *Proceedings of the Symposium on the Structure of Non-*

Crystalline Solids, edited by P.H. Gaskell, Taylor & Francis Ltd., London, 1977, pp. 235-237.

[25] Robertson J., "Electronic structure of amorphous semiconductors", Advances in Physics, **32**, 1983, pp. 361-452.

[26] Adler D. and Yoffa E.J., "Localized electronic states in amorphous semiconductors", Canadian Journal of Chemistry, **55**, 1977, pp. 1920-1929.

[27] Abkowitz M., "Changes in the photoelectric properties of glassy chalcogenides induced by chemical doping, irradiation, and thermal history", Journal of Chemical Physics, **46**, 1967, pp. 4537.

[28] Agarwal S.C., "Nature of localized states in amorphous semiconductors: a study by electron spin resonance", Physical Review B, **7**, 1973, pp. 685-691.

[29] Mott N.F. and Davis E.A., *Electronic Processes in Non-Crystalline Material, 2nd ed.*, Oxford University Press, Oxford, 1979, Chapters 6 and 10.

[30] Elliot S.R., "A unified model for reversible photostructural effects in chalcogenide glasses", Journal of Non-Crystalline Solids, **81**, 1986, pp. 71-98.

[31] Carles D., Lefrancois G. and Larmagnac J.P., "A model for steady-state photoconductivity in amorphous selenium", Journal of Physics Letters, **45**, 1984, pp. L901-L906.

[32] Abkowitz M., "Density of states in a-Se from combined analysis of xerographic potentials and transient transport data", Philosophical Magazine Letters, **58**, 1988, pp. 53-57.

[33] Spear W.E., "Transit time measurements of charge carriers in amorphous selenium films", Proceedings from the Physical Society of London, **B70**, 1957, pp. 669-675.

[34] Rudenko A.I. and Arkhipov V.I., "Drift and diffusion in materials with traps. I. Quasi-equilibrium transport regime", Philosophical Magazine B, **45**, 1982, pp. 177-187.

[35] Kasap S.O. and Juhasz C., "Time-of-flight drift mobility measurements on chlorine-doped amorphous selenium films", Journal of Physics D: Applied Physics, **18**, 1985, pp. 703-720.

[36] Abkowitz M.A. and Pai D.M., "Photoelectronic behavior of a-Se and some a-Se:As alloys in their glass transition regions", Physical Review B, **18**, 1978, pp. 1741-1750.

[37] Juska G., Matulionis A., and Viscakas J., "Measurement of thermal release and transit time in case of multiple trapping", Physica Status Solidi, **33**, 1969, pp. 533-539.

[38] Orlowski T.E. and Abkowitz M., "Microstripline transient photocurrents in a-Se structure resolved in shallow band tail states", Solid State Communications, **59**, 1986, pp. 665-668.

[39] Marshall J.M. and Owen A.E., "The hole drift mobility of vitreous selenium", Physica Status Solidi A, **12**, 1972, pp. 181-191.

[40] Abkowitz M., "Evidence of the defect origin of states which control photoelectric behavior of amorphous chalcogenides", Journal of Non-Crystalline Solids, **66**, 1984, pp. 315-320.

[41] Abkowitz M., "Relaxation induced changes in electrical behavior of glassy chalcogenide semiconductors", Polymer Engineering Science, **24**, 1984, pp. 1149-1154.

[42] Abkowitz M. and Markovics J.M., "Evidence of equilibrium native defect populations in amorphous chalcogenides from analysis of xerographic spectra", Philosophical Magazine B, **49**, 1984, pp. L31-L36.

[43] Pai D.M, "Time-of-flight study of the compensation mechanism in a-Se alloys", Journal of Imaging Science and Technology, **41**, 1997, pp 135-142.

[44] Song H.Z., Adriaenssens G.J., Emelianova E.V., and Arkhipov V.I., "Distribution of gap states in amorphous selenium thin films", **59**, 1999, pp. 10607-10613.

[45] Hartke J.L. and Regensburger P.J., "Electronic states in vitreous selenium", Physical Review, **139**, 1965, pp. A970-A980.

[46] Davis E.A., "Optical absorption, transport and photoconductivity in amorphous selenium", Journal of Non-Crystalline Solids, **4**, 1970, pp. 107-116.

[47] Adachi H. and Kao K.C., "Dispersive optical constants of amorphous selenium $Se_{1-x}Te_x$ films", Journal of Applied Physics, **51**, 1980, pp. 6326-6331.

[48] Pai D.M. and Enck R.C., "Onsager mechanism of photogeneration in amorphous selenium", Physical Review B., **11**, 1975, pp. 5163-5174.

[49] Spear W.E., "Drift mobility techniques for the study of electrical transport properties in insulating solids", Journal of Non-Crystalline Solids, **1**, 1969, pp. 197-214.

[50] Polischuk B., *Interrupted Field Time-of-Flight Transient Photoconductivity Technique and its Applications to Amorphous Semiconductors*, Ph. D. Thesis, University of Saskatchewan, Saskatoon, Canada, 1994.

[51] Papadakis A.C., "Theory of space-charge perturbed currents in insulators", Journal of Physics and Chemistry of Solids, **28**, 1967, pp. 641-647.

[52] Kasap, S.O., *Optoelectronics and Photonics: Principles and Practices*, Prentice Hall, Upper Saddle River, New Jersey, 2001.

[53] Hecht K., "Zum mechanismus des lichtelektrischen primärstromes in isolierenden kristallen", Zeitschrift Fur Physik, **77**, 1932, pp. 235-245.

[54] Zanio K.R., Akutagawa W.M., and Kikuchi R., "Transient currents in semi-insulating CdTe characteristic of deep traps", Journal of Applied Physics, **39**, 1968, pp. 2818-2828.

[55] Akutagawa W. and Zanio K., "The possibility of using CdTe as a gamma spectrometer", 1968, IEEE Transactions on Nuclear Science, **15**, pp. 266-274.

[56] Nesdoly M.T.A., *X-ray sensitivity and x-ray induced charge transport changes in stabilized a-Se films*, Ph. D. Thesis, University of Saskatchewan, Saskatoon, Canada, 2000.

[57] Martini M., Mayer J.W., and Zanio K.R., "Drift velocity and trapping in semiconductors – transient charge technique", *Applied State Science: Advances in Materials and Device Research*, edited by R. Wolfe, Academic Press, 1972.

[58] Blakney R.M. and Grunwald H.P., "Small-signal current transients in insulators with traps", Physical Review, **159**, 1967, pp. 658-664.

[59] Blakney R.M. and Grunwald H.P., "Trapping processes in amorphous selenium", Physical Review, **159**, 1967, pp. 664-671.

[60] Kasap S.O., Thakur R.P.S., and Dodds D., "Method and apparatus for interrupted transit time transient photoconductivity measurements", Journal of Physics E: Scientific Instrumentation, **21**, 1988, pp. 1195-1202.

[61] Schmidlin F.W., "Theory of trap-controlled transient photoconduction", Physical Review B, **16**, 1977, pp. 4466-4473.

[62] Noolandi, J., "Multiple-trapping model of anomalous transit time dispersion in a-Se", Physical Review B, **16**, 1977, pp. 4466-4473.

[63] Schmidlin, F.W., "Theory of multiple trapping", Solid State Communication, **22**, 1977, pp. 451-453.

[64] Rudenko, A.I., "Theory of trap-controlled transient current injection", Journal of Non-Crystalline Solids, **22**, 1976, pp. 215-218.

[65] Polischuk B., Kasap S.O., and Baillie A., "Study of phtogenerated charge carrier dispersion in chlorinated a-Se:0.3%As by the interrupted field time-of-flight technique", Applied Physics Letters, **63**, 1993, pp. 183-185.

[66] Zhang Q. and Champness C.H., "Charge decay in amorphous selenium layers with an intermediate aluminum oxide layer", Canadian Journal of Physics, **69**, 1990, pp. 278-283.

[67] Kepler R.G., "Charge carrier production and mobility in anthracine crystals", Physical Review, **119**, 1960, pp. 1226-1229.

[68] Leblanc O.H., "Hole and electron drift mobilities in anthracine", Journal of Chemical Physics, **35**, 1960, pp. 1275-1280.

[69] Brown F.C., "Temperature dependence of electron mobility in AgCl", Physical Review, **97**, 1955, pp. 355-362.

[70] Kasap S.O. and Juhasz C., "Transient photoconductivity probing of negative bulk space charge evolution in halogenated amorphous selenium films", Solid State Communications, **63**, 1987, pp. 553-556.

[71] Mort J., Troup A., Morgan M., Grammatica S., Knights J.C., and Lujan R., "Geminite recombination in a-Si:H", Applied Physics Letters, **38**, 1981, pp. 277-279.

[72] Naito H., Nakaishi M., Nakayama H., Okuda M., Nakau T., Suzuki A., and Matsushita T., "Isothermal photocurrent transient spectroscopy of gap states in amorphous chalcogenide semiconductors", Japanese Journal of Applied Physics, **22**, 1983, pp. 1818-1821.

[73] Tabak M.D. and Warter P.J., "Field-controlled photogeneration and free carrier transport in amorphous selenium films", Physical Review, **173**, 1968, pp. 899-907.

[74] Oda O., Onozuka A., and Tsuboya T., "Effect of oxygen on electrophotographic properties of selenium", Journal of Non-Crystalline Solids, **83**, 1986, pp. 49-62.

[75] Abkowitz M.A., Rice M.J., and Stolta M., "Electronic transport in silicon backbone polymers", Philosophical Magazine B, **61**, 1990, pp. 25-57.

[76] Reza, T., *Electron and Hole transport in stabilized a-Se for x-ray imaging*, M. Sc. Thesis, University of Saskatchewan, Saskatoon, 1997.

[77] Kasap S.O., Polischuk B. and Dodds D., "An interrupted field time-of-flight (IFTOF) technique in transient photoconductivity measurements", Review of Scientific Instruments, **61**, 1990, pp. 2080-2087.

[78] Helfrich W. and Mark P., "Space charge limited currents in anthracine as a means of determining the hole drift mobility", Zeitschrift Fur Physik, **166**, 1962, pp. 370-385.

[79] Polischuk B. and Kasap S.O., "A high-voltage interrupted-field time-of-flight transient photoconductivity apparatus", Measurement Science & Technology, 1991, **2**, 75-80.

[80] Könenkamo R., Hermann A.M., and Madan A., "Photocurrent reversal and time-of-flight in amorphous silicon-hydrogen films", Philisophical Magazine B, **48**, 1983, L33-L37.

[81] Tabak, M.D. and Scharge M., "Transition from emission limited to space charge limited photoconductivity", 1970, Journal of Applied Physics, **41**, pp. 2114-2118.

[82] Polischuk B., Kasap S.O., Dodds D., and Yannacopoulos S., "Charge trapping studies in amorphous selenium films by the interrupted transit time time-of-flight technique", Proceedings from the Fourth International Symposium on uses of Selenium and Tellurium, 1989, pp. 202-218.

[83] Kasap S.O., Aiyah V., Polischuk B., Bhattacharyya A., and Liang Z., "Deep-trapping kinematics of charge carriers in amorphous semiconductors: A theoretical and experimental study", 1991, Physical Review B, **43**, pp. 6691-6705.

[84] Kasap S.O., "Charge-carrier deep-trapping kinetics in high-resistivity semiconductors", 1992, Journal of Physics D: Applied Physics, **25**, pp. 83-93.

[85] Tabak M.D. and Hillegas W.J., "Preparation and transport properties of vacuum evaporated selenium films", 1972, Journal of Vacuum Science Technology, **9**, pp. 387-392.

[86] Kasap S.O. and Juhasz C., "Charge transport in selenium based amorphous xerographic photoreceptors", 1982, Photographic Science and Engineering, **26**, pp. 239-244.

[87] Juhasz C., Vaezi-Nejad S.M., and S. O. Kasap, "Electron and hole drift mobility in amorphous selenium based photoreceptors", Journal of Imaging Science, **29**, 1985, pp. 144-148.

[88] Kasap S.O., Koughia K.V., Fogal B., Belev G., and Johanson R.E., "The influence of deposition conditions and alloying on the electronic properties of amorphous selenium", Semiconductors, **37**, 2003, pp. 816-21.

[89] Wei Z., DeCrescenzo G., and Rowlands J.A., "Investigation of lag and ghosting in amorphous selenium flat-panel X-ray detectors", Proceedings of the SPIE - The International Society for Optical Engineering, **4682**, 2002, pp. 9-20.

[90] Choquette M., Rougeot H., Martin J., Laperriere L., Shukri Z., and Polischuk B., "Direct selenium x-ray detector for fluoroscopy, R&F, and radiography", Proceedings of the SPIE - The International Society for Optical Engineering, **3977**, 2000, pp. 128-136.

[91] He Z., "Review of the Shockley-Ramo theorem and its application in semiconductor gamma-ray detectors", Nuclear Instruments and Methods in Physics Research A, **463**, 2001, pp. 250-267.

[92] Haugen C. and Kasap S.O., "Langevin recombination of drifting electrons and holes in stabilized a-Se (Cl-doped a-Se:0.3% As)", Philosophical Magazine B, **71**, 1995, pp. 91-96.

[93] Schiebel U., Buchkremer T., Frings G., and Quadflieg P., "Deep trapping and recombination in a-Se:As x-ray sensitive photoreceptors.", Journal of Non-Crystalline Solids, **115**, 1989, pp. 216-218.

[94] Kalade J., Montrimas M., and Rakauskas J., "The mechanism of sensitivity reduction in selenium layers irradiated by x-rays", Physica Status Solidi A, **25**, 1974, pp. 629-636.